Fatigue Load Monitoring of an Onshore Wind Turbine

By

J.A. Bilbao Nieva

in partial fulfilment of the requirements for the degree of

Master of Science

in Civil Engineering

at the Delft University of Technology,

to be defended publicly on July 8, 2021 at 13.00.

Thesis committee:	Prof. Dr. A. Metrikine,	TU Delft
	Prof. Dr. E. Lourens,	TU Delft
	Prof. Dr. A. Cicirello,	TU Delft
	Dr. L. Ziegler,	EnBW

TU Delft

EnBW

Abstract

Wind turbines are typically designed for an operational life of 20-25 years. The operation of the assets can be extended beyond their design life if structural components have sufficient reserves left. One approach is to monitor fatigue loads and compare these with design assumptions to determine the remaining useful lifetime of the assets. A major challenge is that sensors for measuring the stress history, such as strain gauges, only deliver local information. Monitoring of every hot spot is technically and financially not feasible due to cost and access restrictions. In addition, strain gauges only have a limited lifetime when compared to accelerometers.

Several response estimation or extrapolation methods have been proposed in literature to tackle this problem. All of them are Kalman filter based methods, with the exception of the Modal Decomposition and Expansion Method. A new Kalman filter based method has been recently proposed in literature called Gaussian Process Latent Force Model. The aim of this work is to assess this new method with respect to existing ones both theoretically and numerically.

Theoretically, the Kalman filter based methods always rely on white gaussian noise assumptions for the unknown loads, and the modal decomposition and expansion method disregard measurement imperfections. The new method improves upon these assumptions by providing a flexible stochastic definition for the unknown load, and by taking into account measurement imperfections.

The numerical analysis is restricted to a comparison with respect to the modal decomposition and expansion method given the different theoretical backgrounds. The comparison is realised upon a simulation which illustrates and validates the methods, and upon a real-life onshore wind turbine equipped with accelerometers and strain gauges. Measured strains are compared with estimated strains. The accuracy of each method is quantified using the mean absolute error and by the correlation between measurement and estimation. The higher accuracy obtained shows that the new method is an improvement upon existing methods. This is further extended in the calculation of Damage Equivalent Loads. The result shows a relative error that, depending on operational conditions, ranges within 20-40[%] for the modal decomposition and expansion method and less than 10[%] for the new method.

These results show that the novel Gaussian Process Latent Force Model method should be taken into account for response estimation when accuracy is relevant. Future works should aim on developing a mechanical model that better capture the real behaviour of the wind turbine, as the accuracy of the response estimation methods is mainly controlled by the validity of the underlying assumptions of the mechanical model. Furthermore, the strain estimations should be sought in the whole frequency range, this can be realised by including measurements that deliver this information: GPS sensors or inclinometers for example.

Acknowledgments

This work would have been impossible without guidance throughout the entirety of the project, and therefore I would like to extend my gratitude to those who have been of assistance and support.

First, I would like to thank EnBW for providing the opportunity to work in such an interesting topic. Specifically, my industry supervisors Lisa Ziegler and Andreas Schultze for providing the technical support on the project, and the week-to-week guidance enabling me to achieve the highest quality of work possible.

I would also like to express my gratitude to my academic supervisors. Eliz-Mari Lourens for taking an active part in the weekly meetings and for the highly valuable expertise on the subject. Andrei Metrikine for accepting to be the Chairman of the committee and for the insightful comments on the progress meetings, and Alice Cicirello for accepting to be part of the assessment committee.

Thanks also to all the colleagues and fellow students that helped me throughout this process.

Special thanks to my friends and family. Your unconditional support during these trying times has been invaluable.

Contents

Nomenclature

General Notation

Matrices, bold and capitalized:	$\boldsymbol{X}$
Vectors, bold and lower case:	$\boldsymbol{x}$
Scalars, lower case:	x
Time dependencies may be omitted for simplicity:	$x(t) \rightarrow x$
Time derivatives are expressed using Newton's notation:	$\frac{\mathrm{d}x(t)}{\mathrm{d}t} = \dot{x}$
Discrete-time notation:	$\boldsymbol{x}(t = k\Delta t) = \boldsymbol{x}_{[k]}$
Estimations are, in general, denoted with a hat:	$\hat{x}$

Abbreviations

GPLFM	Gaussian Process Latent Force Model
MD&E	Modal Decomposition and Expansion
MAE	Mean Absolute Error
TRAC	Time Response Assurance Criterion
MAC	Modal Assurance Criterion
MDOF	Multi-Degree Of Freedom
SSI-Cov	Covariance Driven Stochastic Subspace Identification
pLSCF	poly-reference Least-Squares Complex Frequency-domain estimator
OPTICS	Ordering Points To Identify the Clustering Structure
RD	Reachability Distance
CD	Core Distance
MinObj	Minimum number of Objects

1 Introduction

1.1 Motivation

The energy sector has undergone a shift towards renewable energies in order to meet the Paris Agreement target of holding the increase in the global average temperature well below 2°C [1]. Wind Energy plays an important role in accomplishing this objective. More than one-third (35%) of the total electricity needs would be generated by both onshore and offshore wind turbines by 2050 [2].

Wind turbines are subject to a highly variable load: the wind. The loading cycles that this load produces on the structure brings considerable fatigue loads as a consequence. Typically, wind turbines are designed for a 20-year life with the fatigue loads governing the design [3]. The lifetime can be extended if the structural components have sufficient reserves left. This can be done by assessing the state of the system [4]. This assessment has to include the entire wind turbine, and in particular, all the load transferring components. One of these components is the tower, which is the element under analysis in this work.

As indicated in [4], the assessment of the tower has to include the comparison of the original design conditions with the conditions on site. One approach is to measure the stresses that the tower has withstood over its lifetime. The stresses on a specific point of the tower can be measured by employing strain sensors. It is unpractical however to install strain sensors on all points of the structure, which means that the response has to be estimated from a discrete set of measurements. Furthermore, it has been observed that the use of strain sensors are less reliable and harder to maintain than accelerometers over long periods of time [5].

This motivation brings the main research question of this thesis:

“Is it possible to obtain the strain response from a discrete set of acceleration measurements?”

The problem of estimating the response at unmeasured locations from a set of discrete measurements will be referred to hereafter as “Response Estimation”.

1.2 Literature Review

1.2.1 Wind Turbines: preliminary understanding

Some basic definitions and concepts regarding wind turbines are briefly presented in this section. The main components of the wind turbine are shown in Figure 1-1.

Wind turbines have several moving parts. The most relevant to consider for this work, besides the rotor motion, are the motion of the nacelle, characterised by the yaw angle, and the motion of the blades, characterised by the pitch. The yaw angle refers to the rotation of the nacelle in order to orientate the rotor in the wind direction. The pitch refers to the rotation of the blades in order to control the angle of attack of the wind to the blades.

The dynamic characterisation of the structure can be defined through the natural modes of vibrations. These may be divided in two sets: modes related to the tower, and modes related to the rotor. The rotor modes refer to those that are mainly related to the blades, while the tower modes refer to those that are mainly related to the tower vibrations. Coupled modes also exist. A description of these modes may be found in [3]. Furthermore, in [6] an experimental identification of these modes is presented.

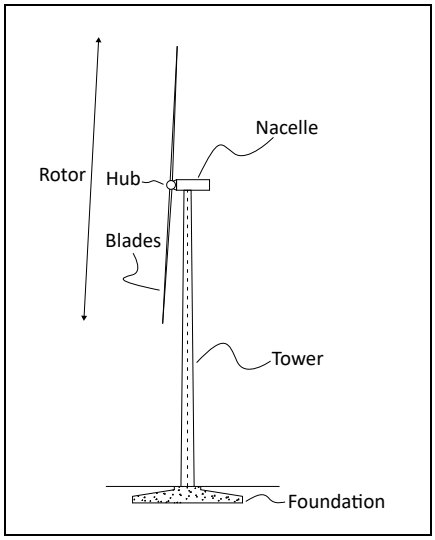

Figure 1-1. Wind Turbine main components.

Given the focus of this work on the tower response, only the tower modes will be sought to be represented by the mechanical model. It is noted however that the response of the tower will be also influenced by the rotor mode shapes, although to a lesser extent. The tower modes are often divided in three directions: the fore-aft (FA) direction, the side-side (SS) direction and the torsional direction. The FA and SS direction modes are sketched in Figure 1-2. The torsional direction refers to the torsional motion of the tower.

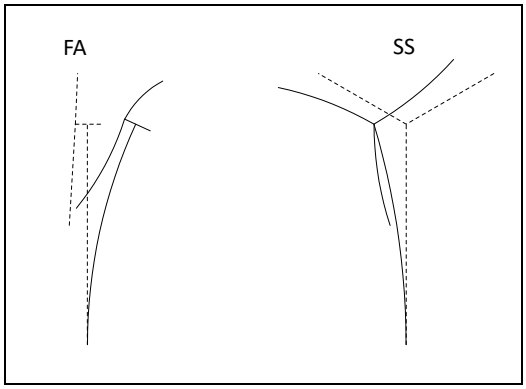

Figure 1-2. Tower mode shapes. FA and SS directions.

The modal parameters of the structure vary in time as a consequence of different operational conditions. Two conditions are highlighted: The rotor speed and the wind speed. As discussed in [7], the rotor speed affects mainly the rotor modes. The tower modes are not affected in a considerable manner. The wind speed brings as a consequence an effect known as aerodynamic damping [3]. In simple terms, the motion of the tower implies a change in both the relative velocity of the wind with respect to the blades, and also a change in the angle of attack of the blades. This results in a load which is a function of the response of the blades motion in terms of velocity. Consequently, a higher wind speed will yield a higher aerodynamic effect.

Finally, the analysis of the system due to the wind load has to take into account the tower shadow effect [3]. The wind pressure is decreased locally in the presence of the tower, both down-wind and up-wind. This means that the wind pressure acting on the blades while passing through the tower is decreased. This brings as a consequence a harmonic load transferred to the tower every time a blade passes in front of it. In consequence, a harmonic load is expected to occur in the tower at multiples of $3f_{rotor}$, with f_{rotor} the rotor frequency (speed). Note that a harmonic load occurs also at the rotor frequency due to its rotation.

1.2.2 Overview on response estimation

Several methods that address the problem of response estimation have been proposed in literature. The most relevant methods are briefly introduced as follows:

Kalman Filter: First introduced in [8] provides an algorithm to solve problems that can be formulated by a discrete state space model in a recursive and optimal manner. In the context of this work, it can be applied considering a known load, or by assuming the load being part of the noise on the process and measurements [5].

Augmented Kalman Filter: Presented in the context of structural dynamics in [9]. It augments the state equation by including the load as part of the augmented state. The solution afterwards is obtained by means of applying the Kalman Filter to this augmented formulation. It has stability issues if measuring acceleration only [10].

Augmented Kalman Filter With dummy measurements Considers the inclusion of dummy measurements seeking to minimize the error produced from the stability issues. Proposed in [11].

Dual Kalman filter [12]. It seeks to solve the problem of estimation of the load by using two parallel Kalman Filters, one to estimate the load, and another to estimate the state considering the estimated load. As shown in [13], it is outperformed by the Joint input-response estimation.

Joint input-response estimation: Based on [14], and presented in the context of structural dynamics in [15]. It includes the load estimation as part of a Kalman Filter approach. The stability issues when measuring accelerations only still prevail [10].

Extension on Joint input-response estimation: An extension of this approach is presented in [16] by considering that the noise between processes is non-zero, and furthermore providing a methodology to estimate the noise covariances. The stability issues when measuring accelerations only still prevail [10].

Modal Decomposition and Expansion (MD&E): Presented in [17]. It is based only on the mode shapes of a well calibrated finite element model. It is therefore a very simple yet effective approach for response estimation.

Gaussian Process Latent Force Model (GPLFM): Recently introduced in [18] and extended in [19] for its implementation on joint input-state-parameter estimation. It assumes a stochastic description for the load that is not limited by a white gaussian assumption, in contrast to all other Kalman Filter based methods. It does not have stability issues when using only accelerations. It uses the Kalman filter in order to compute posterior distributions: this means that it yields not only the expected values (estimations) but also the variances (uncertainty). It has been shown in [18] that this method can be reduced to the Augmented Kalman Filter but without stability (drift) issues.

1.2.3 Response estimation in the context of wind turbines

Some case studies in the context of wind turbines are discussed in the following.

A first approach towards the problem of fatigue estimation of wind turbines can be found in [20], where the need to separate between a low frequency content (quasi-static loads) and high frequency content (dynamic loads) is highlighted. This is a consequence of the nature of the loads that the structure is subject to. The response estimation problem is concerned with the higher frequency content. Though it provides a good framework for the problem of fatigue estimation, the mechanical model considered is an oversimplification of the real problem. Therefore, no relevant response estimation method is found.

In [21], [17] and [22] the use of MD&E towards fatigue estimation can be found:[21] introduces MD&E for estimating accelerations at one point on the structure from measured accelerations at another

point, [17] employs both accelerations and strain measurements to estimate strains, and finally in [22] the last approach is combined with a low frequency (quasi-static load) estimation to estimate fatigue.

In [5] a comparison is made between using Kalman Filter, Joint Input Response and MD&E to estimate strains. Two sets of measurements are evaluated: using only acceleration measurements, and using accelerations and strains measurements. The former, which is of interest for this work, is observed to be accurate in some defined frequency range when using Joint Input Response and MD&E approaches. It is highlighted however that offline displacement estimation is required for the stability of Joint Input Response estimation, and high-pass filtering is required for both joint input response and MD&E in order to avoid errors in the form of low frequency components. Other works such as [23] or [24] uses MD&E and Kalman Filtering approaches for the problem of estimating strains from acceleration measurements, with the MD&E approach being more accurate in comparison to Kalman Filtering.

1.3 Scope

Summarising the literature review, several methods exist that attempt to tackle the problem of Response Estimation. These methods can be divided in two approaches: Kalman Filter based approaches, and the Modal Decomposition and Expansion (MD&E) method.

The novel GPLFM method has been recently proposed in the field of Structural Dynamics [18]. This method belongs to the set of Kalman Filter approaches, and it has not yet been employed in the context of wind turbines.

In light of this novel approach, the scope of this thesis is reduced to answering the following question:

"Does the novel GPLFM method improves upon existing methods?"

This question is restricted to the context of wind turbines and focused towards the tower component.

In order to apply any response estimation method, a mechanical model that is representative of the structure is required.

1.4 Methodology

The term 'improves' stated in the research question implies the need to assess the GPLFM against existing methods. The assessment is executed under two points of view: theoretical and numerical.

The theoretical assessment is performed by exposing the underlying theory of the GPLFM method, and by taking into account the literature review presented in section 1.2.

The numerical assessment is restricted to compare the GPLFM with the MD&E method given that it is the only response estimation method found that falls outside the Kalman Filter based methods, and also given that it has been successfully implemented on wind turbines. This assessment is performed upon a simulated response and upon real data obtained from an operating onshore wind turbine. Note that the simulated response will also be useful for illustrative purposes and for validation of both methods employed.

The onshore wind turbine has been equipped with accelerometers and strain gauges, measuring between December 2020 and January 2021. The accelerometers will be used for the application of the response estimation methods, and the strain gauges will serve as a reference for the numerical results. The simulated response will replicate this configuration. The records used for the analysis will be chosen from the available data set so as to cover the most relevant operating conditions of the wind turbine. The mechanical model considered for the analysis of the onshore wind turbine is validated using system identification.

This methodology brings as a consequence the structure of this thesis, outlined as follows:

Section II: Theoretical Background. This section presents the underlying theory for the mechanical model, system identification and response estimation methods employed. The error metrics considered for the analysis of the numerical results are also introduced.

Section III: Simulation. The system identification and response estimation methods are validated and illustrated through a finite element model simulation.

Section IV: Case Study: Onshore Wind turbine. Both response estimation methods are applied to measured data from an onshore wind turbine.

Section V: Conclusion. The main results and recommendations for future works are presented.

2 Theoretical Framework

2.1 Mechanical model

This section briefly presents the required theoretical background considered for system identification and response estimation.

2.1.1 Equation of Motion and Modal Analysis

The formulation of the Equations of Motion and associated Modal Transformation are well covered in literature (e.g. [25], [26]). The following only presents the relations used by the system identification and response estimation methods.

2.1.1.1 Equation of Motion

The equation of motion for a Multi-Degree of Freedom (MDOF) system is given by:

$$\boldsymbol{M}\ddot{\boldsymbol{u}}(t) + \boldsymbol{C}\dot{\boldsymbol{u}}(t) + \boldsymbol{K}\boldsymbol{u}(t) = \boldsymbol{S_p}\boldsymbol{p}(t) \qquad \text{(Eq. 2-1)}$$

where the mass, damping and stiffness matrices are represented by, $\boldsymbol{M}, \boldsymbol{C}, \boldsymbol{K} \in \mathbb{R}^{n_u \times n_u}$ respectively, and the load locations are defined by $\boldsymbol{S_p} \in \mathbb{R}^{n_u \times n_p}$. The response of the system is defined by $\boldsymbol{u}(t) \in \mathbb{R}^{n_u}$, and the loads in time are defined as $\boldsymbol{p}(t) \in \mathbb{R}^{n_p}$. n_u refers to the total number of degrees of freedom, and n_p refers to the total number of loads.

2.1.1.2 Modal Transformation

Classic modal analysis starts from the assumption that the damping matrix is proportional to the mass or stiffness matrix. Under this assumption, and considering the following modal transformation:

$$\boldsymbol{u}(t) = \boldsymbol{\Phi}\boldsymbol{u_m}(t) \qquad \text{(Eq. 2-2)}$$

The classical modal representation of the equation of motion is obtained:

$$\boldsymbol{I}\ddot{\boldsymbol{u}}_{\boldsymbol{m}}(t) + \boldsymbol{\Gamma}\dot{\boldsymbol{u}}_{\boldsymbol{m}}(t) + \boldsymbol{\Omega}^2\boldsymbol{u_m}(t) = \boldsymbol{\Phi}^{\mathrm{T}}\boldsymbol{S_p}\boldsymbol{p}(t) \qquad \text{(Eq. 2-3)}$$

With $\boldsymbol{u_m} \in \mathbb{R}^{n_u}$ the modal coordinates, $\boldsymbol{\Phi} \in \mathbb{R}^{n_u \times n_u}$ the mass-normalised modal shape matrix (i.e., $\boldsymbol{\Phi}^T\boldsymbol{M}\boldsymbol{\Phi} = \boldsymbol{I}$), $\boldsymbol{\Gamma} \in \mathbb{R}^{n_u \times n_u}$ and $\boldsymbol{\Omega} \in \mathbb{R}^{n_u \times n_u}$ diagonal matrices formed by the natural frequencies ω_n and damping ratios ζ_n so that $\boldsymbol{\Omega} = \mathrm{diag}(\omega_n)$ and $\boldsymbol{\Gamma} = \mathrm{diag}(2\zeta_n\omega_n)$.

Often the response of a structure can be sufficiently represented by a subset of modes $n_m \leq n_u$. This is called a Modal Reduction. The response is then approximated by:

$$\boldsymbol{u}(t) \approx \boldsymbol{\Phi_r}\boldsymbol{u_{mr}}(t) \qquad \text{(Eq. 2-4)}$$

With the reduced mode shapes $\boldsymbol{\Phi}_r \in \mathbb{R}^{n_u \times n_m}$ and modal coordinates $\boldsymbol{u_{mr}} \in \mathbb{R}^{n_m}$. Furthermore, the reduced system matrices are written as $\boldsymbol{\Omega}_r \in \mathbb{R}^{n_m \times n_m}$ and $\boldsymbol{\Gamma}_r \in \mathbb{R}^{n_m \times n_m}$.

2.1.2 Mechanical State Space Model

This section presents the state space model derived from the modal reduction of the MDOF systems previously defined.

The state space model is formed by the state equation, which is an equivalent formulation of the equation of motion, and the observation equation, which relates some set of observations with the state of the system.

2.1.2.1 State Equation

The state equation for the reduced modal formulation is defined as (for the derivation, see e.g. [15]):

$$\dot{\boldsymbol{x}}_{\boldsymbol{m}}(t) = \boldsymbol{A}_{\boldsymbol{cm}}\boldsymbol{x}_{\boldsymbol{m}}(t) + \boldsymbol{B}_{\boldsymbol{cm}}\boldsymbol{p}(t) \quad \text{(Eq. 2-5)}$$

$$\boldsymbol{x}_{\boldsymbol{m}} = \begin{Bmatrix} \boldsymbol{u}_{\boldsymbol{mr}} \\ \dot{\boldsymbol{u}}_{\boldsymbol{mr}} \end{Bmatrix} \quad \text{(Eq. 2-6)}$$

$$\boldsymbol{A}_{\boldsymbol{cm}} = \begin{bmatrix} \boldsymbol{0} & \boldsymbol{I} \\ -\boldsymbol{\Omega}_r^2 & -\boldsymbol{\Gamma}_r \end{bmatrix} \quad \text{(Eq. 2-7)}$$

$$\boldsymbol{B}_{\boldsymbol{cm}} = \begin{bmatrix} \boldsymbol{0} \\ \boldsymbol{\Phi}_r^T \boldsymbol{S}_{\boldsymbol{p}} \end{bmatrix} \quad \text{(Eq. 2-8)}$$

With $\boldsymbol{x}_{\boldsymbol{m}} \in \mathbb{R}^{2n_m}, \boldsymbol{A}_{\boldsymbol{cm}} \in \mathbb{R}^{2n_m \times 2n_m}, \boldsymbol{B}_{\boldsymbol{cm}} \in \mathbb{R}^{2n_m \times n_p}$.

Note that the response can be transformed to the original coordinates by multiplying with the mode shapes:

$$\boldsymbol{x}(t) \approx \begin{bmatrix} \boldsymbol{\Phi}_r & \boldsymbol{0} \\ \boldsymbol{0} & \boldsymbol{\Phi}_r \end{bmatrix} \boldsymbol{x}_{\boldsymbol{m}}(t) \quad \text{(Eq. 2-9)}$$

The approximation being a consequence of using a reduced number of modes.

2.1.2.2 Observation Equation

Let $\boldsymbol{y}(t) \in \mathbb{R}^{n_y}$ be a subset of the system response:

$$\boldsymbol{y}(t) = \boldsymbol{S}_{\boldsymbol{a}}\ddot{\boldsymbol{u}}(t) + \boldsymbol{S}_{\boldsymbol{v}}\dot{\boldsymbol{u}}(t) + \boldsymbol{S}_{\boldsymbol{d}}\boldsymbol{u}(t) \quad \text{(Eq. 2-10)}$$

The matrices $\boldsymbol{S}_{\boldsymbol{a}}, \boldsymbol{S}_{\boldsymbol{v}}, \boldsymbol{S}_{\boldsymbol{d}} \in \mathbb{R}^{n_y \times n_u}$ are the selection matrices for accelerations, velocities, and displacements respectively. These relate the observed (measured) response $\boldsymbol{y}(t)$ of the structure with the mechanical model. Note that n_y represent the total number of displacements, velocities or accelerations being measured.

Considering the modal formulation, and the equation of motion, the observations $\boldsymbol{y}(t)$ can be defined in terms of the state and load applied in the system (for the derivation, see e.g. [15]):

$$\boldsymbol{y}(t) = \boldsymbol{G}_{\boldsymbol{cm}}\boldsymbol{x}_{\boldsymbol{m}}(t) + \boldsymbol{J}_{\boldsymbol{cm}}\boldsymbol{p}(t) \quad \text{(Eq. 2-11)}$$

$$\boldsymbol{G}_{\boldsymbol{cm}} = [[-\boldsymbol{S}_{\boldsymbol{a}}\boldsymbol{\Phi}_r\boldsymbol{\Omega}_r^2 + \boldsymbol{S}_{\boldsymbol{d}}\boldsymbol{\Phi}_r] \quad [-\boldsymbol{S}_{\boldsymbol{a}}\boldsymbol{\Phi}_r\boldsymbol{\Gamma}_r + \boldsymbol{S}_{\boldsymbol{v}}\boldsymbol{\Phi}_r]] \quad \text{(Eq. 2-12)}$$

$$\boldsymbol{J}_{\boldsymbol{cm}} = \boldsymbol{S}_{\boldsymbol{a}}\boldsymbol{\Phi}_r{\boldsymbol{\Phi}_r}^{\mathrm{T}}\boldsymbol{S}_{\boldsymbol{p}} \quad \text{(Eq. 2-13)}$$

With dimensions: $\boldsymbol{G}_{\boldsymbol{cm}} \in \mathbb{R}^{n_y \times 2n_m}, \boldsymbol{J}_{\boldsymbol{cm}} \in \mathbb{R}^{n_y \times n_p}$.

2.1.3 Finite Element Model

The mechanical model is defined numerically through a finite element model. Only beam elements are considered in this work, based upon Euler-Bernoulli beam theory. The element cross section used is assumed to be circular and constant. The particular definition of the finite element is known, and can be found for example in [27]. The relevant expressions are summarised in the following, based upon the information shown in Figure 2-1.

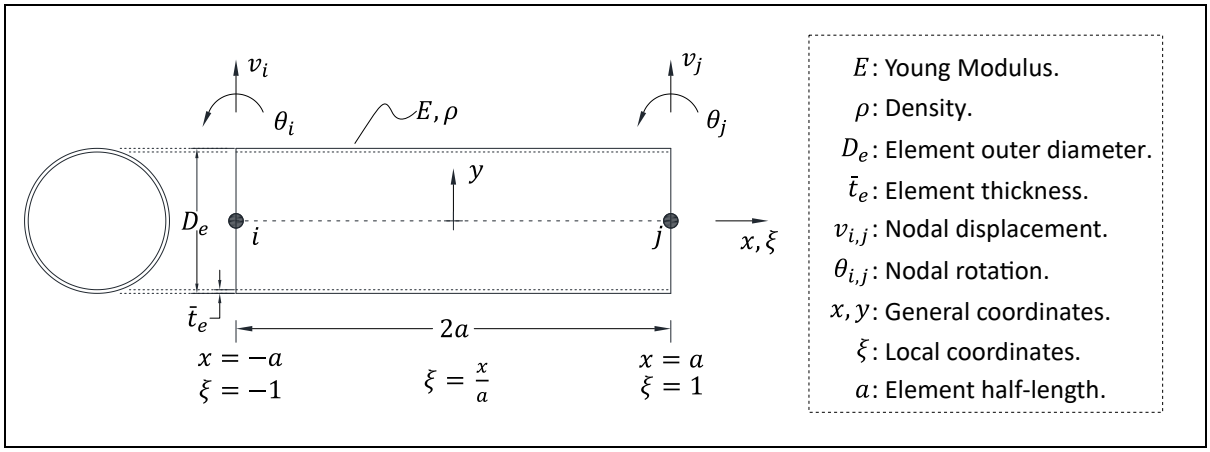

Figure 2-1. Beam Finite Element.

In accordance with Figure 2-1, the nodal displacement vector is defined by:

$$\boldsymbol{u_e} = [v_i \quad \theta_i \quad v_j \quad \theta_j]^T \tag{Eq. 2-14}$$

The shape functions $\boldsymbol{N}$, and spatial derivatives $\boldsymbol{N'}, \boldsymbol{N''}$, are defined in terms of the local coordinate ξ:

$$\boldsymbol{N}(\xi) = [1 \quad \xi \quad \xi^2 \quad \xi^3]\,\boldsymbol{\Xi}(a) \tag{Eq. 2-15}$$

$$\boldsymbol{N'}(\xi) = [0 \quad 1 \quad 2\xi \quad 3\xi^2]\boldsymbol{\Xi}(a) \tag{Eq. 2-16}$$

$$\boldsymbol{N''}(\xi) = [0 \quad 0 \quad 2 \quad 6\xi]\boldsymbol{\Xi}(a) \tag{Eq. 2-17}$$

$$\boldsymbol{\Xi}(a) = \frac{1}{4}\begin{bmatrix} 2 & a & 2 & -a \\ -3 & -a & 3 & -a \\ 0 & -a & 0 & a \\ 1 & a & -1 & a \end{bmatrix} \tag{Eq. 2-18}$$

The displacement or rotation at any point within the element is given by:

$$v(\xi) = \boldsymbol{N}(\xi)\boldsymbol{u_e} \tag{Eq. 2-19}$$

$$\theta(\xi) = \frac{1}{a}\boldsymbol{N'}(\xi)\boldsymbol{u_e} \tag{Eq. 2-20}$$

The element stiffness and mass matrix are then defined as:

$$\boldsymbol{K}_e = \frac{EI_e}{2a^3}\begin{bmatrix} 3 & 3a & -3 & 3a \\ 3a & 4a^2 & -3a & 2a^2 \\ -3 & -3a & 3 & -3a \\ 3a & 2a^2 & -3a & 4a^2 \end{bmatrix} \tag{Eq. 2-21}$$

$$I_e = \frac{\pi}{64}(D_e^4 - (D_e - 2\bar{t}_e)^4) \tag{Eq. 2-22}$$

$$\boldsymbol{M}_e = \frac{\rho A_e a}{105}\begin{bmatrix} 78 & 22a & 27 & -13a \\ 22a & 8a^2 & 13a & -6a^2 \\ 27 & 13a & 78 & -22a \\ -13a & -6a^2 & -22a & 8a^2 \end{bmatrix} \tag{Eq. 2-23}$$

$$A_e = \frac{\pi}{4}(D_e^2 - (D_e - 2\bar{t}_e)^4) \tag{Eq. 2-24}$$

The strain for any point within the element is:

$$\varepsilon_{xx} = -\frac{y_\varepsilon}{a^2}\boldsymbol{N''}(\xi)\boldsymbol{u_e} \tag{Eq. 2-25}$$

With y_ε the distance from the neutral axis.

2.1.3.1 Selection matrices

Selection matrices can be defined with the above relations. First note that the element vector can be related to the global vector through an element selection matrix $\boldsymbol{S_e} \in \mathbb{R}^{4\times n}$:

$$\boldsymbol{u_e} = \boldsymbol{S_e}\boldsymbol{u} \qquad \text{(Eq. 2-26)}$$

Defining the location at which the response is to be evaluated will define the selection matrix $\boldsymbol{S_e}$, which indicates what element it corresponds to. The position within the element is controlled by ξ.

Therefore, in the case of accelerations, the response at a given location (i.e., $\boldsymbol{S_e}$ and ξ known) can be expressed as:

$$\ddot{u} = \ddot{v}(\xi) = \boldsymbol{N}(\xi)\ddot{\boldsymbol{u}}_{\boldsymbol{e}} = \boldsymbol{N}(\xi)\boldsymbol{S_e}\ddot{\boldsymbol{u}} = \boldsymbol{S_{ai}}\ddot{\boldsymbol{u}} \qquad \text{(Eq. 2-27)}$$

This defines the selection matrix for the acceleration $\boldsymbol{S_{ai}} \in \mathbb{R}^{1\times n}$.

The same can be done for the strains, assuming also a defined distance y_ε with respect to the neutral axis:

$$\varepsilon_{xx} = -\frac{y_\varepsilon}{a^2}\boldsymbol{N}''(\xi)\boldsymbol{u_e} = -\frac{y_\varepsilon}{a^2}\boldsymbol{N}''(\xi)\boldsymbol{S_e}\boldsymbol{u} = \boldsymbol{S_\varepsilon}\boldsymbol{u} \qquad \text{(Eq. 2-28)}$$

This defines the selection matrix for the strain $\boldsymbol{S_\varepsilon} \in \mathbb{R}^{1\times n}$.

It is noted that the selection matrices defined here are for a single point in space. In the case that a set of points in space is required (as described in 2.1.2.2), each row can be defined following the above expressions. In particular, each row of $\boldsymbol{S_a}$ is defined by $\boldsymbol{S_{ai}}$ as described in this section**.**

Finally, note that for both cases the selection matrix can be developed for the modal response:

$$\boldsymbol{S_{am}} = \boldsymbol{S_a}\boldsymbol{\Phi} \qquad \text{(Eq. 2-29)}$$

$$\boldsymbol{S_{\varepsilon m}} = \boldsymbol{S_\varepsilon}\boldsymbol{\Phi} \qquad \text{(Eq. 2-30)}$$

2.2 System Identification

2.2.1 Introduction

System Identification involves the problem of estimating the dynamic properties of a structural system. This, in practice, reduces to the problem of estimating frequencies, damping ratios and mode shapes of an existing structure.

In the context of wind turbines, system identification has been successfully applied in literature (see [28], [29]), where two methods in particular have been considered: covariance-driven stochastic subspace identification (SSI-Cov, [30]) and poly-reference least-squares complex frequency-domain estimator (pLSCF, [31]). Both methods have been observed to yield similar results. Only SSI-Cov is employed in this work.

One of the most relevant drawbacks of using SSI-COV, which is also observed for pLSCF, is the need to define the model order of the system. In simple terms, the model order can be understood as the dimension of the system matrices (i.e., number of degrees of freedom) that are needed to represent the structure. A more detailed explanation can be found in section 2.2.2.1. The model order is not easily defined, and even the best estimation for the model order may yield spurious modes. In order to overcome this, the use of stabilisation diagrams is often employed in practice to distinguish physical and spurious modes [30]. A stabilisation diagram is a plot of the frequencies found for a wide range of model orders. Through the stabilisation diagram, the physical modes are detected as they are assumed to appear somewhat consistently across the diagram, in the form of ‘stable columns’.

Stabilisation diagrams must be interpreted to recover the physical modes. Several attempts have been proposed in literature in order to automatically interpret such diagrams (see e.g. [28], [32]). These methods rely on cluster analysis tools to distinguish the physical modes. It is observed also that the success of the methods found in literature are dependent on the measurement setup and the structure conditions.

In this work, a cluster tool useful for both manual analysis and automatic analysis is employed, called OPTICS (Ordering Points To Identify the Clustering Structure, [33]). The use of this tool in the context of stabilisation diagrams for both manual and automatic analysis has been validated in [34]. In this work, only manual analysis of stabilisation diagrams is employed.

This section aims to present the system identification method SSI-COV and the cluster analysis tool OPTICS.

2.2.2 SSI-Cov

The covariance-driven stochastic subspace identification method (SSI-Cov) can be found in [35], [30], [28], [36]. The following introduces the main assumptions and methodology followed for its implementation.

The method starts from the state-space model similar to the one described in Section 2.1.2, but without considering modal reduction (i.e., the state equation as the equation of motion). The state equation is then defined by:

$$\dot{\boldsymbol{x}}(t) = \boldsymbol{A_c}\boldsymbol{x}(t) + \boldsymbol{B_c}\boldsymbol{p}(t) \quad \text{(Eq. 2-31)}$$

$$\boldsymbol{x} = \begin{Bmatrix} \boldsymbol{u} \\ \dot{\boldsymbol{u}} \end{Bmatrix} \quad \text{(Eq. 2-32)}$$

$$\boldsymbol{A_c} = \begin{bmatrix} \boldsymbol{0} & \boldsymbol{I} \\ -\boldsymbol{M}^{-1}\boldsymbol{K} & -\boldsymbol{M}^{-1}\boldsymbol{C} \end{bmatrix} \quad \text{(Eq. 2-33)}$$

$$\boldsymbol{B_c} = \begin{bmatrix} \boldsymbol{0} \\ \boldsymbol{S_p} \end{bmatrix} \quad \text{(Eq. 2-34)}$$

And the observation equation:

$$\boldsymbol{y}(t) = \boldsymbol{G_c}\boldsymbol{x}(t) + \boldsymbol{J_c}\boldsymbol{p}(t) \quad \text{(Eq. 2-35)}$$

$$\boldsymbol{G_c} = [[-\boldsymbol{S_a}\boldsymbol{M}^{-1}\boldsymbol{K} + \boldsymbol{S_d}] \quad [-\boldsymbol{S_a}\boldsymbol{M}^{-1}\boldsymbol{C} + \boldsymbol{S_v}]] \quad \text{(Eq. 2-36)}$$

$$\boldsymbol{J_c} = \boldsymbol{S_a}\boldsymbol{M}^{-1}\boldsymbol{S_p} \quad \text{(Eq. 2-37)}$$

The load is neglected, and implicitly modelled by including noise in both the state and observation equation, therefore the state and observation equations are reduced to (in discrete notation, further details in [30]):

$$\boldsymbol{x}_{[k+1]} = \boldsymbol{A}\boldsymbol{x}_{[k]} + \boldsymbol{w}_{[k]} \quad \text{(Eq. 2-38)}$$

$$\boldsymbol{y}_{[k]} = \boldsymbol{G_c}\boldsymbol{x}_{[k]} + \boldsymbol{v}_{[k]} \quad \text{(Eq. 2-39)}$$

With $\boldsymbol{x}_{[k]} \in \mathbb{R}^{n_x}$ the state vector, $\boldsymbol{y}_{[k]} \in \mathbb{R}^{n_y}$ the observation vector, $\boldsymbol{A} = \exp(\boldsymbol{A_c}\Delta t) \in \mathbb{R}^{n_x \times n_x}$ the state matrix, $\boldsymbol{G_c} \in \mathbb{R}^{n_y \times n_x}$ the output matrix, $\boldsymbol{w}_{[k]} \in \mathbb{R}^{n_x}$ the process noise and $\boldsymbol{v}_{[k]} \in \mathbb{R}^{n_y}$ the observation noise.

It is assumed that the noises are white gaussian processes:

$$\mathbb{E}\left[\boldsymbol{w}_{[k]}\right] = \boldsymbol{0} \quad \text{(Eq. 2-40)}$$

$$\mathbb{E}\left[\boldsymbol{v}_{[k]}\right] = \boldsymbol{0} \quad \text{(Eq. 2-41)}$$

$$\mathbb{E}\left[\begin{pmatrix} \boldsymbol{w}_{[p]} \\ \boldsymbol{v}_{[p]} \end{pmatrix} \begin{pmatrix} \boldsymbol{w}_{[q]}^T & \boldsymbol{v}_{[q]}^T \end{pmatrix}\right] = \begin{pmatrix} \boldsymbol{Q} & \boldsymbol{S} \\ \boldsymbol{S}^T & \boldsymbol{R} \end{pmatrix} \delta_{[p][q]} \quad \text{(Eq. 2-42)}$$

With $\delta_{[p][q]}$ the Delta dirac function in discrete notation: $\delta_{[p][q]} = \delta(p\Delta t - q\Delta t)$. Furthermore, the stochastic process $\boldsymbol{x}_{[k]}$ is assumed to be stationary and independent of the noise:

$$\mathbb{E}\left[\boldsymbol{x}_{[k]}\right] = \boldsymbol{0} \tag{Eq. 2-43}$$

$$\mathbb{E}\left[\boldsymbol{x}_{[k]}\boldsymbol{x}_{[k]}^T\right] = \boldsymbol{\Sigma} \tag{Eq. 2-44}$$

$$\mathbb{E}\left[\boldsymbol{x}_{[k]}\boldsymbol{w}_{[k]}^T\right] = \boldsymbol{0} \tag{Eq. 2-45}$$

$$\mathbb{E}\left[\boldsymbol{x}_{[k]}\boldsymbol{v}_{[k]}^T\right] = \boldsymbol{0} \tag{Eq. 2-46}$$

Finally, the output covariance matrices $\boldsymbol{\Lambda}_i \in \mathbb{R}^{n_y \times n_y}$ and the next state – output covariance matrix $\boldsymbol{\mathcal{C}} \in \mathbb{R}^{n_x \times n_y}$ are defined as:

$$\boldsymbol{\Lambda}_i = \mathbb{E}\left[\boldsymbol{y}_{[k+i]}\boldsymbol{y}_{[k]}^T\right] \tag{Eq. 2-47}$$

$$\boldsymbol{\mathcal{C}} = \mathbb{E}\left[\boldsymbol{x}_{[k+i]}\boldsymbol{y}_{[k]}^T\right] \tag{Eq. 2-48}$$

Given these definitions, it can be shown (see e.g. [35], [36]) that the output covariance matrices can be written as:

$$\boldsymbol{\Lambda}_i = \boldsymbol{G_c}\boldsymbol{A}^{i-1}\boldsymbol{\mathcal{C}} \tag{Eq. 2-49}$$

As mentioned in [30], this last relationship implicitly states that the output covariances can be considered as impulse responses of the system. In order to use this relationship for estimating the system matrix $\boldsymbol{A}$, and in consequence the dynamic properties, a Toeplitz matrix $\boldsymbol{T}_{1|i} \in \mathbb{R}^{in_y \times in_y}$ is built:

$$\boldsymbol{T}_{1|i} = \begin{bmatrix} \boldsymbol{\Lambda}_i & \boldsymbol{\Lambda}_{i-1} & \cdots & \boldsymbol{\Lambda}_1 \\ \boldsymbol{\Lambda}_{i+1} & \boldsymbol{\Lambda}_i & \cdots & \boldsymbol{\Lambda}_2 \\ \vdots & \vdots & \ddots & \vdots \\ \boldsymbol{\Lambda}_{2i-1} & \boldsymbol{\Lambda}_{2i-2} & \cdots & \boldsymbol{\Lambda}_i \end{bmatrix} \tag{Eq. 2-50}$$

Note that a Toeplitz matrix is characterised by repeated diagonal terms. This matrix can be expressed as:

$$\boldsymbol{T}_{1|i} = \begin{pmatrix} \boldsymbol{G_c} \\ \boldsymbol{G_c}\boldsymbol{A} \\ \vdots \\ \boldsymbol{G_c}\boldsymbol{A}^{i-1} \end{pmatrix} \begin{pmatrix} \boldsymbol{A}^{i-1}\boldsymbol{\mathcal{C}} & \boldsymbol{A}^{i-2}\boldsymbol{\mathcal{C}} & \cdots & \boldsymbol{A}\boldsymbol{\mathcal{C}} & \boldsymbol{\mathcal{C}} \end{pmatrix} \tag{Eq. 2-51}$$

$$\boldsymbol{\mathcal{O}}_{0|i} = \begin{pmatrix} \boldsymbol{G_c} \\ \boldsymbol{G_c}\boldsymbol{A} \\ \vdots \\ \boldsymbol{G_c}\boldsymbol{A}^{i-1} \end{pmatrix} \tag{Eq. 2-52}$$

With $\boldsymbol{\mathcal{O}}_{0|i} \in \mathbb{R}^{in_y \times n_x}$ the extended observability matrix, which can be estimated by a singular value decomposition of the Toeplitz matrix (see [35], [30], [36]):

$$\boldsymbol{T}_{1|i} = \begin{pmatrix} \boldsymbol{U}_1 & \boldsymbol{U}_2 \end{pmatrix} \begin{pmatrix} \boldsymbol{S}_1 & 0 \\ 0 & 0 \end{pmatrix} \begin{pmatrix} \boldsymbol{V}_1^T \\ \boldsymbol{V}_2^T \end{pmatrix} = \boldsymbol{U}_1\boldsymbol{S}_1\boldsymbol{V}_1^T \Rightarrow \boldsymbol{\mathcal{O}}_{0|i} = \boldsymbol{U}_1\boldsymbol{S}_1^{1/2} \tag{Eq. 2-53}$$

With $\boldsymbol{S}_1 \in \mathbb{R}^{n_x \times n_x}$ a diagonal matrix containing the positive singular values in descending order.

The state matrix $\boldsymbol{A}$ and the output matrix $\boldsymbol{G_c}$ can then be obtained by using the pseudoinverse $(\quad)^\dagger$ and submatrices of the extended observability matrix:

$$\boldsymbol{A} = \boldsymbol{\mathcal{O}}_{0|i-1}^\dagger \boldsymbol{\mathcal{O}}_{1|i} \tag{Eq. 2-54}$$

$$\boldsymbol{G_c} = \boldsymbol{\mathcal{O}}_0 \tag{Eq. 2-55}$$

Finally, the system properties can be obtained by the eigenvalues of the system matrix $\boldsymbol{A}$, and the modal shapes can be obtained considering the output matrix $\boldsymbol{G_c}$:

$$\boldsymbol{A} = \boldsymbol{\Psi}\boldsymbol{\Lambda}_{\mathbf{d}}\boldsymbol{\Psi} \tag{Eq. 2-56}$$

$$\boldsymbol{\Phi} = \boldsymbol{G_c}\boldsymbol{\Psi} \tag{Eq. 2-57}$$

With $\boldsymbol{\Phi} \in \mathbb{C}^{n_y \times n_x}$ the mode shapes referred to the observed points of the structure, and $\boldsymbol{\Lambda_d}$ containing the singular values λ_{d_q}, from which the frequency and damping ratio can be defined (see [30], [28], [36]):

$$\lambda_{c_q} = \frac{\ln\left(\lambda_{d_q}\right)}{\Delta t} \tag{Eq. 2-58}$$

$$\omega_q = \left|\lambda_{c_q}\right| \tag{Eq. 2-59}$$

$$\zeta_q = -\frac{Re\left\{\lambda_{c_q}\right\}}{\left|\lambda_{c_q}\right|} \tag{Eq. 2-60}$$

The following subsections discusses some relevant remarks regarding the application of this method.

2.2.2.1 Stabilisation Diagrams

In the above derivation, a number of singular values n_x was assumed implicitly by the dimension of the system matrix $\boldsymbol{A}$. In practice however, the dimension of the system matrix is not known, and in consequence, the number of singular values is not known a priori.

It is known that the system matrix $\boldsymbol{A}$ has a dimension twice as large as the number of degrees of freedom. Let the model order n_o be defined as the number of degrees of freedom, which in turn means that $n_x = 2n_o$. Note that this ensures that the number of eigenvalues of the system matrix is an even number.

In practice, defining a unique model order n_o for the method is likely to yield several modes that should not be considered as physical modes: spurious modes. The solution that is often adopted is to use several model orders, from which the physical modes can be observed to be present on most of these model orders. To observe this, the stabilisation diagram is used.

The stabilisation diagram is a plot of the frequencies obtained for each model order n_o. The name 'stabilisation' comes from the fact that the physical modes would appear as stable columns in this diagram. Therefore, the physical modes can be recovered by interpreting the results observed from the stabilisation diagram.

2.2.2.2 Covariance Estimation

In order to efficiently compute the Toeplitz matrix $\boldsymbol{T}_{1|i}$, the following Hankel matrix is built by rearranging the outputs:

$$\frac{1}{\sqrt{j}}\begin{pmatrix} \boldsymbol{y}_{[0]} & \boldsymbol{y}_{[1]} & \cdots & \boldsymbol{y}_{[j-1]} \\ \boldsymbol{y}_{[1]} & \boldsymbol{y}_{[2]} & \cdots & \boldsymbol{y}_{[j]} \\ \vdots & \vdots & \ddots & \vdots \\ \boldsymbol{y}_{[i-1]} & \boldsymbol{y}_{[i]} & \cdots & \boldsymbol{y}_{[i+j-2]} \\ \boldsymbol{y}_{[i]} & \boldsymbol{y}_{[i+1]} & \cdots & \boldsymbol{y}_{[i+j-1]} \\ \boldsymbol{y}_{[i+1]} & \boldsymbol{y}_{[i+2]} & \cdots & \boldsymbol{y}_{[i+j]} \\ \vdots & \vdots & \ddots & \vdots \\ \boldsymbol{y}_{[2i-1]} & \boldsymbol{y}_{[2i]} & \cdots & \boldsymbol{y}_{[2i+j-2]} \end{pmatrix} = \begin{pmatrix} \boldsymbol{Y}_{[0|i-1]} \\ \boldsymbol{Y}_{[i|2i-1]} \end{pmatrix} \tag{Eq. 2-61}$$

With $\boldsymbol{Y}_{[0|i-1]}, \boldsymbol{Y}_{[i|2i-1]} \in \mathbb{R}^{in_y \times j}$. Note that a Hankel matrix is a matrix where the antidiagonal terms repeat. The Toeplitz matrix is then obtained as:

$$\boldsymbol{T}_{[1|i]} = \boldsymbol{Y}_{[i|2i-1]} \boldsymbol{Y}_{[0|i-1]}^T \quad \text{(Eq. 2-62)}$$

It is observed that, by using these expressions, the covariance matrices are estimated as:

$$\boldsymbol{\Lambda}_i = \frac{1}{j} \sum_{k=0}^{j-1} \boldsymbol{y}_{[k+i]} \boldsymbol{y}_{[k]}^T \quad \text{(Eq. 2-63)}$$

Which holds under the assumption that $j \to \infty$. Furthermore, the number of lags i considered will control the number of singular values that can be obtained from the Toeplitz matrix. As discussed in [28], the Hankel matrix is defined by setting i as the minimum number of lags to find the desired model order n_o, and thus maximizing j in order to have the best estimation for the covariance matrices from the available observations $\boldsymbol{y}_{[k]}$.

2.2.3 Cluster Analysis

As discussed in section 2.2.2.1, the physical modes are to be interpreted from the stabilisation diagram. The present section shows the methodology employed in order to efficiently interpret it. This methodology is heavily influenced by what is proposed in [34].

The methodology uses two stages: the first stage aims to clear the stabilization diagram by removing spurious modes from it. The second stage aims to identify the clusters that refer to physical modes (i.e., the stable columns).

2.2.3.1 First Stage: Clearing the stabilisation diagram

In order to clear the stabilisation diagram from (definitely) spurious modes, the following rules are implemented:

1) Valid frequency range: $f \in [0, f_{max}]$
2) Valid damping range: $\zeta \in [0, \zeta_{max}]$
3) Presence of conjugates for the poles and mode shapes

Therefore, the modes that don't comply with either of the three rules defined above are considered as spurious modes and removed from the analysis.

2.2.3.2 Second Stage: OPTICS

In order to identify the clusters (stable columns), OPTICS is used. The details of its implementation can be found in [33]. The following procedure is a simplified approach of what has been proposed in [34].

In order to implement OPTICS, the Reachability Distance (RD) needs to be defined. To do so, two distance measures are introduced: Distance between objects $d(i,j)$, and core distance (CD):

2.2.3.2.1 Distance between objects:

The distance between objects is defined as:

$$d(i,j) = \frac{|f_i - f_j|}{f_{max}} + 1 - MAC(\boldsymbol{\phi}_i, \boldsymbol{\phi}_j) + d_o(i,j) \quad \text{(Eq. 2-64)}$$

With f_i, f_j representing the frequency identified (obtained after clearing the stabilisation diagram) for any two pair of frequencies. f_{max} the maximum frequency allowed (defined in the previous subsection). $\boldsymbol{\phi}_i, \boldsymbol{\phi}_j$ the associated complex mode shapes and MAC refers to the Modal Assurance Criterion (see e.g. [37]) defined as:

$$MAC(\boldsymbol{\phi}_i, \boldsymbol{\phi}_j) = \frac{\left|\boldsymbol{\phi}_i^H \boldsymbol{\phi}_j\right|^2}{(\boldsymbol{\phi}_i^H \boldsymbol{\phi}_i)(\boldsymbol{\phi}_j^H \boldsymbol{\phi}_j)} \quad \text{(Eq. 2-65)}$$

With $(\quad)^H$ representing the Hermitian of the vector. The MAC takes values from 0 (when there is no consistent correspondence) to 1 (when there is perfect correspondence). The distance between frequencies is normalized to obtain comparable values with the MAC.

Finally, $d_o(i,j)$ is a measure of distance in terms of the model order. If the two objects have the same model order it takes a value of 1, otherwise it takes a value of 0. This helps in avoiding clustering objects in the same model order.

2.2.3.2.2 Core Distance:

The core distance (CD) depends on a parameter called $MinObj$, which indicates the minimum number of objects that a cluster should have. The core distance is the distance (measured by $d(i,j)$) at which $MinObj$ objects can be found. The computation is illustrated in Figure 2-2. A formal expression for it can be found in [34].

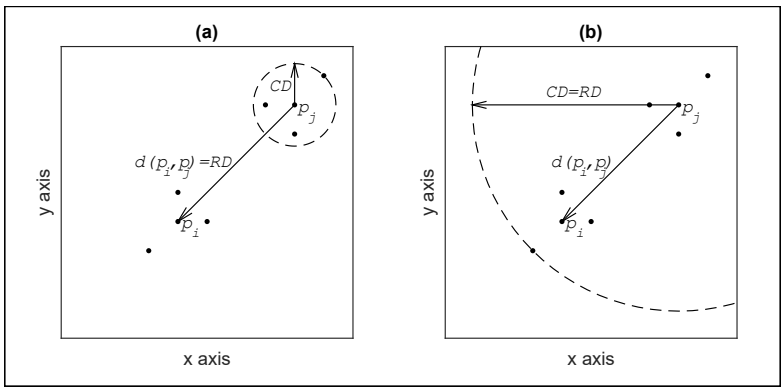

Figure 2-2. Reachability Distance (RD) and Core Distance (CD) illustration. (a) considering $MinObj = 4$, (b) considering $MinObj = 8$. Ref.: [34].

2.2.3.2.3 Reachability Distance and Reachability Plot:

The Reachability Distance (RD) is defined as the maximum between the core distance and the distance between objects:

$$RD(i,j) = \max\{CD(j), d(i,j)\} \quad \text{(Eq. 2-66)}$$

OPTICS uses this definition to build a reachability plot. The reachability plot is defined iteratively. In simple words it is defined by computing the RD between the (remaining) objects, selecting the object with the minimum RD and excluding it from the next step in the iteration. This defines an order for the objects. The specific algorithm used can be found in [34], [33].

The Reachability plot is the result of using OPTICS. Clusters are identified by low RD value regions. The lower the RD the denser the cluster is (in terms of the distance previously defined).

2.2.3.2.4 Cluster detection from reachability plots

In order to efficiently detect low RD value regions, a simplified version of what is proposed in [34] is implemented. First, steep objects need to be defined. Let s_i denote the difference between consecutive objects in the reachability plot. Let $\xi_s = \frac{mean(|s_i|)}{2}$. Downwards steep objects are defined as the objects for which $s_i < -\xi_s$, and conversely, upwards steep objects are defined as the objects for which $s_i > \xi_s$.

Clusters can then be defined as the elements between a downwards steep object and an upwards steep object, as long as the number of elements that the formed cluster has at least $MinObj$ objects.

2.2.3.2.5 Remarks

The main parameter to be defined to implement OPTICS is $MinObj$. Following the recommendations in [34], this parameter can be defined by the number of model orders that the stable columns should be present at. Let the range of model orders be $n_{o,r} = \max(n_o) - \min(n_o)$. Then, $MinObj$ can be defined as:

$$MinObj = \alpha_{MinObj} n_{o,r} \quad \text{(Eq. 2-67)}$$

Where α_{MinObj} should take at most a value of $\alpha_{MinObj} = 1$ when the stable columns are expected to be present across the whole range of model orders, and a lower value when the stable columns are expected to be present only partially across the model orders.

2.2.3.3 Third Stage: Representative element

The final step of this methodology is to define a representative element from the clusters identified in the second stage. The representative element is chosen as the median values in frequency, damping ratio and mode shape.

2.3 Modal Decomposition and Expansion

The MD&E can be found in [17]. The method starts by noticing that the observed accelerations can be related to the modal coordinates of a mechanical model (see section 2.1.2.2 and 2.1.3.1):

$$\boldsymbol{y}(t) = \boldsymbol{S_{am}} \ddot{\boldsymbol{u}}_{\boldsymbol{m}}(t) \quad \text{(Eq. 2-68)}$$

It is therefore possible to estimate the acceleration modal coordinates at any point in time by computing the pseudo-inverse:

$$\ddot{\boldsymbol{u}}_{\boldsymbol{m}}(t) = \boldsymbol{S_{am}}^{\dagger} \boldsymbol{y}(t) = \left(\boldsymbol{S_{am}}^{\mathrm{T}} \boldsymbol{S_{am}}\right)^{-1} \boldsymbol{S_{am}}^{T} \boldsymbol{y}(t) \quad \text{(Eq. 2-69)}$$

Note that this requires that the number of modes n_m considered to be less than or equal to the number of observations n_y: $n_m \leq n_y$ so as to avoid defining an underdetermined system (less equations than unknowns).

The displacement modal coordinate is required to define the strains. This can be computed, as proposed in [5], by integration in the frequency domain:

$$\boldsymbol{u}_{\boldsymbol{m}}(t) = \mathcal{F}^{-1}\left\{\frac{1}{-\omega^2}\mathcal{F}\{\ddot{\boldsymbol{u}}_{\boldsymbol{m}}(t)\}\right\} \quad \text{(Eq. 2-70)}$$

From which the strains can be obtained:

$$\varepsilon(t) = \boldsymbol{S_{\varepsilon m}} \boldsymbol{u}_{\boldsymbol{m}}(t) \quad \text{(Eq. 2-71)}$$

With $\boldsymbol{S_{\varepsilon m}}$ the modal selection matrix as defined in 2.1.3.1.

There are three points that should be considered in the implementation of this method:

1) The error (noise) of the observation $\boldsymbol{y}$ is not taken into account. This will yield errors in the estimation of the modal coordinate depending on the amount of noise. To minimise this error, the system is sought to be solved in a least-square sense (overdetermined system: $n_m < n_y$).
2) Integration in the frequency domain will amplify low frequencies. To avoid this, the signal is filtered after integrating.
3) Ill-conditioning of the matrix $\boldsymbol{S_{am}}$ may amplify the noise in the results.

2.4 Gaussian Process Latent Force Model

2.4.1 Introduction

The GPLFM is a model that combines a mechanical model of the structure with a stochastic characterisation of the unknown input. A flowchart representing the main considerations for the GPLFM is presented in Figure 2-3. The mechanical model represents the structure, and the equation is as defined in section 2.1. The stochastic model represents the load, and it is written in state space form (see section 2.4.3). The augmented model is a combination of both the mechanical and stochastic model (see section 2.4.4). The augmented model is a stochastic differential equation for the augmented state vector $\boldsymbol{z^a}$ which contains the modal displacements, modal velocities, and the state vector for the load. The augmented state vector is a stochastic variable, and in consequence the expected value and the covariance are of relevance. The prior refers to the marginal distribution obtained for the augmented vector at any point in time, and the posterior refers to the conditional distribution of the state vector upon some information regarding the system. The posterior distribution is computed by employing Kalman Filter and Smoothing algorithms. The result of the GPLFM is therefore the new marginal distribution obtained through the posterior distribution.

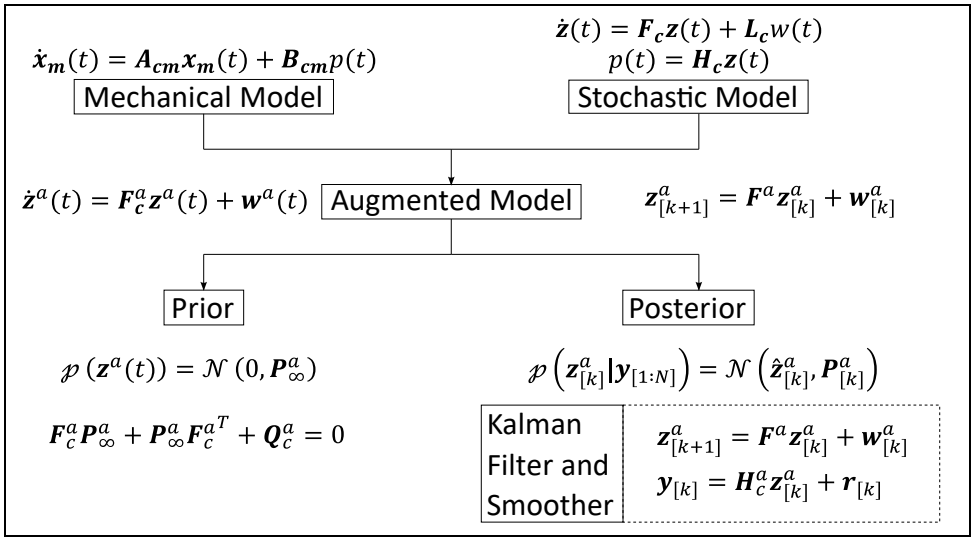

Figure 2-3. GPLFM flowchart.

The present section aims to present the GPLFM method in detail. Taking into account that the amount of theoretical background required is considerable, an outline is indicated below:

1) Gaussian Process: Gaussian processes are introduced in a simplistic manner, along with recalling some relevant properties of the Multivariate Normal distribution. Furthermore, two particular gaussian processes are presented: The white gaussian noise and a process driven by a Matérn covariance function. Finally, the concept of prior and posterior is introduced.

2) Stochastic State Space Model: The state space model representation of a stochastic process is presented. The prior and posterior are revisited in this context.

3) Augmented State Space Model: The augmentation of the mechanical and stochastic state space models is presented. This is the core of the GPLFM method. The prior and posterior is again revisited for this model.

4) Parameter estimation: The hyperparameters of the stochastic load and the noise levels must be defined. Two methodologies to estimate these parameters are presented. The first falls in line with what has been proposed in literature, and the second is a novel proposed methodology considered in this work.

2.4.2 Gaussian Process

The aim of this section is to provide a sufficient understanding of gaussian processes.

Let $p(\boldsymbol{x})$ denote the probability distribution of a random variable $\boldsymbol{x}$.

The distribution of interest in the context of this work is the Multivariate Gaussian probability distribution (or joint normal distribution) of a random variable $\boldsymbol{x} \in \mathbb{R}^n$ given by:

$$p(\boldsymbol{x}) = \mathcal{N}(\hat{\boldsymbol{x}}, \boldsymbol{\Upsilon}) = \frac{1}{\sqrt{2\pi \det(\mathbf{K})}} \exp\left(-\frac{1}{2}(\boldsymbol{x} - \hat{\boldsymbol{x}})^T \boldsymbol{\Upsilon}^{-1} (\boldsymbol{x} - \hat{\boldsymbol{x}})\right) \quad \text{(Eq. 2-72)}$$

Where $\hat{\boldsymbol{x}} \in \mathbb{R}^n$ is the mean and $\boldsymbol{\Upsilon} \in \mathbb{R}^{n \times n}$ is the covariance matrix, formally defined as:

$$\hat{\boldsymbol{x}} = \mathbb{E}[\boldsymbol{x}] \quad \text{(Eq. 2-73)}$$

$$\boldsymbol{\Upsilon} = \mathbb{E}[(\boldsymbol{x} - \hat{\boldsymbol{x}})(\boldsymbol{x} - \hat{\boldsymbol{x}})^T] \quad \text{(Eq. 2-74)}$$

Where $\mathbb{E}[\quad]$ corresponds to the expected value operator.

A gaussian process $x(t)$ can be roughly understood by considering a vector with infinitely many elements [38], corresponding to the values that it takes in time: $x(t) \rightarrow \boldsymbol{x} \in \mathbb{R}^{\infty}$. A gaussian process can therefore be characterised by a mean value $\hat{x}(t) \rightarrow \hat{\boldsymbol{x}} \in \mathbb{R}^{\infty}$ and a covariance function $\kappa(t, t') \rightarrow \boldsymbol{\Upsilon} \in \mathbb{R}^{\infty \times \infty}$. The covariance function will define the correlation between time t and t'. This notion is recovered by using the following notation:

$$x(t) \sim \mathcal{GP}\left(\hat{x}(t), \kappa(t, t')\right) \quad \text{(Eq. 2-75)}$$

Using infinite vectors is, of course, not feasible in practice. However, considering a discrete subset of time, it can be reduced to a multivariate gaussian distribution.

Furthermore, it is noted that when the statistics (mean and covariance) of the gaussian process do not vary in time it is called stationary. This implies that the mean has a constant value for all points in time: $\hat{x}(t) = \hat{x}$ and that the covariance function will depend only on the time lag $\tau = |t - t'|$ regardless at which point in time it is evaluated: $\kappa(t, t') = \kappa(\tau)$. Then, a stationary gaussian process can be written as:

$$x(t) \sim \mathcal{GP}\left(\hat{x}, \kappa(\tau)\right) \quad \text{(Eq. 2-76)}$$

Note that all gaussian process used in this work are stationary.

2.4.2.1 Multivariate Normal Distribution

Given the relevance of the Multivariate Gaussian distribution for Gaussian Processes, some basic properties are recalled. To do so, a simpler version of the Multivariate Gaussian distribution is considered:

$$p\left(\begin{bmatrix} a \\ b \end{bmatrix}\right) = \mathcal{N}\left(\begin{bmatrix} \hat{a} \\ \hat{b} \end{bmatrix}, \begin{bmatrix} \kappa_a & \kappa_{ab} \\ \kappa_{ab}{}^T & \kappa_b \end{bmatrix}\right) \quad \text{(Eq. 2-77)}$$

Note that a and b can be considered as vectors or as scalars.

2.4.2.1.1 Marginal Distribution

The marginal distribution can be understood as the distribution of a variable independent of other events. For each variable, the marginal distribution can be obtained directly from the joint distribution:

$$p(a) = \mathcal{N}(\hat{a}, \kappa_a) \quad \text{(Eq. 2-78)}$$

$$p(b) = \mathcal{N}\left(\hat{b}, \kappa_b\right) \quad \text{(Eq. 2-79)}$$

2.4.2.1.2 Conditional distribution

The conditional distribution can be understood as an update of the probability distribution when information is known for dependant variables. Considering the simpler version above, the distribution of the variable a can be updated if the variable b is known:

$$p(a|b) = \mathcal{N}\left(\hat{a} + \kappa_{ab}\kappa_b^{-1}\left(b - \hat{b}\right), \kappa_a - \kappa_{ab}\kappa_b^{-1}\kappa_{ab}^T\right) \quad \text{(Eq. 2-80)}$$

2.4.2.2 White Gaussian Noise

A frequently used Gaussian Process is the White Gaussian Process. It is defined by a zero mean $\hat{x}(t) = 0$ with a covariance function given by $\kappa(\tau) = \sigma_w^2\delta(\tau)$.

Therefore, white noise is defined as: $w(t) \sim \mathcal{GP}\left(0, \kappa(\tau) = \sigma_w^2\delta(\tau)\right)$. With $\delta(\ \ )$ refers to the Dirac delta function.

if a discrete subset of time is considered: $\{t_1, t_2\} \rightarrow \{w_1 = w(t_1), w_2 = w(t_2)\}$, the multivariate probability distribution can be expressed as:

$$p\left(\begin{bmatrix} w_1 \\ w_2 \end{bmatrix}\right) = \mathcal{N}\left(\begin{bmatrix} 0 \\ 0 \end{bmatrix}, \sigma_w^2 \begin{bmatrix} 1 & 0 \\ 0 & 1 \end{bmatrix}\right) \quad \text{(Eq. 2-81)}$$

Considering the expressions defined for the marginal distribution:

$$p(w_k) = \mathcal{N}(0, \sigma_w^2) \quad \text{(Eq. 2-82)}$$

Furthermore, the conditional distribution is given by:

$$p\left(w_k \middle| w_j\right) = p(w_k) \quad (k \neq j) \quad \text{(Eq. 2-83)}$$

These results indicate that at any point in time the probability distribution is the same, regardless of the information known at any other point in time.

For simplicity, a White Gaussian Process is denoted as:

$$w(t) \sim \mathcal{N}(0, \sigma_w^2) \quad \text{(Eq. 2-84)}$$

It is highlighted that σ_w^2 does not refer to the variance directly. It refers to the spectral density. The variance is obtained from integration of the spectral density over all frequencies, which in this case would be infinite. In the discrete case however, the spectral density can be considered as the variance of the marginal distribution as illustrated above:

$$w_{[k]} \sim \mathcal{N}(0, \sigma_w^2) \quad \text{(Eq. 2-85)}$$

2.4.2.3 Matern32 Covariance Function

A particular covariance function is considered in this work, named the Matern32 covariance function. The use of this covariance function rise from the fact that it offers great flexibility in modelling different types of random processes (See [18], [19]).

The Matern32 covariance function is a specific function belonging to the Matérn family of covariance functions. The general expression for the family of functions can be found in [38]. The specific function is defined as:

$$\kappa_{M32}(\tau; \sigma, l_{sc}) = \sigma^2 \left\{1 + \frac{\sqrt{3}|\tau|}{l_{sc}}\right\} e^{\left(-\frac{\sqrt{3}|\tau|}{l_{sc}}\right)} \quad \text{(Eq. 2-86)}$$

And the spectral density is given by [39]:

$$S_{M32}(f; \sigma^2, l_{sc}) = \sigma^2 \frac{12\sqrt{3}}{l_{sc}^3}\left(\frac{3}{l_{sc}^2} + (2\pi f)^2\right)^{-2} \quad \text{(Eq. 2-87)}$$

This covariance function is defined not only by the time lag τ, but also by two hyperparameters: σ and l_{sc}. These hyperparameters are described as follows:

- σ: known as the magnitude. It controls the amplitude of the covariance function. Notice that $\kappa_{M32}(0) = \sigma^2$, which means that the marginal distribution of the stochastic process $p(t)$ defined by this covariance function has a variance of σ^2: $\mathcal{p}\big(p(t)\big) = \mathcal{N}(0, \sigma^2)$.
- l_{sc}: known as the length scale, controls the extent of the correlation. Note that, from the covariance function, it can be observed that for a given l_{sc} a significant correlation may be found up to $5l_{sc}$. Furthermore, from the spectral density, the expected frequency content may be considered significant up to $f \sim 1/5l_{sc}$, which is below the half-power point.

Figure 2-4 illustrates the Matern32 covariance function in terms of the covariance function, spectral density, and some samples to illustrate the behaviour of a process described by this covariance function.

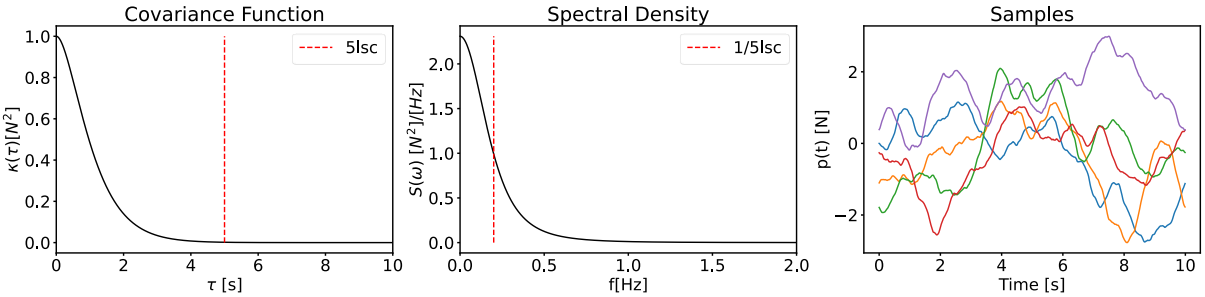

Figure 2-4. Matern32 covariance function, spectral density and samples.
$\boldsymbol{\sigma = 1[N], l_{sc} = 1[s]}$.

2.4.2.4 Prior and Posterior

Consider a stochastic process $p(t) \sim \mathcal{GP}\big(0, \kappa(\tau)\big)$. This characterisation of the process can be understood as setting some 'prior belief' for the function: it is expected to have a zero-mean and a covariance given by $\kappa(\tau)$. The marginal distribution: $\mathcal{p}\big(p(t)\big) = \mathcal{N}\big(0, \kappa(0)\big)$ is referred to hereafter as the 'prior'. It is highlighted that this definition provides only partial information regarding the 'prior belief', as it provides no information regarding the correlation in time (i.e., regarding the covariance function for $\tau \neq 0$). Figure 2-5 shows the prior through the mean value and the 3σ interval of confidence for the Matern32 covariance function with unitary values for σ and l_{sc}.

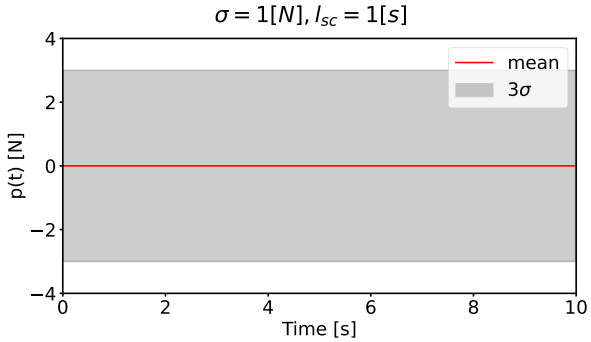

Figure 2-5. Prior. Matern32 covariance function.
$\boldsymbol{\sigma = 1[N]}$ **and** $\boldsymbol{l_{sc} = 1[s]}$.

Any two points in time have a joint distribution given by:

$$\mathcal{p}\left(\begin{bmatrix} p(t_1) \\ p(t_2) \end{bmatrix}\right) = \mathcal{N}\left(\begin{bmatrix} 0 \\ 0 \end{bmatrix}, \begin{bmatrix} \kappa_0 = \kappa(0) & \kappa_\tau = \kappa(\tau = |t_1 - t_2|) \\ \kappa_\tau = \kappa(\tau = |t_1 - t_2|) & \kappa_0 = \kappa(0) \end{bmatrix}\right) \quad \text{(Eq. 2-88)}$$

If the stochastic process is measured at some point in time, it is reasonable to think that the 'prior belief' should be updated, because there is more information regarding the process. Updating beliefs with the new information is the same as computing the conditional distribution on the observations. This would update the values for the mean and covariance at any point in time. To illustrate this, let $p(t_1) = p_1$ be known, or in words: let the stochastic process be measured at time t_1. Furthermore, let $p(t_2)$ refer to any point in time: $p(t_2) = p(t)$, then, using the conditional distribution:

$$\mathcal{p}(p(t)|p_1) = \mathcal{N}(\hat{p}(t) = \kappa_\tau {\kappa_0}^{-1} p_1, \kappa(t) = \kappa_0 - \kappa_\tau {\kappa_0}^{-1} \kappa_\tau) \quad \text{(Eq. 2-89)}$$

The updated distribution has a mean $\hat{p}(t)$ and a covariance $\kappa(t)$ that varies in time. in particular, it varies as a function of the time lag: $\tau = |t_1 - t|$.

This conditional distribution is referred to hereafter as the 'posterior'. Figure 2-6 shows the posterior for the Matern32 covariance function with unitary values and considering a single observation. Note that the closer to the observation, the less uncertainty there is (to the extreme of zero uncertainty at the observed point) and the farther from the observation the more uncertainty there is (to the extreme of recovering the prior).

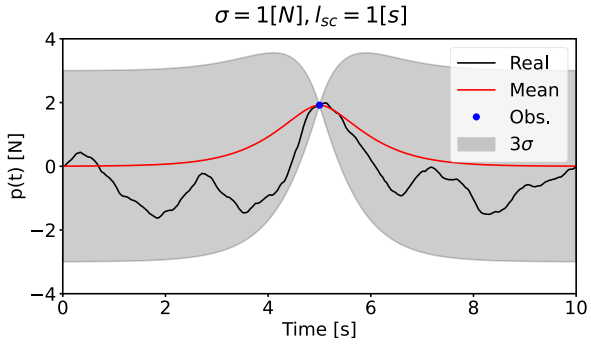

Figure 2-6. Posterior. Matern32 covariance function. $\boldsymbol{\sigma = 1[N]}$ and $\boldsymbol{l_{sc} = 1[s]}$.

2.4.3 Stochastic State Space Model

The main motivation for formulating a stochastic state space model is to be able to combine it (augment it) mathematically with the mechanical state space model. The reason why it was developed however is because the computational effort required to compute the posterior increases rapidly with the number of measurements. This representation reduces the computational cost from $\mathcal{O}(n^3)$ to $\mathcal{O}(n)$ [39], with n referring to the number of measurements.

In order to construct the stochastic state space model, it is required to first define the gaussian process $p(t) \sim \mathcal{GP}(0, \kappa(\tau))$ as the output of a Linear Time Invariant Stochastic Differential Equation. A methodology to do so is presented in [39]. The following focuses on the Matern32 covariance function.

2.4.3.1 Continuous-Time Stochastic State Space Model

A gaussian process with a Matern32 covariance function can be expressed as the output of the following Linear Time Invariant Stochastic Differential Equation [39]:

$$\ddot{p}(t) + \left(2\frac{\sqrt{3}}{l_{sc}}\right)\dot{p}(t) + \left(\frac{3}{l_{sc}^2}\right)p(t) = w(t) \quad \text{(Eq. 2-90)}$$

Note that it is a stochastic differential equation as it is driven by a white gaussian noise $w(t)$ with a known spectral density:

$$w(t) \sim \mathcal{N}\left(0, \sigma_w^2 = \frac{12\sqrt{3}\sigma^2}{l_{sc}^3}\right) \quad \text{(Eq. 2-91)}$$

This can be written as a continuous-time state space model:

$$\dot{\boldsymbol{z}}(t) = \boldsymbol{F_c}\boldsymbol{z}(t) + \boldsymbol{L_c}w(t) \quad \text{(Eq. 2-92)}$$

$$p(t) = \boldsymbol{H_c}\boldsymbol{z}(t) \quad \text{(Eq. 2-93)}$$

With:

$$\boldsymbol{z}(t) = \begin{bmatrix} p(t) \\ \dot{p}(t) \end{bmatrix} \quad \text{(Eq. 2-94)}$$

$$\boldsymbol{F_c} = \begin{bmatrix} 0 & 1 \\ -\frac{3}{l_{sc}^2} & -2\frac{\sqrt{3}}{l_{sc}} \end{bmatrix} \quad \text{(Eq. 2-95)}$$

$$\boldsymbol{L_c} = \begin{bmatrix} 0 \\ 1 \end{bmatrix} \quad \text{(Eq. 2-96)}$$

$$\boldsymbol{H_c} = \begin{bmatrix} 1 & 0 \end{bmatrix} \quad \text{(Eq. 2-97)}$$

2.4.3.2 Prior: Stationary solution

It is not direct how the prior can be recovered from the state space representation of the stochastic process. Therefore, the prior is revisited in this context.

Notice first that $\boldsymbol{z}(t)$ is also a stochastic process, it therefore has a mean $\hat{\boldsymbol{z}}(t) = \mathbb{E}[\boldsymbol{z}(t)]$ and covariance $\boldsymbol{P}(t) = \mathbb{E}[\boldsymbol{z}(t)\boldsymbol{z}(t)^T]$. Expressions that define these statistics can be found through the stochastic state space model [40]:

$$\dot{\hat{\boldsymbol{z}}}(t) = \boldsymbol{F_c}\hat{\boldsymbol{z}}(t) \quad \text{(Eq. 2-98)}$$

$$\dot{\boldsymbol{P}}(t) = \boldsymbol{F_c}\boldsymbol{P}(t) + \boldsymbol{P}(t)\boldsymbol{F_c}^T + \boldsymbol{L_c}\sigma_w^2\boldsymbol{L_c}^T \quad \text{(Eq. 2-99)}$$

The prior can be recovered from the stationary solutions of these expressions [40]. The stationary solutions, noted by $\hat{\boldsymbol{z}}_\infty$ and $\boldsymbol{P}_\infty$, are obtained by imposing that the rate of change is zero, yielding the following expressions:

$$\boldsymbol{F_c}\hat{\boldsymbol{z}}_\infty = \boldsymbol{0} \quad \text{(Eq. 2-100)}$$

$$\boldsymbol{F_c}\boldsymbol{P}_\infty + \boldsymbol{P}_\infty\boldsymbol{F_c}^T + \boldsymbol{L_c}\sigma_w^2\boldsymbol{L_c}^T = \boldsymbol{0} \quad \text{(Eq. 2-101)}$$

By observing the first equation, it is direct that the stationary solution for the expected value is zero $\hat{\boldsymbol{z}}_\infty = \boldsymbol{0}$, which relates directly with the stationary solution of the stochastic process: $\hat{p}_\infty = \boldsymbol{H_c}\hat{\boldsymbol{z}}_\infty = 0$. The second equation provides an expression that can be used to find the stationary covariance. This equation is known as the continuous-time Lyapunov equation and can be solved numerically. It is highlighted that the covariance of the stochastic process can therefore be obtained as: $\mathbb{E}[p(t)p(t)^T] = \boldsymbol{H_c}\boldsymbol{P}_\infty\boldsymbol{H_c^T} = \sigma^2$. In other words, the prior is regained: $\mathcal{p}\big(p(t)\big) = \mathcal{N}(0, \sigma^2)$.

2.4.3.3 Posterior: Kalman Filter and Smoother

Computing the posterior through the stochastic state space model requires defining the discrete version of the stochastic model, and an observation equation which will provide the information of the system to compute the posterior. Subsequently, the posterior can be computed recursively by employing Kalman Filter and Smoothing.

The expressions found for the statistics can be solved, as they are ordinary differential equations. The solution can be expressed as [40]:

$$\hat{\boldsymbol{z}}(t) = \boldsymbol{e}^{\boldsymbol{F_c}(t-t_0)}\hat{\boldsymbol{z}}(t_0) \quad \text{(Eq. 2-102)}$$

$$\boldsymbol{P}(t) = \boldsymbol{e}^{\boldsymbol{F_c}(t-t_0)}\boldsymbol{P}(t_0)\boldsymbol{e}^{\boldsymbol{F_c}(t-t_0)^T} + \int_{t_0}^{t} \boldsymbol{e}^{\boldsymbol{F_c}(t-\tau)}\boldsymbol{L_c}\sigma_w^2\boldsymbol{L_c}^T\boldsymbol{e}^{\boldsymbol{F_c}(t-\tau)^T}d\tau \quad \text{(Eq. 2-103)}$$

Using discrete notation, and evaluating between time steps:

$$\hat{\boldsymbol{z}}_{[k+1]} = \boldsymbol{F}\hat{\boldsymbol{z}}_{[k]} \quad \text{(Eq. 2-104)}$$

$$\boldsymbol{P}_{[k+1]} = \boldsymbol{F}\boldsymbol{P}_{[k]}\boldsymbol{F}^T + \boldsymbol{Q_d} \quad \text{(Eq. 2-105)}$$

With:

$$\boldsymbol{F} = \boldsymbol{e}^{\boldsymbol{F_c}\Delta t} \quad \text{(Eq. 2-106)}$$

$$\boldsymbol{Q_d} = \int_{k\Delta t}^{(k+1)\Delta t} \boldsymbol{e}^{\boldsymbol{F_c}((k+1)\Delta t-\tau)}\boldsymbol{L_c}\sigma_w^2\boldsymbol{L_c}^T\boldsymbol{e}^{\boldsymbol{F_c}((k+1)\Delta t-\tau)^T}d\tau \quad \text{(Eq. 2-107)}$$

The expressions obtained for the statistics define an equivalent discrete version of the system:

$$\boldsymbol{z}_{[k+1]} = \boldsymbol{F}\boldsymbol{z}_{[k]} + \boldsymbol{w}_{[k]} \quad \text{(Eq. 2-108)}$$

With $\boldsymbol{w}_{[k]} \sim \mathcal{N}(0, \boldsymbol{Q_d})$, uncorrelated from the states.

In order to compute the posterior, an observation equation is defined. Let some discrete set of observations be defined as:

$$y_{[k]} = \boldsymbol{H_c}\boldsymbol{z}_{[k]} + r_{[k]} \quad \text{(Eq. 2-109)}$$

With $r_{[k]} \sim \mathcal{N}(0, R)$ a white gaussian noise to represent some error in the observations.

As mentioned in [39], the posterior can be computed by employing Kalman Filtering and Smoothing upon the discrete model and observation equation using the stationary solutions as initial values. Table 2-1 summarises the relevant equations (the derivation of them can be found in [39]).

Table 2-1. Kalman filter and smoother equations. Stochastic model.

Time Update:	Measurement Update:	Smoothing:
$p(\boldsymbol{z}_{[k]}\|y_{[1:k-1]}) = \mathcal{N}(\hat{\boldsymbol{z}}_{[k]}^-, \boldsymbol{P}_{[k]}^-)$	$p(\boldsymbol{z}_{[k]}\|y_{[1:k]}) = \mathcal{N}(\hat{\boldsymbol{z}}_{[k]}^+, \boldsymbol{P}_{[k]}^+)$ $p(y_{[1:k]}\|y_{[1:k-1]}) = \mathcal{N}(\boldsymbol{H_c}\hat{\boldsymbol{z}}_{[k]}^-, S_{[k]})$	$p(\boldsymbol{z}_{[k]}\|y_{[1:N]}) = \mathcal{N}(\hat{\boldsymbol{z}}_{[k]}, \boldsymbol{P}_{[k]})$
$\hat{\boldsymbol{z}}_{[k]}^- = \boldsymbol{F}\hat{\boldsymbol{z}}_{[k-1]}^+$ $\boldsymbol{P}_{[k]}^- = \boldsymbol{F}\boldsymbol{P}_{[k-1]}^+\boldsymbol{F}^T + \boldsymbol{Q_d}$	$r_{[k]} = y_{[k]} - \boldsymbol{H_c}\hat{\boldsymbol{z}}_{[k]}^-$ $S_{[k]} = \boldsymbol{H_c}\boldsymbol{P}_{[k]}^-\boldsymbol{H_c}^T + R$ $\boldsymbol{K}_{[k]} = \boldsymbol{P}_{[k]}^-\boldsymbol{H_c}^T(S_{[k]})^{-1}$ $\hat{\boldsymbol{z}}_{[k]}^+ = \hat{\boldsymbol{z}}_{[k]}^- + \boldsymbol{K}_{[k]}r_{[k]}$ $\boldsymbol{P}_{[k]}^+ = \boldsymbol{P}_{[k]}^- - \boldsymbol{K}_{[k]}S_{[k]}\boldsymbol{K}_{[k]}^T$	$\boldsymbol{C}_{[k]} = \boldsymbol{P}_{[k]}^+\boldsymbol{F}^T(\boldsymbol{P}_{[k+1]}^-)^{-1}$ $\hat{\boldsymbol{z}}_{[k]} = \hat{\boldsymbol{z}}_{[k]}^+ + \boldsymbol{C}_{[k]}(\hat{\boldsymbol{z}}_{[k+1]} - \hat{\boldsymbol{z}}_{[k+1]}^-)$ $\boldsymbol{P}_{[k]} = \boldsymbol{P}_{[k]}^+ + \boldsymbol{C}_{[k]}(\boldsymbol{P}_{[k+1]} - \boldsymbol{P}_{[k+1]}^-)\boldsymbol{C}_{[k]}^T$

In words, the Time Update step computes the mean and covariance of the distribution conditional on all past observations: $p(\boldsymbol{z}_{[k]}|y_{[1:k-1]}) = \mathcal{N}(\hat{\boldsymbol{z}}_{[k]}^-, \boldsymbol{P}_{[k]}^-)$. The Measurement Update step computes the mean and covariance of the distribution conditional on all past observations, including the observation in the current step: $p(\boldsymbol{z}_{[k]}|y_{[1:k]}) = \mathcal{N}(\hat{\boldsymbol{z}}_{[k]}^+, \boldsymbol{P}_{[k]}^+)$. Note that if there are no observation this step is omitted: $\hat{\boldsymbol{z}}_{[k]}^+ = \hat{\boldsymbol{z}}_{[k]}^-, \boldsymbol{P}_{[k]}^+ = \boldsymbol{P}_{[k]}^-$. Finally, the Smoothing step computes the mean and covariance of the distribution conditional on all observations: $p(\boldsymbol{z}_{[k]}|y_{[1:N]}) = \mathcal{N}(\hat{\boldsymbol{z}}_{[k]}, \boldsymbol{P}_{[k]})$. The result from the Smoothing step is therefore the posterior as defined in 2.4.2.4, but written in discrete notation.

The regression process is illustrated in Figure 2-7. An unknown function is first shown in black, and a prior belief is set by $p(t) \sim \mathcal{GP}(0, \kappa_{M32}(\tau; \sigma = 1[N], l_{sc} = 1[s]))$. A point is observed, and the Kalman Filter is applied, updating points in time after the observation. Finally, the smoother is applied to update points in time before the observation.

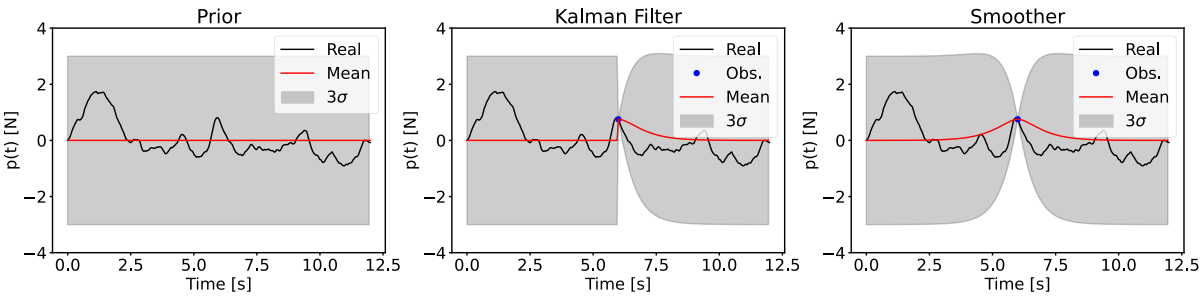

Figure 2-7. Posterior defined through Kalman Filter and Smoother.

2.4.4 Augmented State Space Model

The main model that drives the GPLFM is the augmented state space model. This is a combination of the mechanical model that represents the structure, and a stochastic model that represents the load. It is relevant to notice that the result will also be a stochastic model. In consequence a prior and a posterior can be computed. The augmented model is described in the following.

2.4.4.1 Continuous-time Augmented State Space Model

Starting from the continuous-time state space representation of the mechanical model:

$$\dot{\boldsymbol{x}}(t) = \boldsymbol{A_c}\boldsymbol{x}(t) + \boldsymbol{B_c}p(t) \qquad \text{(Eq. 2-110)}$$

Considering only one load. The stochastic state space model is defined by:

$$\dot{\boldsymbol{z}}(t) = \boldsymbol{F_c}\boldsymbol{z}(t) + \boldsymbol{L_c}w(t) \qquad \text{(Eq. 2-111)}$$

$$p(t) = \boldsymbol{H_c}\boldsymbol{z}(t) \qquad \text{(Eq. 2-112)}$$

Both state space models can be combined into an augmented version:

$$\begin{bmatrix}\dot{\boldsymbol{x}}(t)\\ \dot{\boldsymbol{z}}(t)\end{bmatrix} = \begin{bmatrix}\boldsymbol{A_c} & \boldsymbol{B_c}\boldsymbol{H_c}\\ 0 & \boldsymbol{F_c}\end{bmatrix}\begin{bmatrix}\boldsymbol{x}(t)\\ \boldsymbol{z}(t)\end{bmatrix} + \begin{bmatrix}\boldsymbol{0}\\ \boldsymbol{L_c}w(t)\end{bmatrix} \qquad \text{(Eq. 2-113)}$$

In short notation:

$$\dot{\boldsymbol{z}}^{\boldsymbol{a}}(t) = \boldsymbol{F_c^a}\boldsymbol{z}^{\boldsymbol{a}}(t) + \boldsymbol{w}^{\boldsymbol{a}}(t) \qquad \text{(Eq. 2-114)}$$

With $\boldsymbol{w}^{\boldsymbol{a}}(t) \sim \mathcal{N}(0, \boldsymbol{Q_c^a})$

$$\boldsymbol{Q_c^a} = \begin{bmatrix}0 & 0\\ 0 & L_c\sigma_w^2 L_c^T\end{bmatrix} \qquad \text{(Eq. 2-115)}$$

It is highlighted that the structure of this expression is completely analogous to the stochastic state space model presented for the load. Note that the augmented state $\boldsymbol{z}^{\boldsymbol{a}}(t)$ is a stochastic variable which contains not only the stochastic description of the load, but also a stochastic description of the response (in terms of modal displacements and velocities). The stochastic description of the response is defined taking into account the mechanical model and the stochastic description of the load. In other words: through the augmented model.

Furthermore, it is noted that only one load has been defined for the augmented model. More loads may be considered by further augmentation (see [18]). The simulation and real case structure are modelled by considering only one load, so the increased augmentation is omitted for simplicity.

2.4.4.2 Prior: Stationary solution

Similar to what was exposed in Section 2.4.3.2, expressions for the statistics are found through the augmented model:

$$\dot{\hat{\boldsymbol{z}}}^{a}(t) = \boldsymbol{F_c^a}\hat{\boldsymbol{z}}^{a}(t) \qquad \text{(Eq. 2-116)}$$

$$\dot{\boldsymbol{P}}^a(t) = \boldsymbol{F}_c^a \boldsymbol{P}^a(t) + \boldsymbol{P}^a(t)\boldsymbol{F}_c^{aT} + \boldsymbol{Q}_c^a \quad \text{(Eq. 2-117)}$$

The stationary solutions can then be defined by setting the first derivative to zero:

$$\boldsymbol{F}_c^a \hat{\boldsymbol{z}}_\infty^a = \boldsymbol{0} \quad \text{(Eq. 2-118)}$$

$$\boldsymbol{F}_c^a \boldsymbol{P}_\infty^a + \boldsymbol{P}_\infty^a \boldsymbol{F}_c^{aT} + \boldsymbol{Q}_c^a = \boldsymbol{0} \quad \text{(Eq. 2-119)}$$

From which is easy to conclude that the stationary expected value is zero $\hat{\boldsymbol{z}}_\infty^a = \boldsymbol{0}$, and the stationary covariance $\boldsymbol{P}_\infty^a$ can be found numerically by solving the continuous-time Lyapunov equation.

The prior is then defined as $p\left(\boldsymbol{z}^a(t)\right) = \mathcal{N}(\boldsymbol{0}, \boldsymbol{P}_\infty^a)$. It is highlighted that this is a prior for the augmented state. The augmented state has information regarding the response of the system and the load. Therefore, defining a prior for the load defines a prior for the response.

To further illustrate this last point, note that any response of the system can be described from the augmented state by means of a selection matrix. For example, the strain can be described using the selection matrix defined in 2.1.3.1:

$$\varepsilon(t) = \boldsymbol{S}_{\varepsilon m}\boldsymbol{u}_m(t) = [\boldsymbol{S}_{\varepsilon m} \quad \boldsymbol{0} \quad \boldsymbol{0}] \begin{bmatrix} \boldsymbol{u}_m(t) \\ \dot{\boldsymbol{u}}_m(t) \\ \boldsymbol{z}(t) \end{bmatrix} = \boldsymbol{H}_{\varepsilon m}\boldsymbol{z}^a(t) \quad \text{(Eq. 2-120)}$$

The response description depends on the stochastic variable $\boldsymbol{z}^a(t)$. Therefore, it is a stochastic description of the response. As such, the statistics may be computed. In particular, the marginal distribution, or prior, may be computed. This is illustrated by using the strain:

$$\hat{\varepsilon}(t) = \mathbb{E}[\varepsilon(t)] = \mathbb{E}[\boldsymbol{H}_{\varepsilon m}\boldsymbol{z}^a(t)] = \boldsymbol{H}_{\varepsilon m}\mathbb{E}[\boldsymbol{z}^a(t)] = \boldsymbol{H}_{\varepsilon m}\hat{\boldsymbol{z}}_\infty^a = 0 \quad \text{(Eq. 2-121)}$$

$$P_{\varepsilon,\infty} = \mathbb{E}[\varepsilon(t)\varepsilon(t)^T] = \mathbb{E}[\boldsymbol{H}_{\varepsilon m}\boldsymbol{z}^a(t)\boldsymbol{z}^a(t)^T\boldsymbol{H}_{\varepsilon m}^T] = \boldsymbol{H}_{\varepsilon m}\boldsymbol{P}_\infty^a\boldsymbol{H}_{\varepsilon m}^T \quad \text{(Eq. 2-122)}$$

In consequence, the prior of the strain is obtained: $p\left(\varepsilon(t)\right) = \mathcal{N}\left(0, P_{\varepsilon,\infty}\right)$.

Note that it can be easily observed that, in general, all responses of the mechanical system loaded by a zero-mean stationary process will also be zero mean and stationary.

2.4.4.3 Posterior: Kalman Filter and Smoother

The approach is completely analogous to what is presented in Section 2.4.3.3. First the discrete version of the stochastic model is presented, and the observation equation that will provide the information of the system. Subsequently, the prior can be computed recursively by using the Kalman Filter and Smoothing equations.

The expressions found for the statistics can be solved, as these are ordinary differential equations. The solution can be expressed as:

$$\hat{\boldsymbol{z}}^a(t) = \boldsymbol{e}^{\boldsymbol{F}_c(t-t_0)}\hat{\boldsymbol{z}}^a(t_0) \quad \text{(Eq. 2-123)}$$

$$\boldsymbol{P}^a(t) = \boldsymbol{e}^{\boldsymbol{F}_c^a(t-t_0)}\boldsymbol{P}^a(t_0)\boldsymbol{e}^{\boldsymbol{F}_c^a(t-t_0)^T} + \int_{t_0}^{t} \boldsymbol{e}^{\boldsymbol{F}_c^a(t-\tau)}\boldsymbol{Q}_c^a\boldsymbol{e}^{\boldsymbol{F}_c^a(t-\tau)^T}d\tau \quad \text{(Eq. 2-124)}$$

Using discrete notation, and evaluating between time steps:

$$\hat{\boldsymbol{z}}_{[k+1]}^a = \boldsymbol{F}^a\hat{\boldsymbol{z}}_{[k]}^a \quad \text{(Eq. 2-125)}$$

$$\boldsymbol{P}_{[k+1]}^a = \boldsymbol{F}^a\boldsymbol{P}_{[k]}^a\boldsymbol{F}^{aT} + \boldsymbol{Q}_d^a \quad \text{(Eq. 2-126)}$$

With:

$$\boldsymbol{F}^a = \boldsymbol{e}^{\boldsymbol{F}_c^a\Delta t} \quad \text{(Eq. 2-127)}$$

$$\boldsymbol{Q_d^a} = \int_{k\Delta t}^{(k+1)\Delta t} \boldsymbol{e^{F_c^a((k+1)\Delta t-\tau)} Q_c^a e^{F_c^a((k+1)\Delta t-\tau)^T}} d\tau \quad \text{(Eq. 2-128)}$$

The expressions obtained for the statistics define an equivalent discrete version of the system:

$$\boldsymbol{z_{[k+1]}^a} = \boldsymbol{F^a z_{[k]}^a} + \boldsymbol{w_{[k]}^a} \quad \text{(Eq. 2-129)}$$

With $\boldsymbol{w_{[k]}^a} \sim \mathcal{N}(0, \boldsymbol{Q_d^a})$.

To compute the posterior, an observation equation needs to be defined. Note that only part of the augmented state is observed (accelerations). Starting from the observation equation defined in 2.1.2.2

$$\boldsymbol{y}(t) = \boldsymbol{G_{cm} x_m}(t) + \boldsymbol{J_{cm} p}(t) \quad \text{(Eq. 2-130)}$$

Using the state space representation of the load, this can be written in terms of the augmented state:

$$\boldsymbol{y}(t) = \boldsymbol{H_c^a z^a}(t) \quad \text{(Eq. 2-131)}$$

With:

$$\boldsymbol{H_c^a} = [\boldsymbol{G_{cm}} \quad \boldsymbol{J_{cm} H_c}\,] \quad \text{(Eq. 2-132)}$$

Furthermore, noticing that the observations are measured at discrete points in time, and that they are not perfect, the following discrete form of the observation is employed:

$$\boldsymbol{y_{[k]}} = \boldsymbol{H_c^a z_{[k]}^a} + \boldsymbol{r_{[k]}} \quad \text{(Eq. 2-133)}$$

With $\boldsymbol{r_{[k]}}$ a stochastic variable representing the error of the measurement. This is assumed to be a white gaussian noise: $\boldsymbol{r_{[k]}} \sim \mathcal{N}(0, \boldsymbol{R})$. With $\boldsymbol{R} \in \mathbb{R}^{n_y \times n_y}$ a diagonal matrix with the variances for each signal noise in its diagonals: σ_{Ri}^2.

As discussed in 2.4.3.3, the posterior can be computed by using the Kalman Filter and Smoother using the discrete form of the augmented model and the discrete form including noise of the observation equation. The Kalman Filter and Smoother expressions are shown below for the augmented version. Note that the initial values has to be the stationary solutions in order to properly compute the posterior.

Table 2-2. Kalman filter and smoother equations. Augmented model.

Time Update:	Measurement Update:	Smoothing:
$p(\boldsymbol{z_{[k]}^a}\|\boldsymbol{y}_{[1:k-1]}) = \mathcal{N}(\hat{\boldsymbol{z}}_{[k]}^{a-}, \boldsymbol{P}_{[k]}^{a-})$	$p(\boldsymbol{z_{[k]}^a}\|\boldsymbol{y}_{[1:k]}) = \mathcal{N}(\hat{\boldsymbol{z}}_{[k]}^{a+}, \boldsymbol{P}_{[k]}^{a+})$ $p(\boldsymbol{y}_{[1:k]}\|\boldsymbol{y}_{[1:k-1]}) = \mathcal{N}(\boldsymbol{H_c^a}\hat{\boldsymbol{z}}_{[k]}^{a-}, \boldsymbol{S}_{[k]})$	$p(\boldsymbol{z_{[k]}^a}\|\boldsymbol{y}_{[1:N]}) = \mathcal{N}(\hat{\boldsymbol{z}}_{[k]}^{a}, \boldsymbol{P}_{[k]}^{a})$
$\hat{\boldsymbol{z}}_{[k]}^{a-} = \boldsymbol{F^a}\hat{\boldsymbol{z}}_{[k-1]}^{a+}$ $\boldsymbol{P}_{[k]}^{a-} = \boldsymbol{F^a P}_{[k-1]}^{a+}\boldsymbol{F}^{aT} + \boldsymbol{Q_d^a}$	$\boldsymbol{r}_{[k]} = \boldsymbol{y}_{[k]} - \boldsymbol{H_c^a}\hat{\boldsymbol{z}}_{[k]}^{a-}$ $\boldsymbol{S}_{[k]} = \boldsymbol{H_c^a P}_{[k]}^{a-}\boldsymbol{H_c}^{aT} + \boldsymbol{R}$ $\boldsymbol{K}_{[k]} = \boldsymbol{P}_{[k]}^{a-}\boldsymbol{H_c^a}(\boldsymbol{S}_{[k]})^{-1}$ $\hat{\boldsymbol{z}}_{[k]}^{a+} = \hat{\boldsymbol{z}}_{[k]}^{a-} + \boldsymbol{K}_{[k]}\boldsymbol{r}_{[k]}$ $\boldsymbol{P}_{[k]}^{a+} = \boldsymbol{P}_{[k]}^{a-} - \boldsymbol{K}_{[k]}\boldsymbol{S}_{[k]}\boldsymbol{K}_{[k]}^T$	$\boldsymbol{C}_{[k]} = \boldsymbol{P}_{[k]}^{a+}\boldsymbol{F}^{aT}(\boldsymbol{P}_{[k+1]}^{a-})^{-1}$ $\hat{\boldsymbol{z}}_{[k]}^{a} = \hat{\boldsymbol{z}}_{[k]}^{a+} + \boldsymbol{C}_{[k]}(\hat{\boldsymbol{z}}_{[k+1]}^{a} - \hat{\boldsymbol{z}}_{[k+1]}^{a-})$ $\boldsymbol{P}_{[k]}^{a} = \boldsymbol{P}_{[k]}^{a+} + \boldsymbol{C}_{[k]}(\boldsymbol{P}_{[k+1]}^{a} - \boldsymbol{P}_{[k+1]}^{a-})\boldsymbol{C}_{[k]}^T$

The description of this process is analogous to what was presented in 2.4.3.3. It is recalled that the result from the smoothing step is the posterior, written in discrete notation: $p(\boldsymbol{z_{[k]}^a}|\boldsymbol{y}_{[1:N]}) = \mathcal{N}(\hat{\boldsymbol{z}}_{[k]}^{a}, \boldsymbol{P}_{[k]}^{a})$. Note that the main difference with respect to what is described in 2.4.3.3 is that the posterior is computed only on partial information of the system. This means that the prior belief of the response of the system (e.g., strains) can be updated by any information of the system (e.g., accelerations).

It is highlighted that defining the discrete version of the noise covariance $\boldsymbol{Q}_{\boldsymbol{d}}^{a}$ through the integral is difficult and unpractical. An alternative method of computing is by using the solution for the covariance in discrete version:

$$\boldsymbol{P}_{[k+1]}^{a} = \boldsymbol{F}^{a}\boldsymbol{P}_{[k]}^{a}\boldsymbol{F}^{aT} + \boldsymbol{Q}_{\boldsymbol{d}}^{a} \quad \text{(Eq. 2-134)}$$

Noticing that the stationary solution also applies for this expression:

$$\boldsymbol{P}_{\infty}^{a} = \boldsymbol{F}^{a}\boldsymbol{P}_{\infty}^{a}\boldsymbol{F}^{aT} + \boldsymbol{Q}_{\boldsymbol{d}}^{a} \quad \text{(Eq. 2-135)}$$

And further noticing that the stationary covariance has been already computed by the prior (see 2.4.4.2), a more practical way to define the noise covariance is obtained:

$$\boldsymbol{Q}_{\boldsymbol{d}}^{a} = \boldsymbol{F}^{a}\boldsymbol{P}_{\infty}^{a}\boldsymbol{F}^{aT} - \boldsymbol{P}_{\infty}^{a} \quad \text{(Eq. 2-136)}$$

2.4.5 Parameter Estimation

So far it has been assumed that the hyperparameters σ, l_{sc} of the Matern32 covariance function that represents the load are defined. However, given that the load is unknown, so is the covariance function that could define it stochastically. Furthermore, the noise levels defined through $\boldsymbol{R}$ for the measurements are also unknown.

This section provides two frameworks to estimate these unknown parameters. The first one will be referred to as Maximum A Posteriori, and it is the method suggested by [18], [19], [40]. The second method, referred as 'Fitting the Prior and Posterior', is a novel methodology that aims to solve the parameter estimation in a more intuitive and efficient manner.

2.4.5.1 Maximum A Posteriori

Let the unknown parameters be defined as the hyperparameters $\boldsymbol{\theta} = \{\sigma^2, l_{sc}, \boldsymbol{R}\}$.

The Bayesian way of treating these unknown hyperparameters is by looking at the posterior distribution [41]:

$$p\left(\boldsymbol{z}_{[1:N]}^{a}, \boldsymbol{\theta} \middle| y_{[1:N]}\right) \quad \text{(Eq. 2-137)}$$

Only the marginal posterior distribution of the hyperparameters is of interest. This is given by [41]:

$$p\left(\boldsymbol{\theta} \middle| y_{[1:N]}\right) = \int p\left(\boldsymbol{z}_{[1:N]}^{a}, \boldsymbol{\theta} \middle| y_{[1:N]}\right) d\boldsymbol{z}_{[1:N]}^{a} \quad \text{(Eq. 2-138)}$$

In words, this is the conditional distribution of the hyperparameters given some set of observations. The distribution will vary depending on the hyperparameters chosen. Higher values would be obtained if the hyperparameters chosen yield a higher likelihood for this posterior distribution. This in turn means, at least in a probabilistic sense, that the hyperparameters yield a good representation of the stochastic process. The objective therefore is to find the hyperparameters that maximize this conditional distribution:

$$\widehat{\boldsymbol{\theta}} = \max_{\boldsymbol{\theta}} p\left(\boldsymbol{\theta} \middle| y_{[1:N]}\right) \quad \text{(Eq. 2-139)}$$

This is known as a Maximum A Posteriori estimate [41]. As mentioned in the same reference, computing the full posterior distribution is computationally very expensive. An alternative definition using bayes rule is considered:

$$p\left(\boldsymbol{\theta} \middle| y_{[1:N]}\right) = \frac{p\left(y_{[1:N]} \middle| \boldsymbol{\theta}\right) p(\boldsymbol{\theta})}{p\left(y_{[1:N]}\right)} \propto p\left(y_{[1:N]} \middle| \boldsymbol{\theta}\right) p(\boldsymbol{\theta}) \quad \text{(Eq. 2-140)}$$

Therefore, the Maximum A Posteriori estimate can be obtained maximizing this function:

$$\widehat{\boldsymbol{\theta}} = \max_{\boldsymbol{\theta}} \left(p\left(y_{[1:N]} \middle| \boldsymbol{\theta}\right) p(\boldsymbol{\theta}) \right) \quad \text{(Eq. 2-141)}$$

In order to efficiently compute this distribution (and therefore maximize it to obtain the estimates), the following function is used:

$$\varphi_{[N]}(\boldsymbol{\theta}) = -\log\left(p\left(y_{[1:N]}|\boldsymbol{\theta}\right)\right) - \log\left(p(\boldsymbol{\theta})\right) \quad \text{(Eq. 2-142)}$$

This is called the energy function. Then, it is easy to observe that minimizing this function would yield the Maximum A Posteriori estimates:

$$\widehat{\boldsymbol{\theta}} = \min_{\boldsymbol{\theta}}\left(\varphi_{[N]}(\boldsymbol{\theta})\right) \quad \text{(Eq. 2-143)}$$

The advantage of using this definition, is that the energy function can be computed iteratively directly from the Measurement Update step of the Kalman Filter. This has been shown in [41]:

$$\varphi_{[k]}(\boldsymbol{\theta}) = \varphi_{[k-1]}(\boldsymbol{\theta}) + \frac{1}{2}\log\left(2\pi\, det\left(\boldsymbol{S}_{[k]}\right)\right) + \frac{1}{2}\boldsymbol{r}_{[k]}{}^{T}\boldsymbol{S}_{[k]}{}^{-1}\boldsymbol{r}_{[k]} \quad \text{(Eq. 2-144)}$$

Which shows how the energy function is computed from the Kalman Filter (see Table 2-2). Note that the smoothing step is not required to compute it.

Note that the initial step $\varphi_{[0]}(\boldsymbol{\theta})$ is defined by:

$$\varphi_{[0]}(\boldsymbol{\theta}) = -\log\left(p(\boldsymbol{\theta})\right) \quad \text{(Eq. 2-145)}$$

In words, this means that the starting value for the energy function is the negative log-likelihood of the hyperparameters. This is directly related to the prior of the hyperparameters. If no prior knowledge is available, the distribution may be assumed to be uniform over all possible values of $\boldsymbol{\theta}$, which in practice can be implemented by starting with $\varphi_{[0]}(\boldsymbol{\theta}) = 0$.

2.4.5.1.1 Remarks

The Maximum A Posteriori method presented here has two drawbacks. First, given the large number of undefined parameters (five in total, considering three accelerometers), it is difficult to have a representation of the behaviour of the energy function. Second, as discussed in [18], attempting to minimise this function through optimisation may yield a local minima instead of a global minima. Taking into account both drawbacks, this method can be characterised as being unintuitive and unpractical given the difficulty in the optimisation process. This motivates the need to develop an alternative method for parameter estimation.

2.4.5.2 Fitting the Prior and Posterior

This method aims to define the Matern32 hyperparameters and the noise levels separately. The Matern32 hyperparameters σ, l_{sc} will be defined by ensuring that the prior belief obtained for the measured accelerations fit well with the observations. Whereas the noise levels $\boldsymbol{R}$ will be defined by ensuring that the error estimated from the posterior $\widehat{\boldsymbol{R}}$ fits well with the error defined for the computation of the posterior $\boldsymbol{R}$.

2.4.5.2.1 Fitting the prior

The prior of the accelerations can be easily computed from the prior of the augmented state through the observation equation defined in Section 2.4.4.2:

$$\boldsymbol{y}(t) = \boldsymbol{H}_c^{\boldsymbol{a}}\boldsymbol{z}^{\boldsymbol{a}}(t) \quad \text{(Eq. 2-146)}$$

$$\widehat{\boldsymbol{y}}_{\infty} = \boldsymbol{H}_c^{a}\boldsymbol{z}_{\infty}^{a} = \boldsymbol{0} \quad \text{(Eq. 2-147)}$$

$$\boldsymbol{P}_{y,\infty} = \mathbb{E}[\boldsymbol{y}(t)\boldsymbol{y}(t)^{T}] = \boldsymbol{H}_c^{a}\boldsymbol{P}_{\infty}^{a}\boldsymbol{H}_c^{aT} \quad \text{(Eq. 2-148)}$$

In words: the expected value of the accelerations is zero, and the covariance is given by $\boldsymbol{P}_{y,\infty}$. In particular, the variance for each channel (accelerometer) σ_y^2 will be defined by the diagonal elements

of this covariance matrix. It is highlighted that the correlation between the observed points is defined through the elements outside the diagonal.

Note that this is the prior of the accelerations. This is part of the augmented model. No information of the measurements has been used other than their location within the mechanical model.

Now, taking into consideration that there are measurements available, it is possible to estimate the variance of the observations by directly computing it from the records. This will yield a variance for each channel: σ^{*2}_y.

The key of this method is to realise that the prior belief of the augmented model can be educated through the observations. This can be realised by matching the variance obtained from the model (prior) with the variance that can be computed from the measurements: $\sigma^2_y \approx \sigma^{*2}_y$. In other words: the prior belief should fit the data available.

It is important to realise that an exact match may not be possible. This may be due to the mechanical model not being sufficiently representative of the structure, or due to an inaccurate estimation of the variance from the records, amongst other reasons.

This observation motivates the fit of the prior as a maximum likelihood estimation.

For each signal, a log-normal distribution is built with the mode (peak of the distribution) being defined by the computed variance σ^{*2}_y. The spread of the distribution is defined arbitrarily by the 95[%] interval of confidence. The lower bound is defined by approximately half this value, and the higher bound is defined by approximately double this value. The exact computation of the distribution is illustrated in Figure 2-8. Note that it uses commonly known properties of the log-normal distribution: μ_{mode} referring to the mode (which is the peak of the distribution), and $\mu_{med.}$ referring to the median, from which the interval of confidence bounds can be defined.

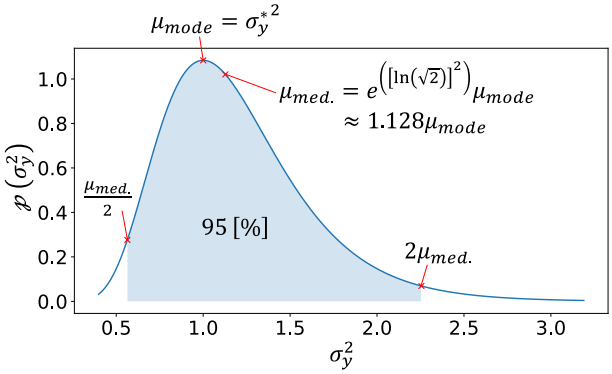

Figure 2-8. Log-normal distribution definition.

For each signal, the best prior would be the one that maximises the associated log-normal distribution.

Given that the goal is to fit the prior to all the observations, what is sought is to maximise all the log-normal distributions associated to all the channels. An efficient way to do so is by using the joint distribution. The joint distribution can be computed by assuming that the distributions are independent, which means that the joint distribution is just the multiplication of the distributions. The assumption of independence follows from the independent definition of the distribution on each signal.

Therefore, the σ and l_{sc} hyperparameters are estimated by maximising the likelihood of this joint distribution. This will ensure that the prior belief is a good match for the observations.

2.4.5.2.2 Fitting the posterior

Now that the prior for the load is defined, the noise levels for each signal, contained in $\boldsymbol{R}$, are required to be defined. This will be realised by studying the posterior of the measured accelerations.

The acceleration measurements are related to the model through the observation equation which includes noise:

$$\boldsymbol{y}_{[k]} = \boldsymbol{H}_{\boldsymbol{c}}^{\boldsymbol{a}} \boldsymbol{z}_{[k]}^{a} + \boldsymbol{r}_{[k]} \qquad \text{(Eq. 2-149)}$$

An estimation for the noise process can therefore be obtained by using the expected value for the augmented state, obtained from the posterior:

$$\hat{\boldsymbol{r}}_{[k]} = \boldsymbol{y}_{[k]} - \boldsymbol{H}_{\boldsymbol{c}}^{\boldsymbol{a}} \hat{\boldsymbol{z}}_{[k]}^{a} \qquad \text{(Eq. 2-150)}$$

Note that the measurements $\boldsymbol{y}_{[k]}$ are deterministic, as the values are directly obtained from the accelerometers.

An estimation of the variance of the noise can be obtained by the associated noise estimations. Therefore, an estimation of the noise matrix is obtained:

$$\widehat{\boldsymbol{R}} = \mathrm{var}\left(\hat{\boldsymbol{r}}_{[k]}\right) \qquad \text{(Eq. 2-151)}$$

The key aspect in this method is to acknowledge that the posterior provides an estimation of the noise covariance. Fitting the posterior translates therefore into matching the defined noise level $\boldsymbol{R}$ with the estimated noise level $\widehat{\boldsymbol{R}}$.

The methodology employed to do so is iterative, illustrated in Figure 2-9, and described as follows:

1) An arbitrary amount of noise is defined for the signals. A starting point may be taken equal to the variance of the signal $\boldsymbol{R} = \mathrm{var}\left(\boldsymbol{y}_{[k]}\right)$. Note that, unless the signal is purely noise, the real amount of noise should be lower.
2) The posterior is computed, from which an estimation for the noise is obtained: $\widehat{\boldsymbol{R}}$
3) The noise is defined as the estimated noise $\boldsymbol{R} = \widehat{\boldsymbol{R}}$
4) Steps two and three are repeated until the maximum relative difference between the variances is less than a user-defined tolerance: $\max\left(\mathrm{diag}\left\{\frac{|\widehat{\boldsymbol{R}}-\boldsymbol{R}|}{\boldsymbol{R}}\right\}\right) < \mathrm{tol}$

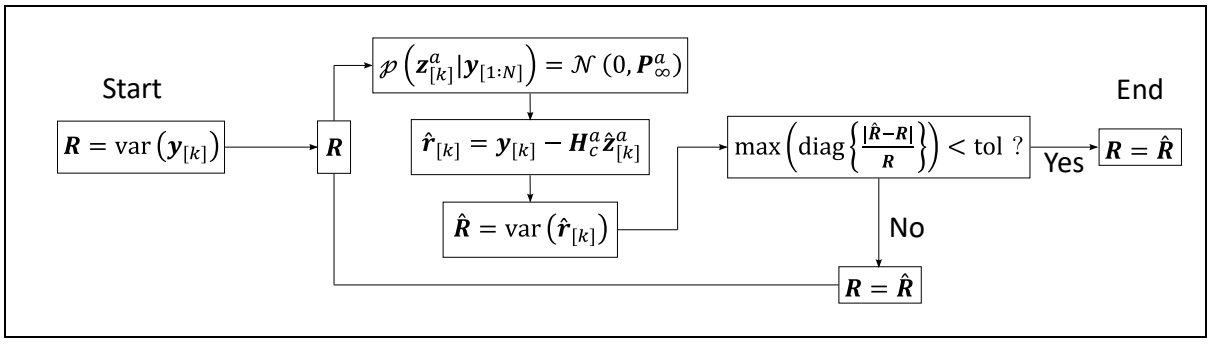

Figure 2-9. Fitting the posterior. Iterative process.

2.5 Error Metrics

The numerical assessment is performed by three measures of accuracy. Namely, the Mean Absolute Error (MAE), Time Response Assurance Criterion ($TRAC$), and the relative error. The MAE and $TRAC$ are defined below using a reference signal $\boldsymbol{x}$ and associated estimation $\hat{\boldsymbol{x}}$:

$$MAE(\boldsymbol{x}, \hat{\boldsymbol{x}}) = \frac{1}{N}\sum_{k}\left|\hat{x}_{[k]} - x_{[k]}\right| \quad \text{(Eq. 2-152)}$$

$$TRAC(\boldsymbol{x}, \hat{\boldsymbol{x}}) = \frac{(\hat{\boldsymbol{x}}\boldsymbol{x}^T)^2}{(\hat{\boldsymbol{x}}\hat{\boldsymbol{x}}^T)(\boldsymbol{x}\boldsymbol{x}^T)} \quad \text{(Eq. 2-153)}$$

The MAE will yield the error on average of the estimated time signal, and the $TRAC$ yields a measure of correlation of the time signals. A $TRAC$ value closer to one indicates strong correlation, and a value closer to zero indicates no correlation.

The relative error will be used as a measure of accuracy for parameter estimations. Considering an estimation $\hat{x}$ and a reference value x, the relative error of the variable is defined as:

$$e_x = \frac{\hat{x} - x}{x} \quad \text{(Eq. 2-154)}$$

3 Simulation

3.1 Mechanical Model

The simulation is defined as a mechanical model of the wind turbine through a finite element model. The aim of this simulation is to provide a known system from which the system identification and response estimation can be illustrated and validated. The finite element model is built considering a set of beam elements (see section 2.1.3). The nacelle, rotor and blades are greatly simplified by considering them as an additional mass on top. The foundation is assumed to clamp the tower in the bottom. The geometry of the tower varies in height. To capture this geometry, $n = 100$ uniform beam elements are used. Each element has a different geometry defined from the average diameter and thickness that the element is capturing. Figure 3-1 summarises the properties of the mechanical model considered. The modal properties, loads, observations, and responses are defined in the following subsections.

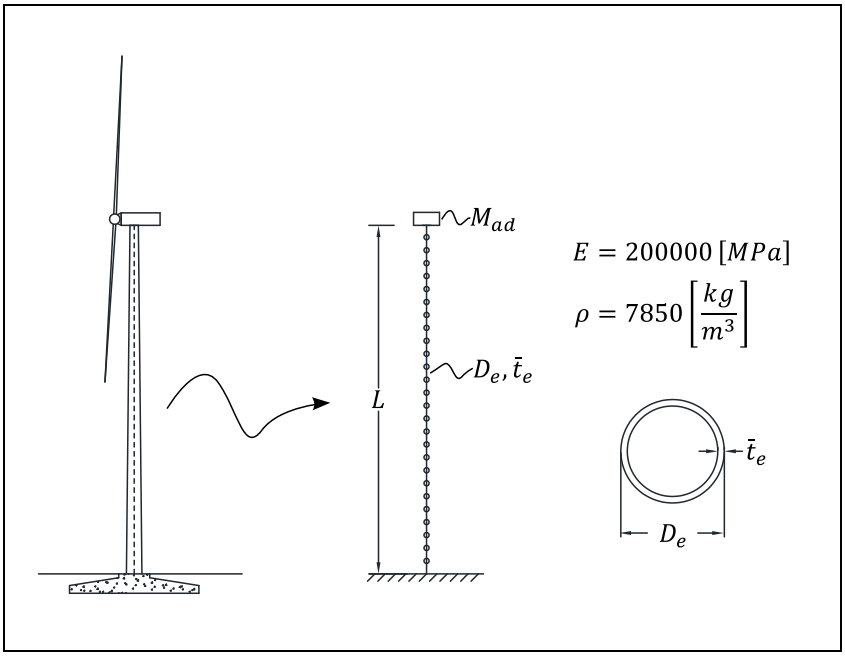

Figure 3-1. Mechanical model assumptions summary. Simulation.

3.1.1 Modal properties

The definition shown above for the mechanical model does not take into account damping. For simplicity, a damping ratio of $\zeta_n = 1[\%]$ is considered for all modes. The damping matrix for the system is then defined as:

$$\boldsymbol{C} = \boldsymbol{M}\boldsymbol{\Phi}\boldsymbol{\Gamma}\boldsymbol{\Phi}^{\mathrm{T}}\boldsymbol{M}^{T} \quad \text{(Eq. 3-1)}$$

$$\boldsymbol{\Gamma} = \mathrm{diag}(2\zeta_n\omega_n) \quad \text{(Eq. 3-2)}$$

The first three mode shapes and frequencies are shown in Figure 3-2.

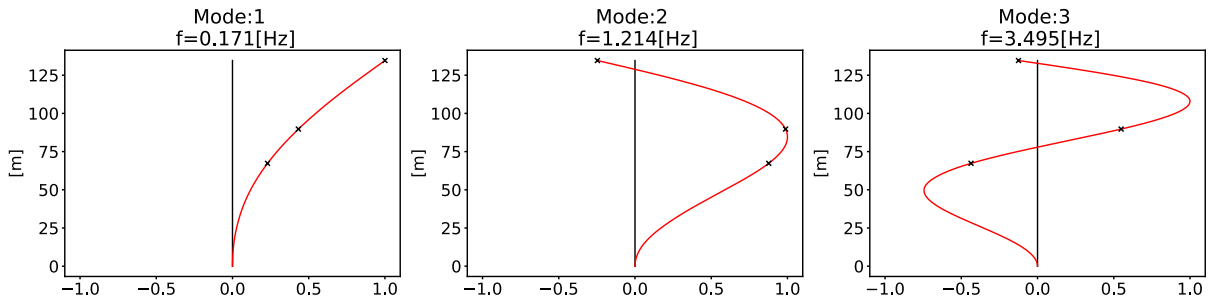

Figure 3-2. Simulation first three modes. Mode shapes and frequencies. Damping ratio: $\zeta = 1\%$ for all modes. Sensor locations are marked with 'x'.

3.1.2 Load and response

A stochastic load is applied on top of the tower and the response is measured at three points: 1/2 of the height, 2/3 of the height and at the top. The aim for the response estimation will be to estimate the strain at the bottom. The set-up is illustrated in Figure 3-3.

The simulation is run for 700[s] sampling at 1000[Hz]. The response is obtained using Newmark β-method, in particular the average acceleration variant, as it is unconditionally stable [26]. The first 100[s] are discarded to avoid transient effects from the start of the simulation. Consequently, the simulation covers 10[mins.] worth of data.

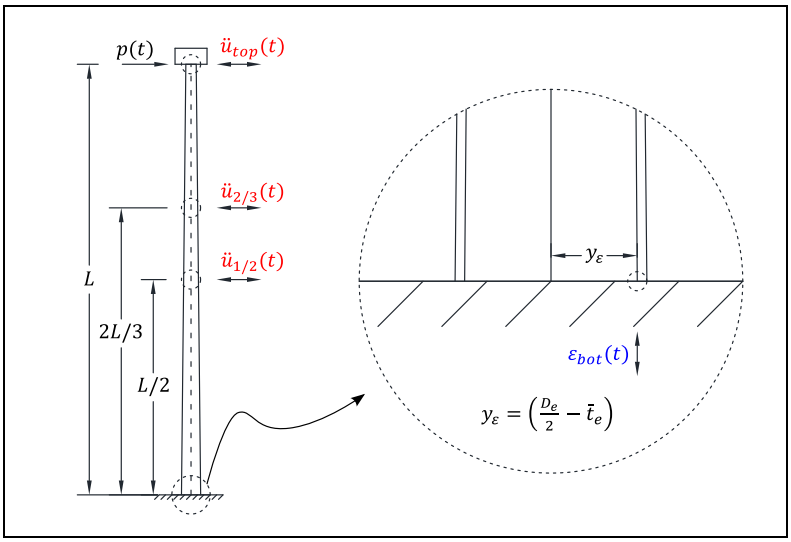

Figure 3-3. Simulation measurement and response set-up.

The stochastic load is defined by a realisation of a zero mean gaussian process with a Matern32 covariance function with a length scale of $l_{sc} = 0.5[s]$ and a magnitude of $\sigma = 10[kN]$. The load is shown in the time and frequency domain in Figure 3-4. The acceleration response is observed for the three locations as shown in Figure 3-3. Figure 3-5 to Figure 3-7 shows the acceleration response for the three locations. Finally, Figure 3-8 shows the strain response at the bottom.

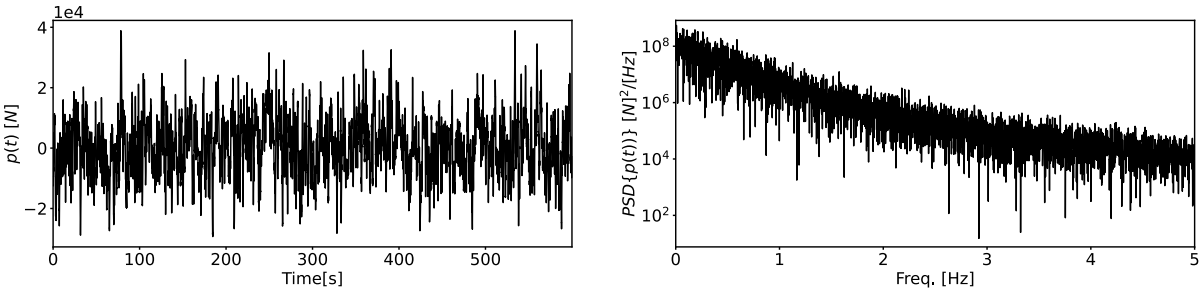

Figure 3-4. Applied load. Time-History (left) and Power Spectral Density (right). Simulation.

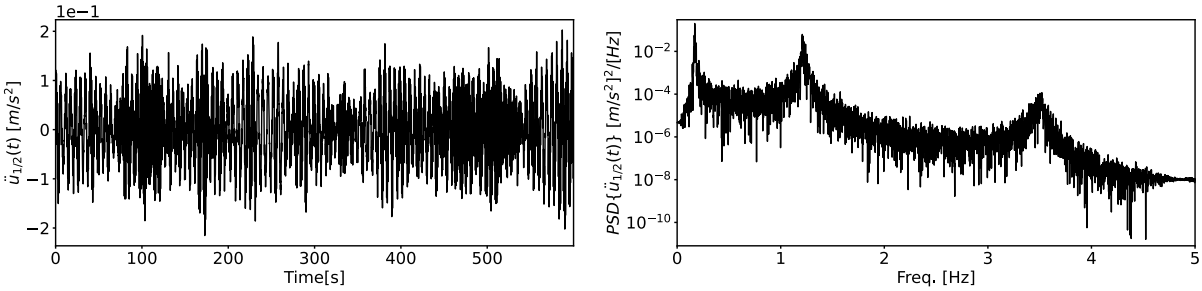

Figure 3-5. Acceleration at L/2. Time-History (left) and Power Spectral Density (right). Simulation.

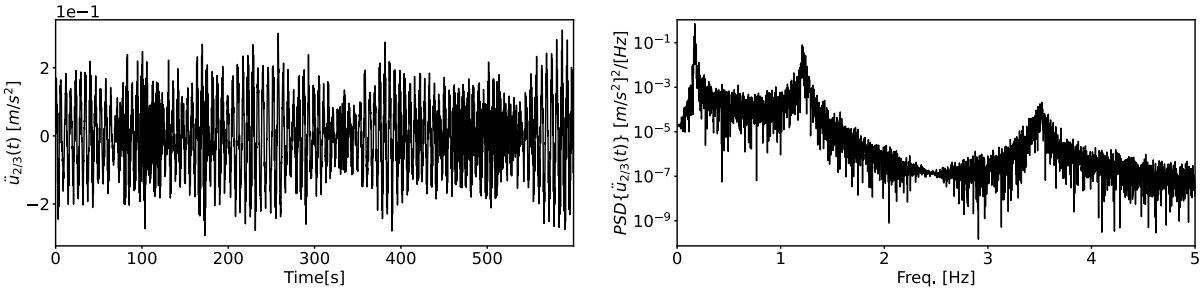

Figure 3-6. Acceleration at 2L/3. Time-History (left) and Power Spectral Density (right). Simulation.

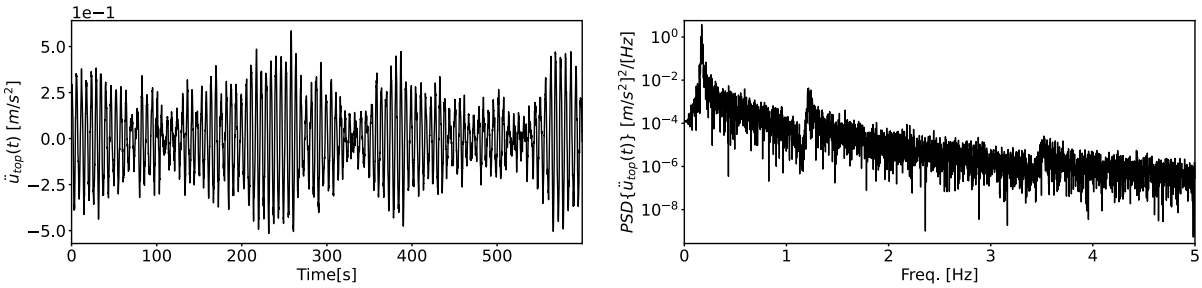

Figure 3-7. Acceleration at the top. Time-History (left) and Power Spectral Density (right). Simulation.

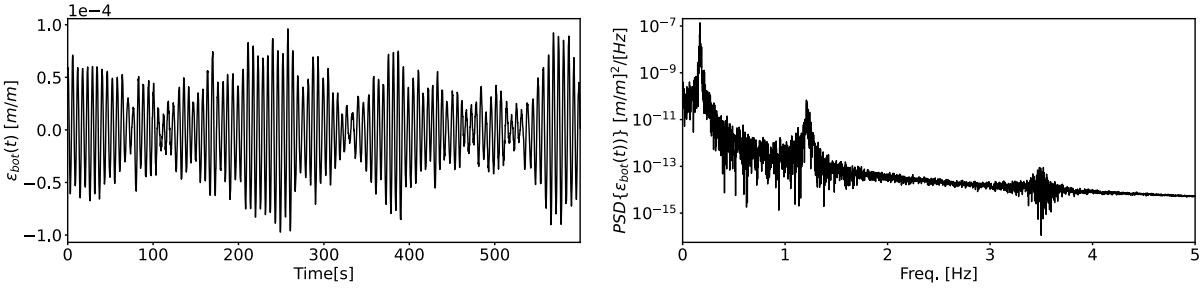

Figure 3-8. Strain at the bottom. Time History (left) and Power Spectral Density (right). Simulation.

3.1.3 Observations

The observations resample the acceleration response at $f_s = 20[Hz]$ and consider an added noise with a signal-to-noise ratio (SNR) of $1:(0.5[\%])$. The noise for each channel is then defined by a zero mean normal distribution with a variance σ_R^2 defined through the variance of the acceleration $\sigma_{\ddot{u}}^2$:

$$SNR = \frac{\sigma_{\ddot{u}}^2}{\sigma_R^2} = \frac{1}{0.5[\%]} \Rightarrow \sigma_R^2 = 0.5[\%]\sigma_{\ddot{u}}^2 \qquad \text{(Eq. 3-3)}$$

In consequence, the noise covariance matrix is defined by:

$$\boldsymbol{R} = \begin{bmatrix} \sigma_R^2(\ddot{u}_{1/2}) & 0 & 0 \\ 0 & \sigma_R^2(\ddot{u}_{2/3}) & 0 \\ 0 & 0 & \sigma_R^2(\ddot{u}_{top}) \end{bmatrix} = \begin{bmatrix} 20.65 & 0 & 0 \\ 0 & 49.85 & 0 \\ 0 & 0 & 196.21 \end{bmatrix} \times 10^{-6} \left[\frac{m}{s^2}\right]^2 \qquad \text{(Eq. 3-4)}$$

Figure 3-9 to Figure 3-11 illustrate the observations. Note that the defined noise level is higher than the amplitude of the response for frequencies higher than 5[Hz].

Note that, as discussed in Section 1.2.3, the quasi-static part cannot be estimated from acceleration measurements. Therefore, when using response estimation methods (sections 3.3 and 3.4), a high-pass Butterworth filter of order 4 with cut-off frequency $f = 0.1[Hz]$ is applied to the simulated measurements (accelerations and strains).

Further noise levels are used for assessing the response estimation methods (section 3.4). The noise levels are defined with $SNR = \{1:(1[\%]), 1:(5[\%]), 1:(10[\%])\}$. The exact noise levels are summarised in Table 3-1.

Table 3-1. Noise variance definition. Simulation.

SNR	$\sigma_R(\ddot{u}_{1/2})\left[\frac{m}{s^2}\right]$	$\sigma_R(\ddot{u}_{2/3})\left[\frac{m}{s^2}\right]$	$\sigma_R(\ddot{u}_{top})\left[\frac{m}{s^2}\right]$
$1:(0.5[\%])$	4.54×10^{-3}	7.06×10^{-3}	14.01×10^{-3}
$1:(1[\%])$	6.43×10^{-3}	9.98×10^{-3}	19.81×10^{-3}
$1:(5[\%])$	14.37×10^{-3}	22.33×10^{-3}	44.30×10^{-3}
$1:(10[\%])$	20.32×10^{-3}	31.57×10^{-3}	62.64×10^{-3}

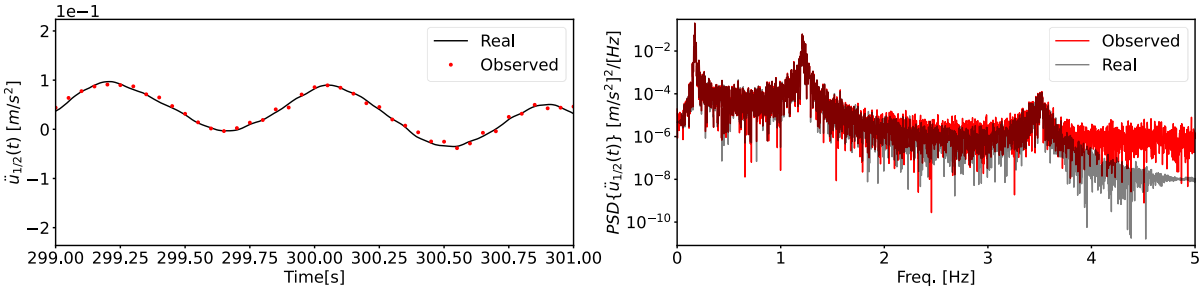

Figure 3-9. Observation at L/2. Time History (left) and Power Spectral Density (right). Simulation.

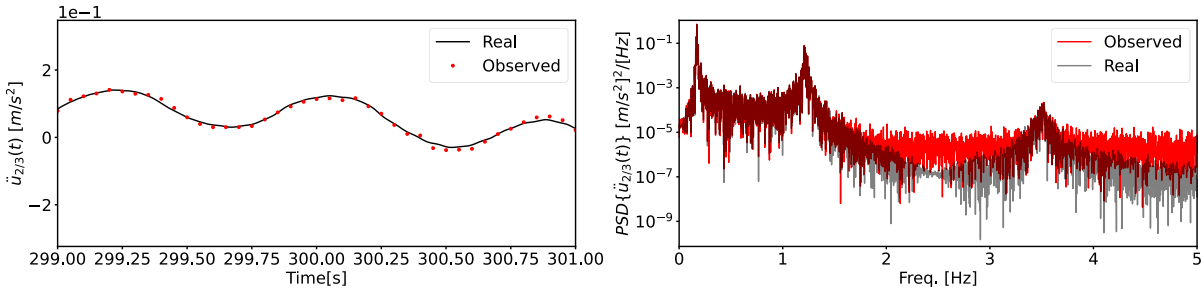

Figure 3-10. Observation at 2L/3. Time History (left) and Power Spectral Density (right). Simulation.

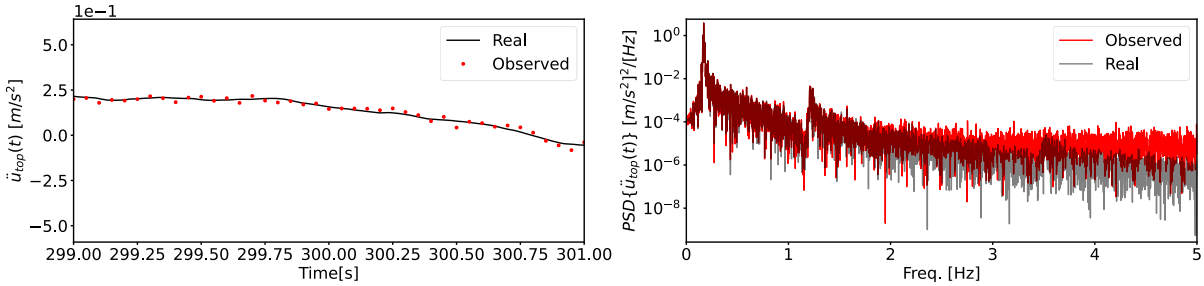

Figure 3-11. Observation at the top. Time History (left) and Power Spectral Density (right). Simulation.

3.2 System Identification

3.2.1 SSI-Cov

The result of implementing SSI-Cov on the simulation is presented through the stabilisation diagram shown in Figure 3-12. Model orders n_o in the range of 10 to 75 were used. From this stabilisation diagram, stable columns can be observed close to the first three natural frequencies of the structure: 0.17[Hz], 1.21[Hz], 3.50[Hz]. These stable columns are sought to be detected through cluster analysis.

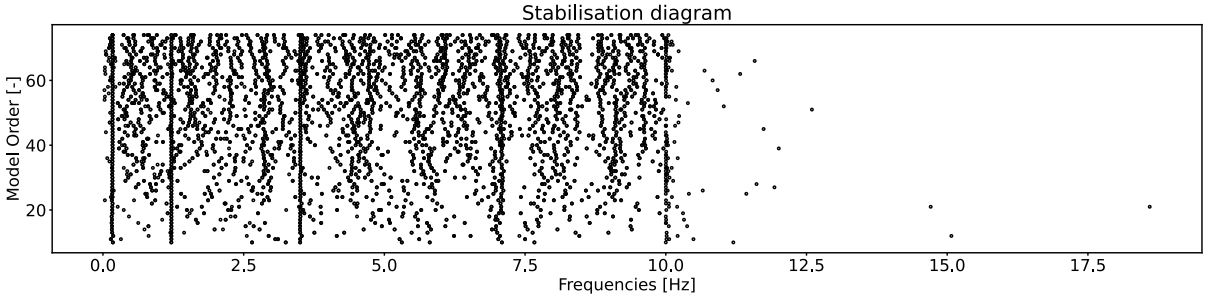

Figure 3-12. Stabilisation Diagram. Simulation.

3.2.2 First Stage: Clearing the stabilisation diagram

The stabilisation diagram is cleared considering a maximum frequency of $f_{max} = 5[Hz]$ and a maximum damping ratio of $\zeta_{max} = 20[\%]$. The result is shown in Figure 3-13 along with the frequency content of the three sensors. From this cleared stabilisation diagram, the stable columns are easier to identify.

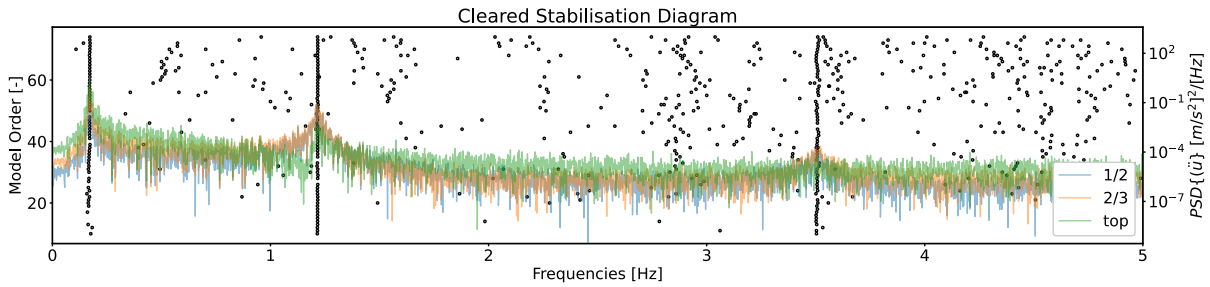

Figure 3-13. Cleared Stabilisation diagram. Simulation.

3.2.3 Second Stage: Optics

In consistency with section 2.2.3.2.5, the $MinObj$ parameter is defined by imposing that the stable columns should cover at least half of the diagram. Therefore: $\alpha_{MinObj} = 0.5 \rightarrow MinObj = 32$. The construction of the reachability plot is shown in Figure 3-14. The subsequent definition of the steep objects is shown in Figure 3-15. The clusters are then defined from the set of objects between a downwards and an upwards steep object, as shown in Figure 3-16. The resulting clusters are shown in the stabilisation diagram in Figure 3-17. Note that these clusters accurately cover the expected stable columns.

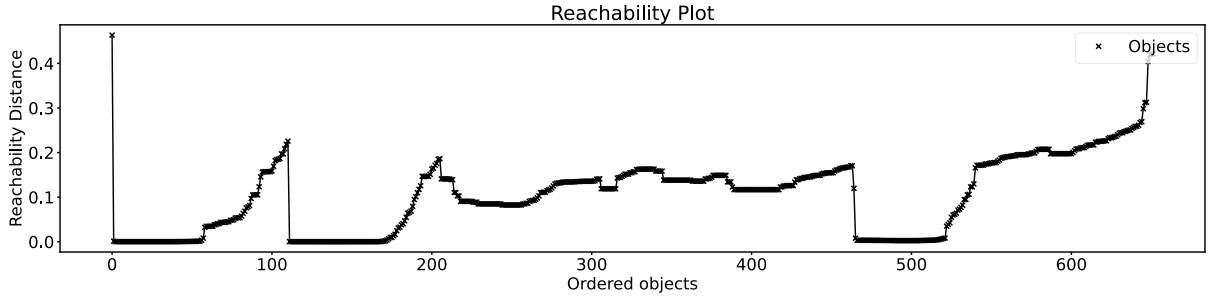

Figure 3-14. Reachability Plot. Simulation.

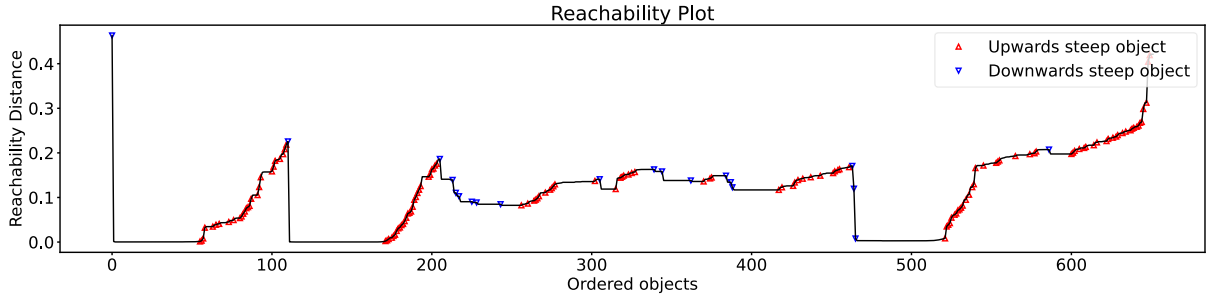

Figure 3-15. Reachability Plot, steep objects. Simulation.

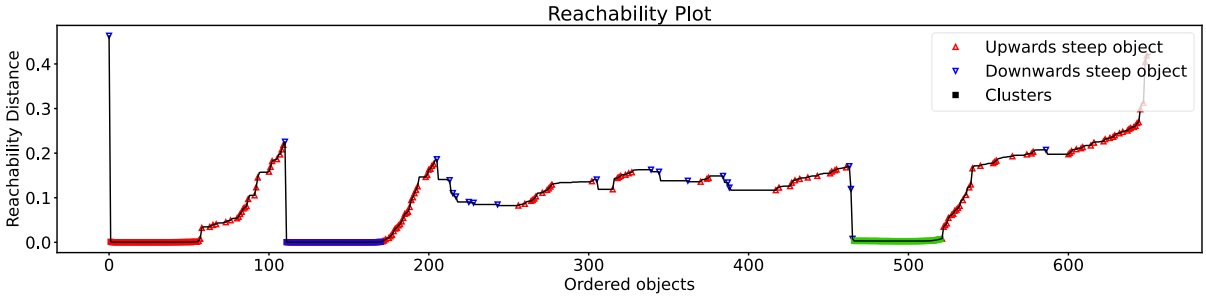

Figure 3-16. Reachability Plot, clusters. Simulation.

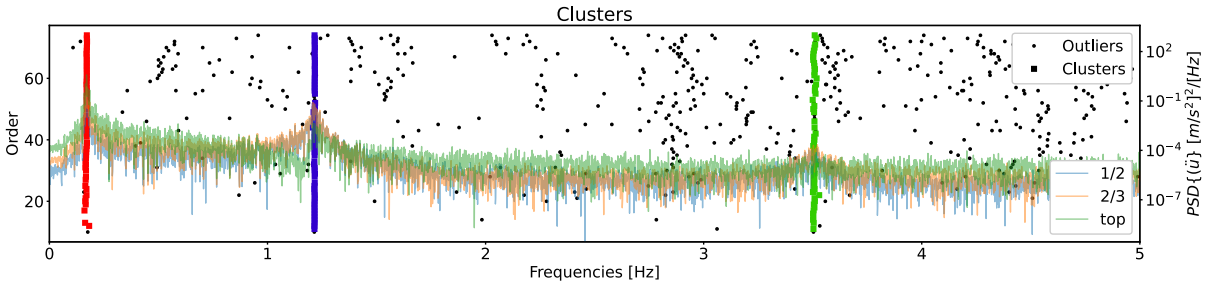

Figure 3-17. Stabilisation Diagram, clusters. Simulation.

3.2.4 Third Stage: Representative element

The representative element is defined by the median value. The results are shown in Figure 3-18 for the frequencies and damping ratios identified, and Figure 3-19 for the mode shapes. Note that the mode shape amplitude and associated phase are normalised to the range [-1,1]. A summary is presented in Table 3-2, where the error between the identified properties and the real properties is presented.

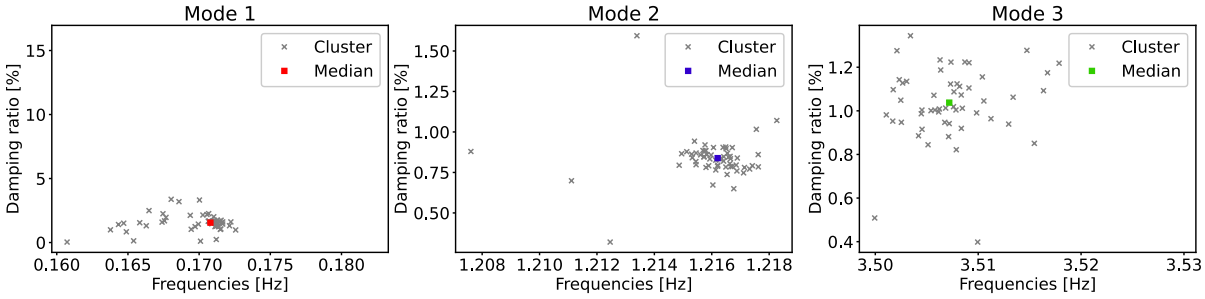

Figure 3-18. Representative elements: Frequencies and damping ratios. Simulation.

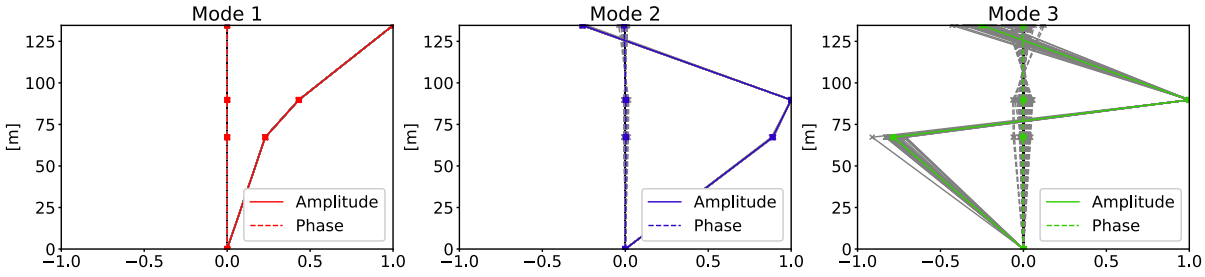

Figure 3-19. Representative elements: Mode shape. Simulation.

Table 3-2. System Identification summary. Simulation.

Mode	$f\ [Hz]$	$\hat{f}[Hz]$	$e_f[\%]$	$\zeta\ [\%]$	$\hat{\zeta}[\%]$	$e_{\zeta}[\%]$	$MAC[\%]$
1	0.171	0.171	−0.266	1.000	1.553	+55.273	100.000
2	1.214	1.216	+0.179	1.000	0.838	−16.154	99.997
3	3.495	3.507	+0.353	1.000	1.038	+3.758	99.961

3.3 GPLFM – Parameter Estimation

This section focuses on assessing the parameter estimation methods within the GPLFM, as described in Section 2.4.5. The two methods, Maximum A Posteriori and Fitting the Prior and Posterior are applied to the simulation results. Note that only three modes are considered for the mechanical model used in GPLFM.

3.3.1 Maximum A Posteriori

The drawbacks of this method have been discussed in 2.4.5.1.1. To minimise these drawbacks, only the stochastic hyperparameters σ and l_{sc} are sought to be defined. The noise levels are taken as the exact values exposed in 3.1.3. Therefore, the noise matrix $\boldsymbol{R}$ is well defined.

The resulting surface for the energy function is shown in Figure 3-20. From the provided zoomed version of the energy function, the minimum might become clearer, and it may be found for the exact values of σ and l_{sc}. Exact values for the minimum are not provided however, as the analysis presented through Figure 3-20 yields enough information to discuss and compare with the other parameter estimation method: Fitting of the prior and posterior.

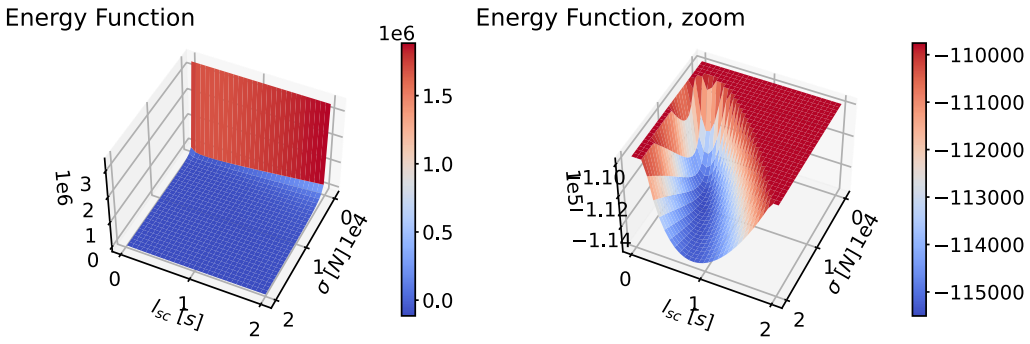

Figure 3-20. Energy function surface. Simulation.

3.3.2 Fitting of the prior and posterior

As discussed in 2.4.4.2, fitting the prior will yield the hyperparameters that will define the stochastic description of the load: σ and l_{sc}. The way that these will be defined is by ensuring that the resulting prior for the accelerations is a good match with the distribution obtained from the observations. The first step is defining the log-normal distributions for each measurement which will yield the likelihood that the prior is a good match with the observations. The log-normal distributions defined for each measurement are shown in Figure 3-21.

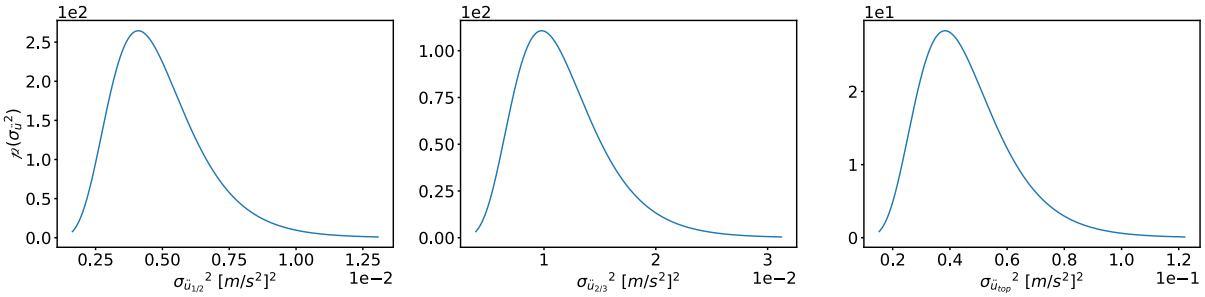

Figure 3-21. Log-normal distributions definition from measurement variance. Simulation.

The joint distribution surface is shown in Figure 3-22. The peak is clear and the resulting values and relative error are summarised in Table 3-3. The prior fit is illustrated in Figure 3-23 to Figure 3-25.

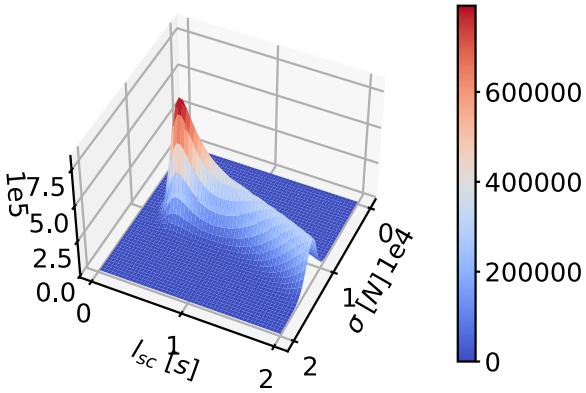

Figure 3-22. Joint distribution.

The posterior defines the noise levels in $\boldsymbol{R}$. The iterative process is illustrated in Figure 3-26. A tolerance of 1% is chosen. The results are summarised in Table 3-3. The posterior fit is illustrated in Figure 3-27 to Figure 3-29 by showing the distribution of the difference between the acceleration estimation and measurement: $r = \hat{y} - y$.

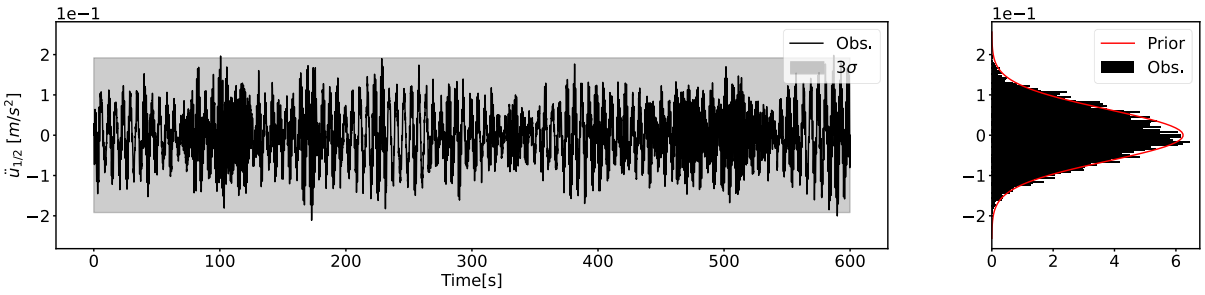

Figure 3-23. Prior fit. Acceleration at L/2.

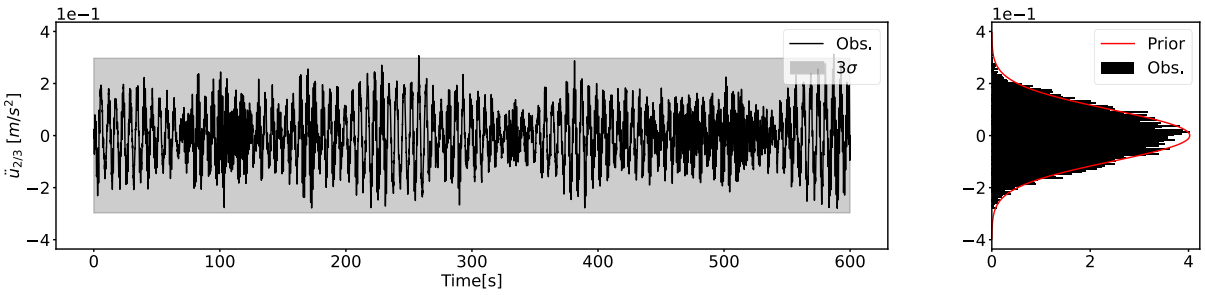

Figure 3-24. Prior fit. Acceleration at 2L/3.

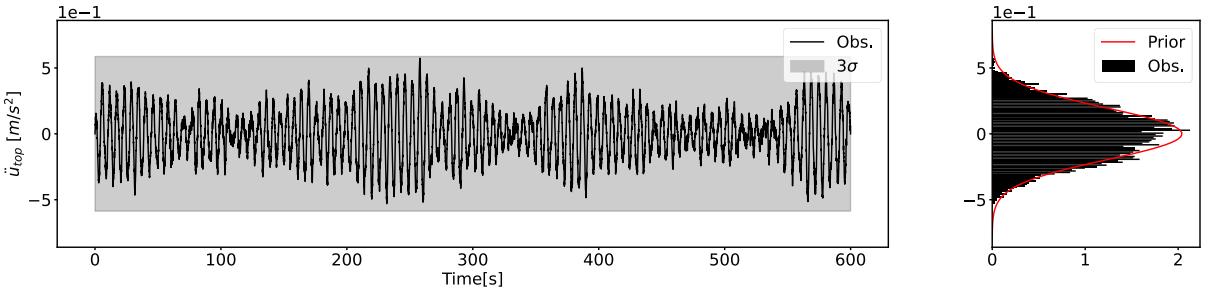

Figure 3-25. Prior fit. Acceleration at top.

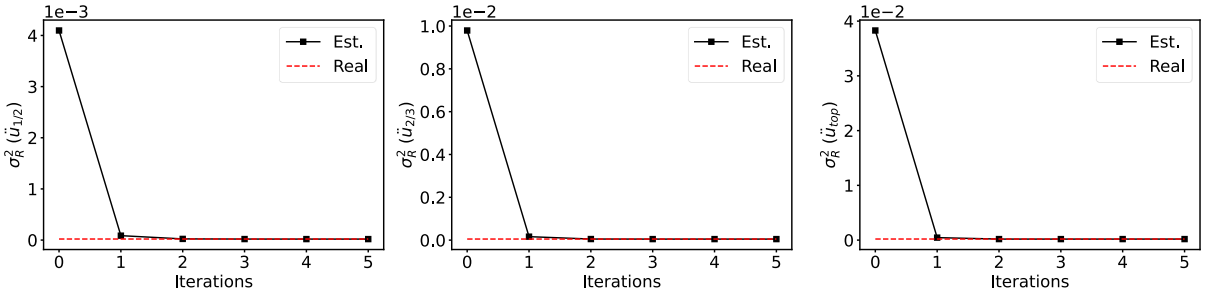

Figure 3-26. Posterior fit. Iterations. Tolerance: 1[%].

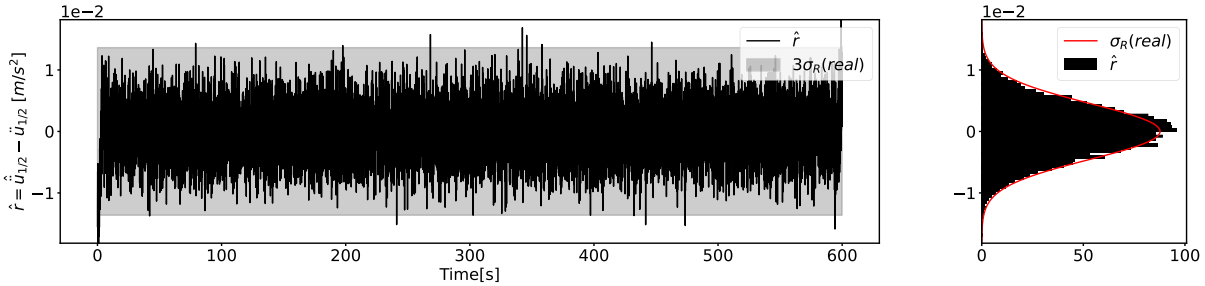

Figure 3-27. Posterior fit. Estimated noise on acceleration at L/2.

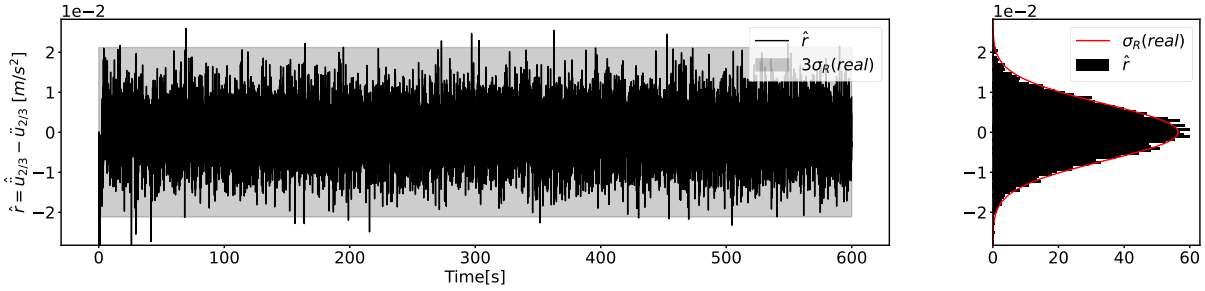

Figure 3-28. Posterior fit. Estimated noise on acceleration at 2L/3.

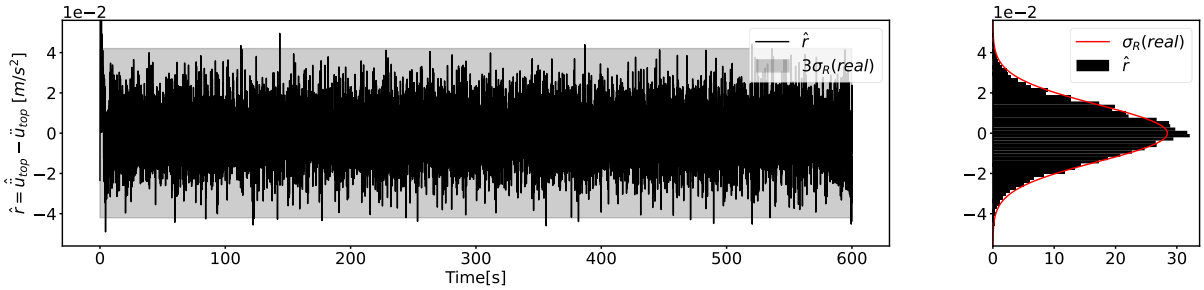

Figure 3-29. Posterior fit. Estimated noise on acceleration at top.

Table 3-3. Parameter estimation: Fitting the prior and posterior.

Parameter	Exact x	Estimation $\hat{x}$	Relative error e_x [%]
$\sigma\ [N]$	10 000	9 326	−6.74
$l_{sc}\ [s]$	0.500	0.435	−12.92
$\sigma_R\left(\ddot{u}_{1/2}\right)\left[\frac{m}{s^2}\right]$	4.54×10^{-3}	4.38×10^{-3}	−3.56
$\sigma_R\left(\ddot{u}_{2/3}\right)\left[\frac{m}{s^2}\right]$	7.06×10^{-3}	6.91×10^{-3}	−2.12
$\sigma_R\left(\ddot{u}_{top}\right)\left[\frac{m}{s^2}\right]$	14.01×10^{-3}	13.68×10^{-3}	−2.33

3.4 Response Estimation

The response estimation methods are compared in this section. Several noise levels are considered in the analysis, as introduced in 3.1.3.

3.4.1 MD&E

The methodology described in Section 2.3 is employed. Two modes are considered. The same filter described in section 3.1.3 Is applied after integration in the frequency domain. The estimated strain is shown in Figure 3-30 for the case with a SNR of 1: (0.5[%]). The MAE and $TRAC$ (see section 2.5) are summarised in Table 3-6 for all noise cases.

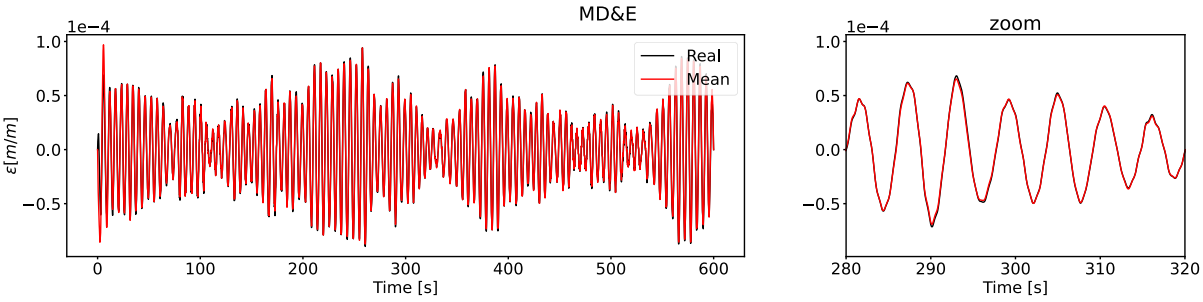

Figure 3-30. Strain estimation. MD&E. Simulation.

3.4.2 GPLFM

The same considerations as defined in 3.3 are employed. The parameter estimation results are summarised in Table 3-4 for all noise levels, and in Table 3-5 for the associated relative errors. Subsequently, Figure 3-31 shows the strain estimation for the case with a SNR of $1:(0.5[\%])$. The MAE and $TRAC$ (see section 1.4) are summarised in Table 3-6 for all noise cases.

Table 3-4. Parameter estimation. All noise levels. Simulation.

SNR	$\hat{\sigma}\ [N]$	$\hat{l}_{sc}\ [s]$	$\hat{\sigma}_R\left(\ddot{u}_{1/2}\right)\left[\frac{m}{s^2}\right]$	$\hat{\sigma}_R\left(\ddot{u}_{2/3}\right)\left[\frac{m}{s^2}\right]$	$\hat{\sigma}_R\left(\ddot{u}_{top}\right)\left[\frac{m}{s^2}\right]$
$1:(0.5[\%])$	9326	0.435	4.38×10^{-3}	6.91×10^{-3}	13.68×10^{-3}
$1:(1[\%])$	9345	0.435	5.90×10^{-3}	9.72×10^{-3}	19.32×10^{-3}
$1:(5[\%])$	9547	0.436	13.35×10^{-3}	21.41×10^{-3}	43.36×10^{-3}
$1:(10[\%])$	9761	0.434	18.90×10^{-3}	30.51×10^{-3}	60.59×10^{-3}

Table 3-5. Parameter estimation. All noise levels. Relative error. Simulation.

SNR	$e_\sigma\ [\%]$	$e_{l_{sc}}\ [\%]$	$e_{\sigma(\ddot{u}_{1/2})}\ [\%]$	$e_{\sigma(\ddot{u}_{2/3})}\ [\%]$	$e_{\sigma(\ddot{u}_{top})}\ [\%]$
$1:(0.5[\%])$	-6.74	-12.92	-3.56	-2.12	-2.33
$1:(1[\%])$	-6.55	-13.00	-8.16	-2.67	-2.46
$1:(5[\%])$	-4.53	-12.81	-7.06	-4.12	-2.11
$1:(10[\%])$	-2.39	-13.29	-7.01	-3.37	-3.28

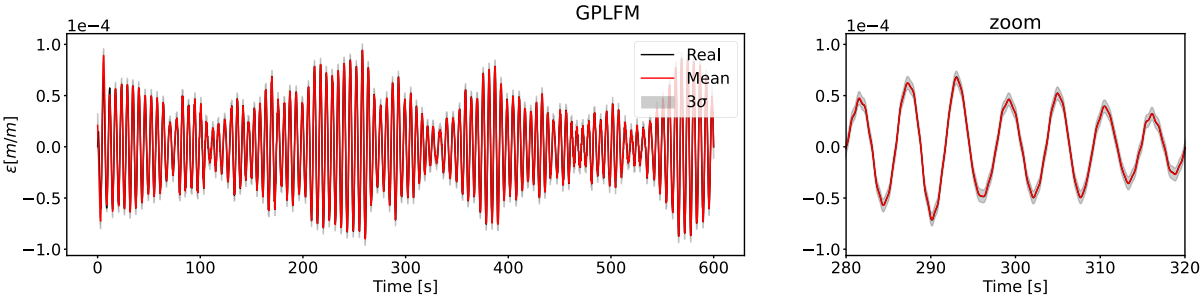

Figure 3-31. Strain estimation. GPLFM. Simulation.

3.4.3 Summary of results

Table 3-6 shows the summary of the error metrics obtained using both methods.

Table 3-6. Error Metrics. Strain estimation. Simulation.

	$GPLFM$		$MD\&E$	
SNR	$MAE(\varepsilon,\hat{\varepsilon})\left[\frac{m}{m}\right]$	$TRAC(\varepsilon,\hat{\varepsilon})\ [\%]$	$MAE(\varepsilon,\hat{\varepsilon})\left[\frac{m}{m}\right]$	$TRAC(\varepsilon,\hat{\varepsilon})\ [\%]$
$1:(0.5[\%])$	0.503×10^{-6}	99.66	1.575×10^{-6}	98.56
$1:(1[\%])$	0.636×10^{-6}	99.62	1.765×10^{-6}	98.49
$1:(5[\%])$	0.856×10^{-6}	99.76	2.612×10^{-6}	98.43
$1:(10[\%])$	1.111×10^{-6}	99.76	3.943×10^{-6}	97.72

3.5 Discussion

The system identification results, summarised in Table 3-2, validates and illustrates the methodology employed. Both frequencies and mode shapes are accurately obtained even for the third mode, characterised by a high amount of noise (see Figure 3-5 to Figure 3-7). The estimation for the damping ratio is observed to have noticeably lower accuracy, which is a well-known issue for system identification methods.

The parameter estimation results presented in section 3.3 illustrates additional drawbacks than the ones exposed in section 2.4.5.1.1 for the Maximum A Posteriori method. First, the computational cost of calculating the energy function was observed to be considerably higher in comparison with the alternative method (Fitting the prior and posterior). Second, the surface obtained for the energy function shown in Figure 3-20 illustrates the difficulty to distinguish the minima, this translates into the need to realise a robust optimisation process which adds to the computational cost of using this procedure. It is highlighted that this methodology is able to provide a solution for parameter estimation, the problem lies in the complexity associated with finding the solution.

The Fitting of the Prior and Posterior method for parameter estimation has been illustrated and validated through the simulation results in section 3.3.2 and section 3.4.2. Reasonable results were obtained for all noise levels considered for the simulation, as summarised in Table 3-5. Note that even though the results obtained are not exact, they are shown to be accurate enough to yield good results for response estimation (section 3.4).

As a consequence of the results obtained for parameter estimation, only the Fitting of the Prior and Posterior method is considered for the case study presented in section 4.

Finally, the response estimation methods are compared numerically, with the results summarised in Table 3-6. Both methodologies yield good results, but the obtained results are observed to be improved when using the GPLFM method for all cases.

4 Case Study: Onshore Wind Turbine

4.1 Measurement campaign

4.1.1 Structure description and sensor location

The structure under analysis is a three bladed horizontal axis wind turbine. The sensor locations and local axes are illustrated in Figure 4-1. All sensors are mounted on the inner surface of the tower. The acceleration sensors are bidirectional, and as shown in Figure 4-1, the local x direction will include a torsional component. Four unidirectional strain gauges are mounted at the bottom to obtain bending strains. All sensors measure at a sampling frequency of 20[Hz] ($\Delta t = 0.05[s]$).

The wind turbine is equipped with a Supervisory Control And Data Acquisition (SCADA) system. This system provides 10[mins.] average values of different operational conditions. The operational conditions are exposed in Section 4.1.2.

The records considered are from 09/12/2020 to 30/01/2021. Both accelerations and strain measurements are divided into 10[mins.] records for analysis.

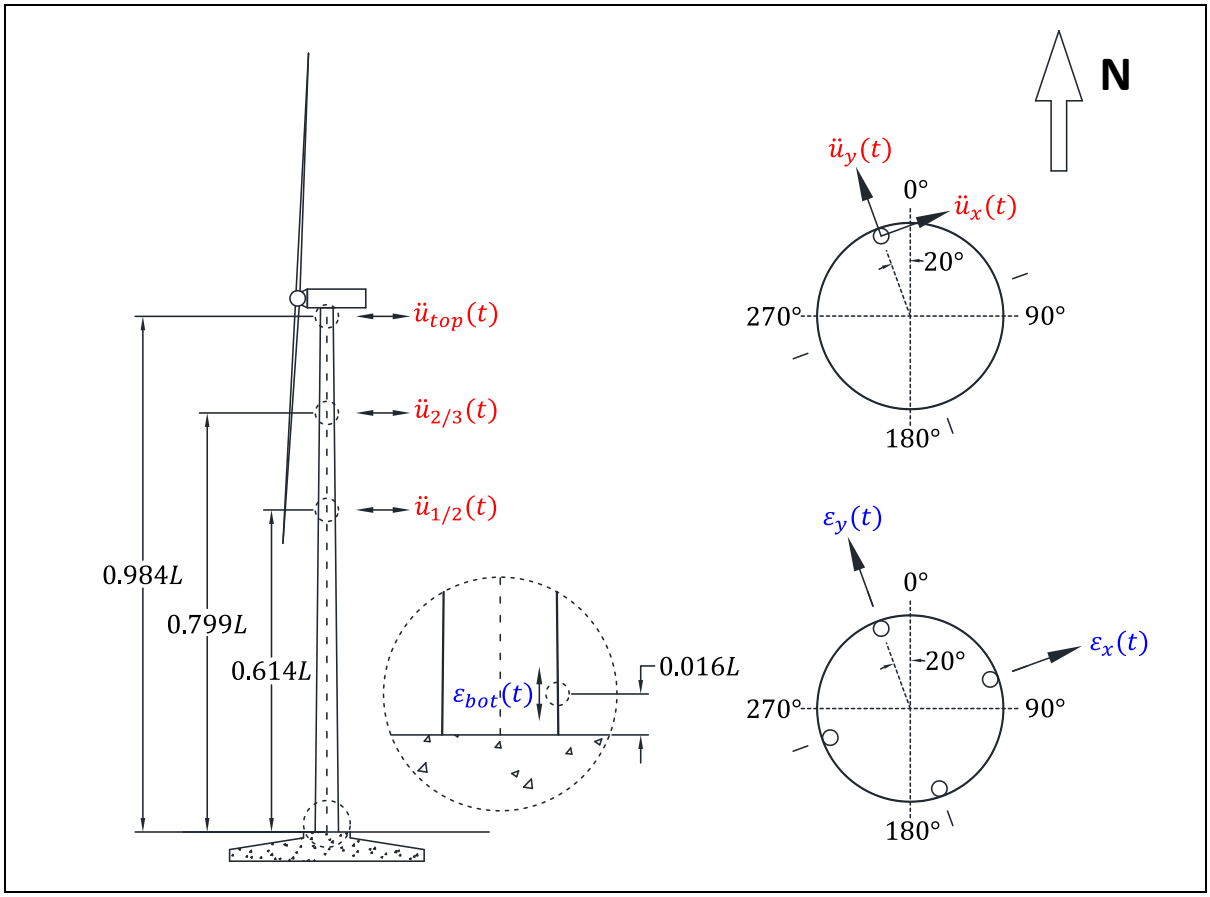

Figure 4-1. Sensor location and local axes.
Exact sensor location relative to the height L of the tower.

4.1.2 Operational Conditions: SCADA data

The following plots present the operational conditions associated to the available acceleration and strain measurements. Specifically, 10[min.] average values of: wind speed at hub height, rotor speed, output power, seconds in operation counter, wind direction, yaw angle and blade pitch (for each blade).

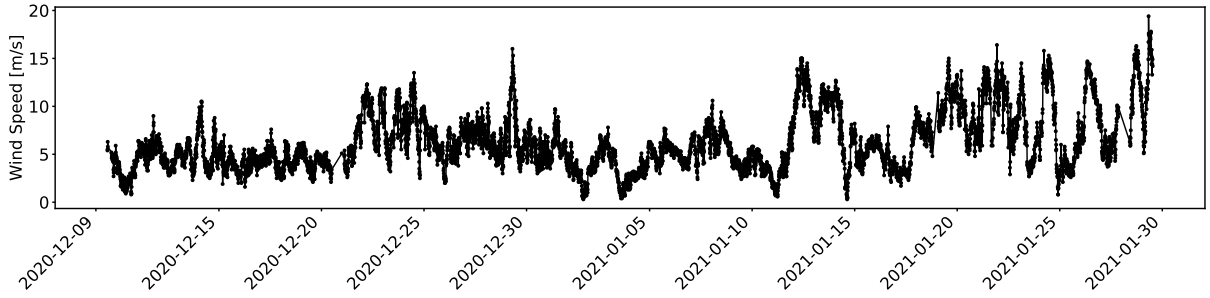

Figure 4-2. Wind Speed.

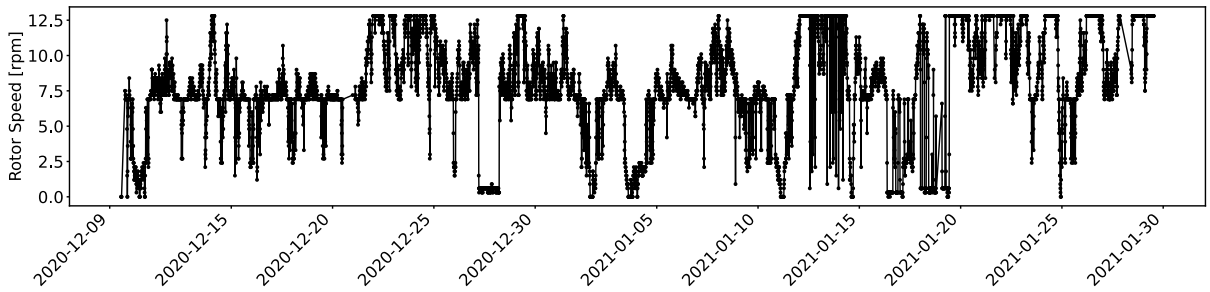

Figure 4-3. Rotor Speed.

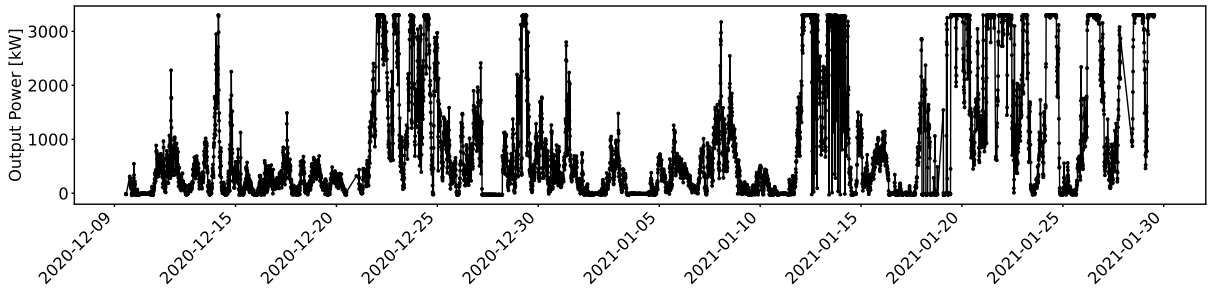

Figure 4-4. Output Power.

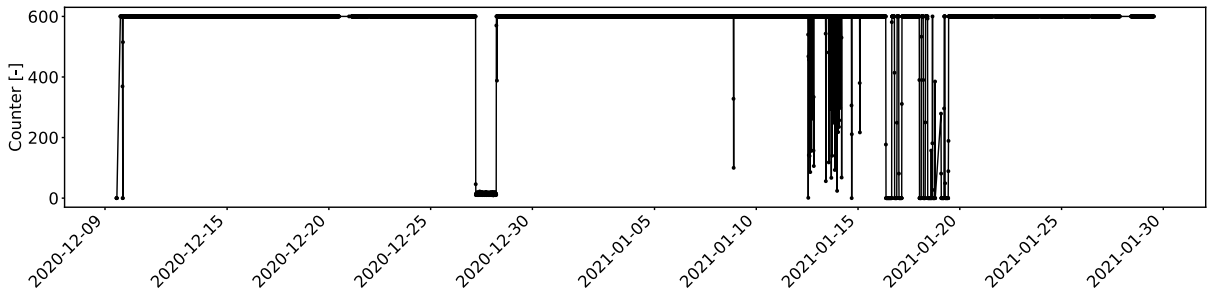

Figure 4-5. Seconds in operation counter.

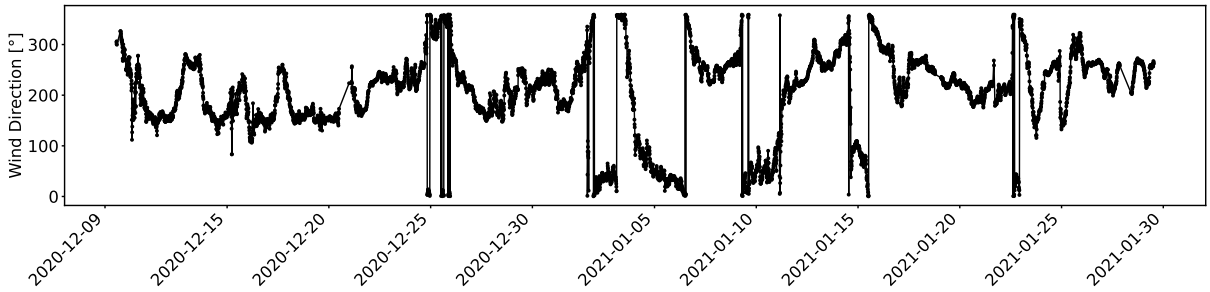

Figure 4-6. Wind Direction.

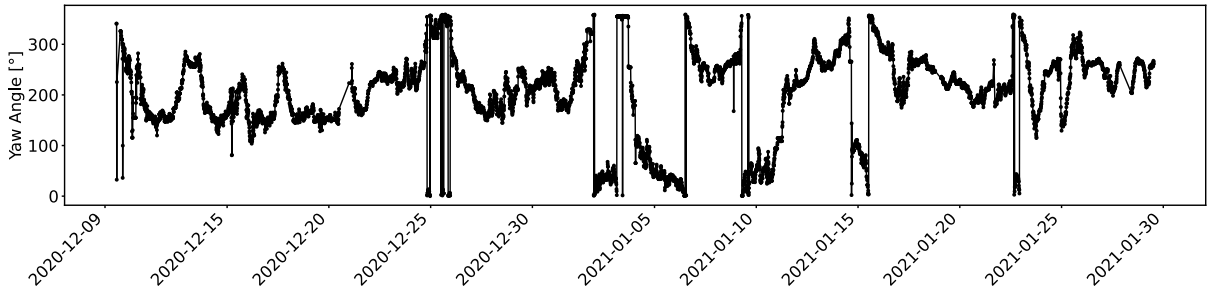

Figure 4-7. Yaw angle.

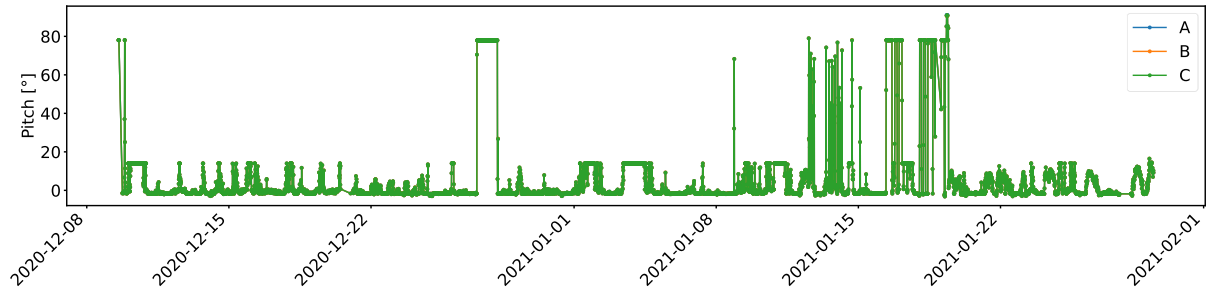

Figure 4-8. Blade pitch. Three blades: A, B, C.

4.1.3 Record Selection

Records are selected so as to cover the design situations for fatigue as defined in [42]. The design situations depend upon the cut-in and cut-out wind speed. For the wind turbine in analysis the cut-in wind speed is $V_{in} = 3\left[\frac{m}{s}\right]$ and the cut-out wind speed $V_{out} = 25\left[\frac{m}{s}\right]$. Table 4-1 summarises the specific records considered for analysis.

Table 4-1. Selected Records.

ID	Design Situation	Record	ID	Design Situation	Record
OP1	Power Production (v=4 [m/s])	2020-12-12 07:10:00	SU2	Start-up	2021-01-19 05:30:00
OP2	Power Production (v=6 [m/s])	2021-01-15 21:40:00	SU3	Start-up	2021-01-14 16:20:00
OP3	Power Production (v=8 [m/s])	2021-01-20 10:20:00	SD1	Normal Shut-Down	2021-01-16 08:50:00
OP4	Power Production (v=10 [m/s])	2020-12-22 06:50:00	SD2	Normal Shut-Down	2021-01-16 19:00:00
OP5	Power Production (v=12 [m/s])	2021-01-21 10:40:00	SD3	Normal Shut-Down	2021-01-17 00:10:00
OP6	Power Production (v=14 [m/s])	2021-01-24 13:00:00	PK1	Idling	2020-12-27 19:10:00
OP7	Power Production (v=16 [m/s])	2020-12-29 07:30:00	PK2	Idling	2020-12-20 11:30:00
SU1	Start-up	2021-01-19 10:30:00	PK3	Idling	2021-01-01 18:50:00

4.2 System Identification and Mechanical Model

4.2.1 System Identification

The procedure defined in section 2.2, and illustrated in section 3.2, is applied for the record PK1. Note that idling conditions are used for identification in order to best comply with the white gaussian noise assumptions present in SSI-Cov, as operational conditions will always have a harmonic load due to the tower shadow effect (see 1.2.1).

Figure 4-9 and Figure 4-10 shows the acceleration records and their frequency content. No pre-processing is applied. Subsequently, Figure 4-11 and Figure 4-12 shows the identification and clustering process for the FA and SS direction. The transformation into the FA and SS direction is realised taking into account a yaw angle of 158.3[°] with respect to the north (see Figure 4-1). The yaw angle is provided from the operational conditions (see Figure 4-7).

Model orders n_o in the range of 10 to 75 were used. The stabilisation diagram is cleared considering a maximum frequency of $f_{max} = 5[Hz]$ and a maximum damping ratio of $\zeta_{max} = 20[\%]$. The clustering process is applied using clusters that appear consistently at least for a third of the stabilisation diagram: $\alpha_{MinObj} = \frac{1}{3} \rightarrow MinObj = 21$.

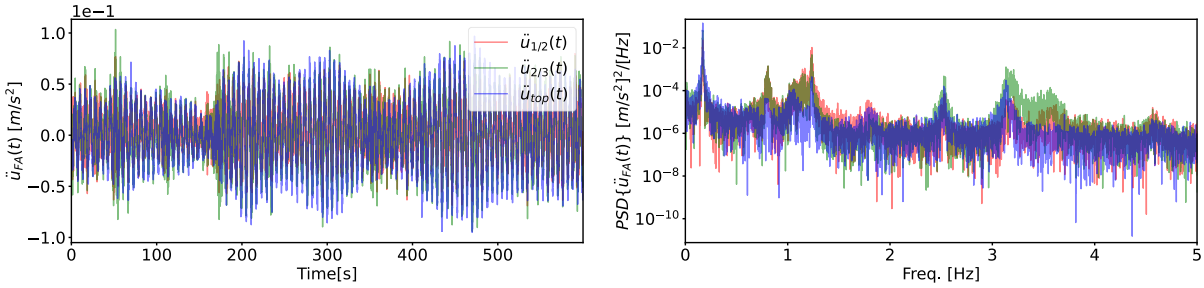

Figure 4-9. Acceleration measurements. FA direction. Time-History (left) and Power Spectral Density (right).

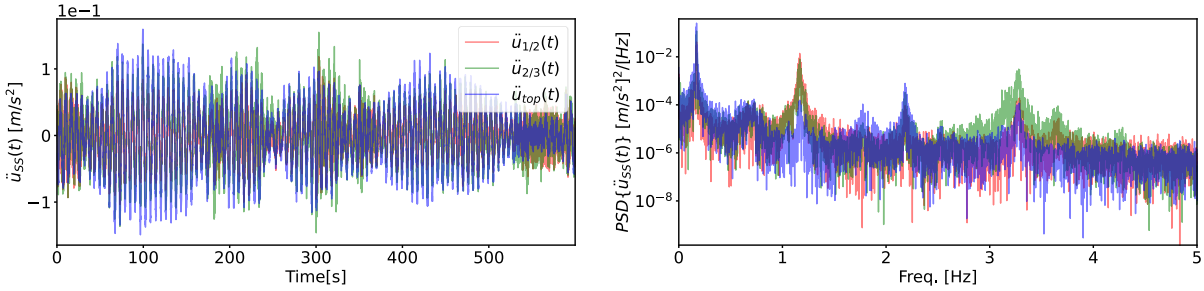

Figure 4-10. Acceleration measurements. SS direction. Time-History (left) and Power Spectral Density (right).

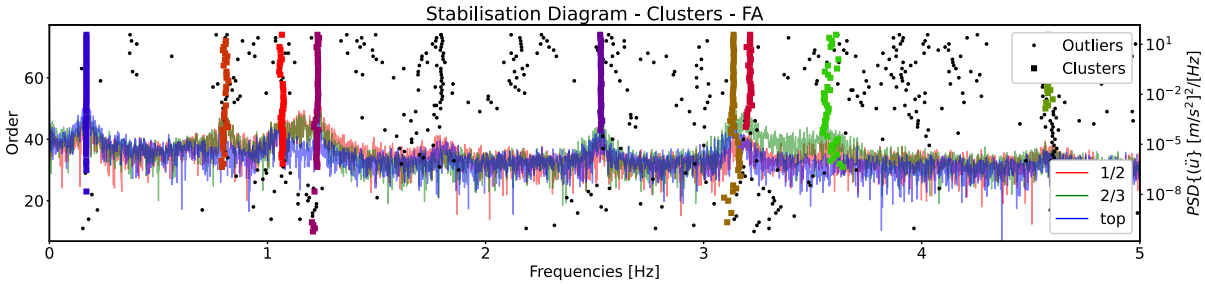

Figure 4-11. Stabilisation diagram, clusters. FA direction.

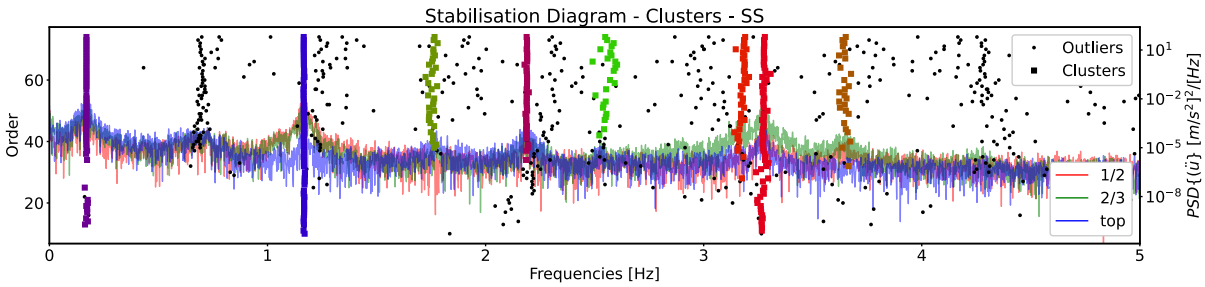

Figure 4-12. Stabilisation diagram, cluster. SS direction.

4.2.2 Mechanical Model

The mechanical model is initially considered to be the same model described in section 3.1. The only difference is the use of $n = 300$ elements to ensure that the variable geometry of the tower is well captured. Figure 4-13 shows the first three modes, along with the sensor locations. Note that the location of the load on the top of the tower (see Figure 3-3) is part of the mechanical model when applying the GPLFM method.

The frequencies and mode shapes are compared with the identification results in Table 4-2 and Table 4-3 for FA and SS directions, respectively. The identified modes are highlighted in the tables. Note that the identification of the third mode is not conclusive. This is discussed in section 4.5. Finally, taking into account the high error that can be expected in the damping estimation, as illustrated in section 3.2, a damping ratio of 0.75[%] is arbitrarily used for all modes.

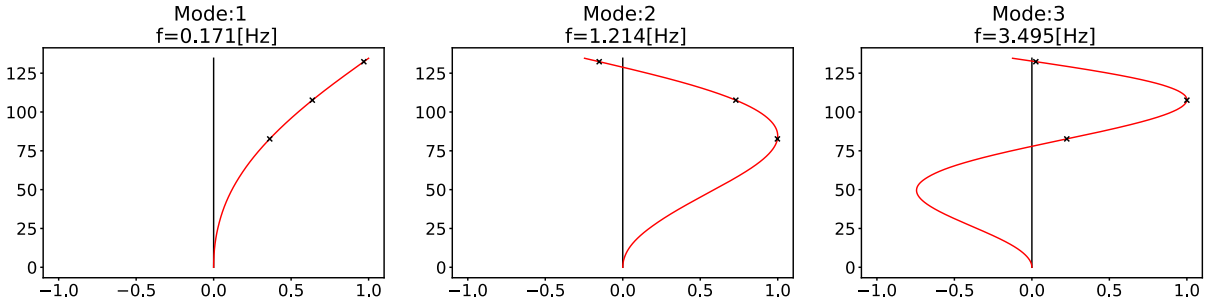

Figure 4-13. Mechanical model first three modes. Mode shapes and frequencies. Damping ratio: $\zeta = 0.75\%$ for all modes. Sensor locations are marked with 'x'.

Table 4-2. System Identification vs Mechanical Model. FA direction.

$\hat{f}[Hz]$	$\hat{\zeta}[\%]$	MAC [%] ($f_1 = 0.17[Hz]$)	MAC [%] ($f_2 = 1.21[Hz]$)	MAC [%] ($f_3 = 3.50[Hz]$)
0.17	**0.36**	**99.97**	21.30	35.82
0.80	1.43	45.59	91.93	70.31
1.07	2.65	69.20	75.52	61.64
1.23	**1.04**	16.68	**99.74**	51.15
2.53	0.41	48.84	3.48	58.02
3.14	0.59	69.69	38.51	86.65
3.21	**0.88**	41.69	53.83	**99.59**
3.57	**1.65**	29.02	71.42	**96.76**
4.58	0.68	4.94	94.26	40.99

Table 4-3. System Identification vs Mechanical Model. SS direction.

$\hat{f}[Hz]$	$\hat{\zeta}[\%]$	MAC [%] ($f_1 = 0.17[Hz]$)	MAC [%] ($f_2 = 1.21[Hz]$)	MAC [%] ($f_3 = 3.50[Hz]$)
0.17	**1.19**	**99.92**	22.45	37.51
1.17	**0.60**	22.63	**99.91**	56.62
1.76	2.57	85.89	0.88	18.05
2.19	0.45	99.98	20.60	37.00
2.55	1.56	57.38	5.11	58.99
3.18	**0.79**	42.94	42.78	**97.82**
3.28	**0.46**	51.23	52.48	**97.48**
3.65	**0.61**	30.58	77.91	**94.09**

4.3 Response Estimation

The results of applying the two response estimation methods to the selected records (see Table 4-1) is presented in this section. The process is illustrated by record OP6 in both directions. A high-pass Butterworth filter of order 4 with cut-off frequency $f = 0.1[Hz]$ is applied to the simulated measurements (accelerations and strains), as quasi-static information cannot be retrieved from acceleration measurements. Figure 4-14 to Figure 4-21 shows the unfiltered and filtered records, accelerations, and strains, for both directions.

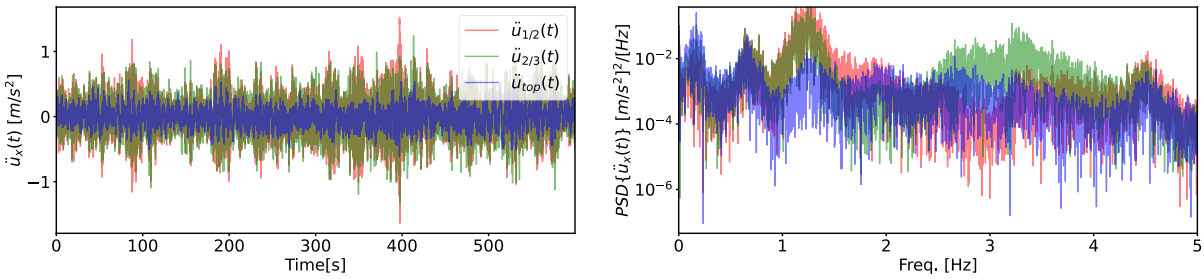

Figure 4-14. Acceleration records OP6-x. Unfiltered. Time-History (left) and Power Spectral Density (right).

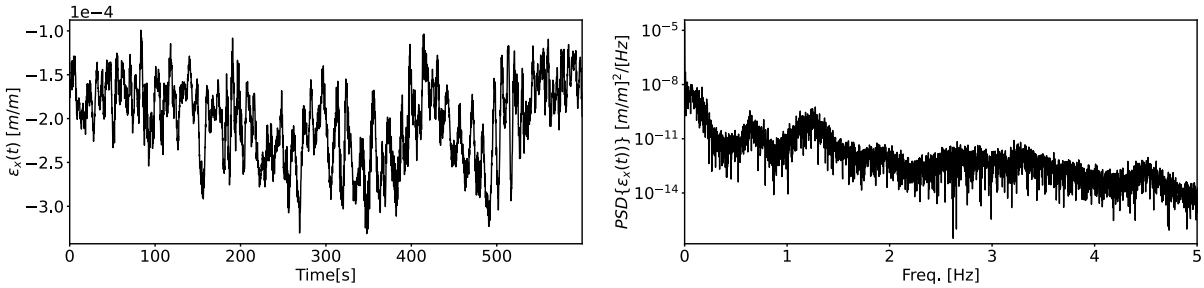

Figure 4-15. Strain record OP6-x. Unfiltered. Time-History (left) and Power Spectral Density (right).

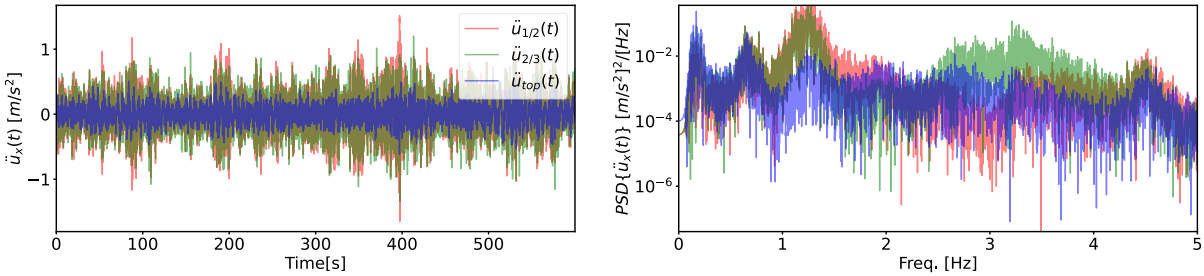

Figure 4-16. Acceleration records OP6-x. Filtered. Time-History (left) and Power Spectral Density (right).

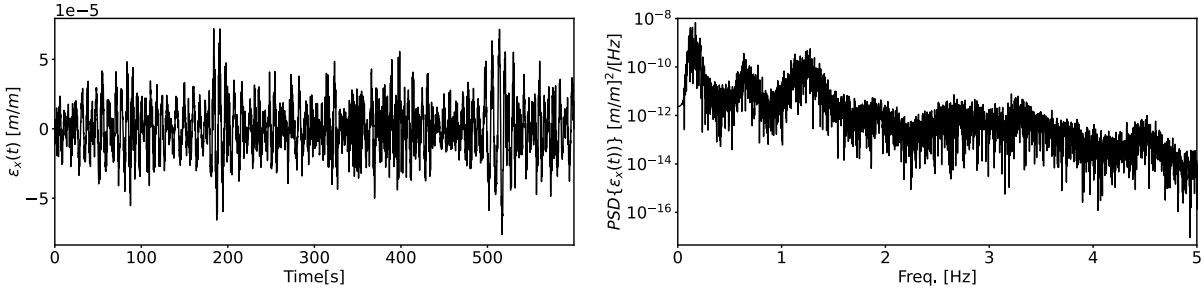

Figure 4-17. Strain record OP6-x. Filtered. Time-History (left) and Power Spectral Density (right).

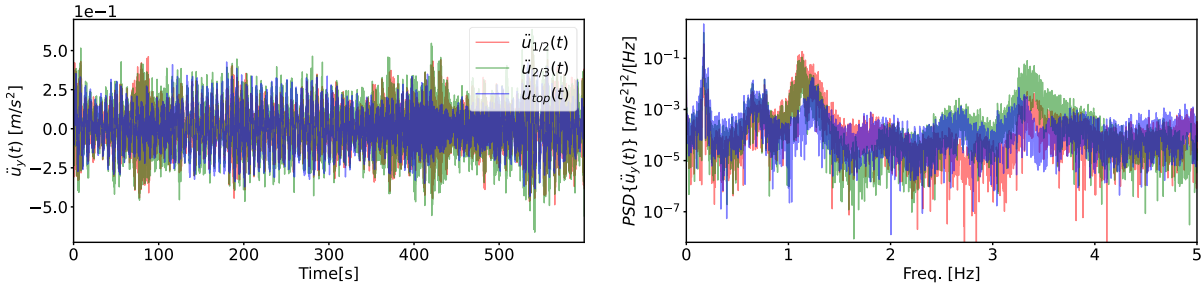

Figure 4-18. Acceleration records OP6-y. Unfiltered. Time-History (left) and Power Spectral Density (right).

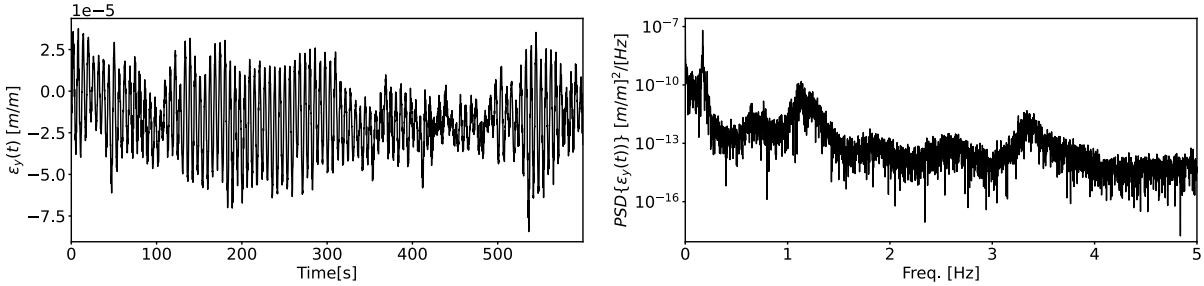

Figure 4-19. Strain record OP6-y. Unfiltered. Time-History (left) and Power Spectral Density (right).

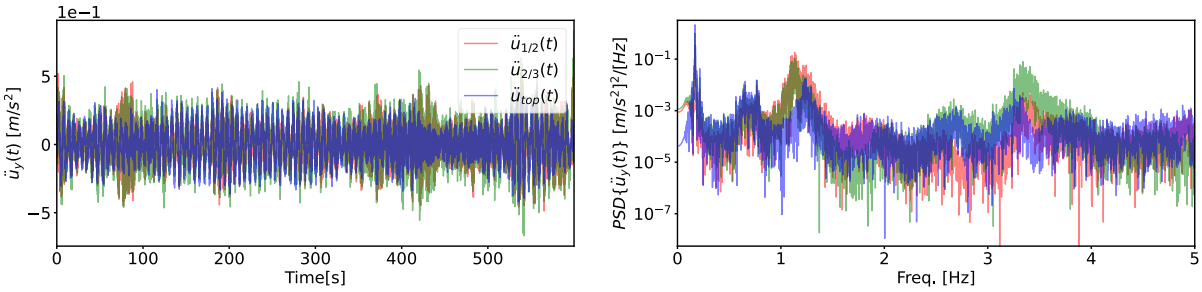

Figure 4-20. Acceleration records OP6-y. Filtered. Time-History (left) and Power Spectral Density (right).

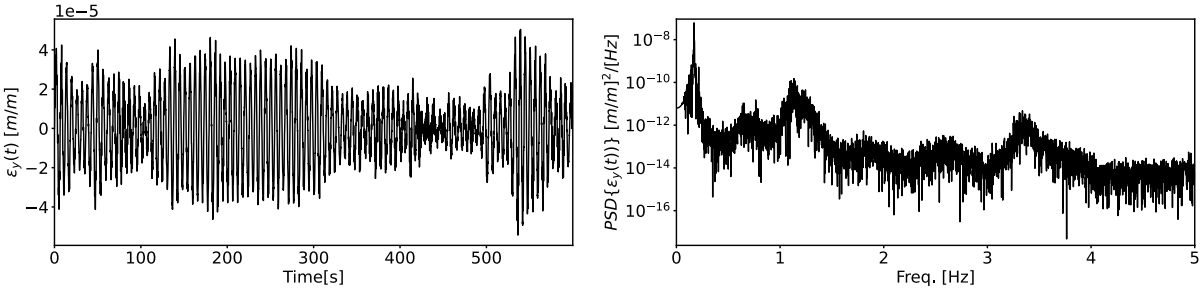

Figure 4-21. Strain record OP6-y. Filtered. Time-History (left) and Power Spectral Density (right).

4.3.1 GPLFM

The GPLFM considers three modes and, as a consequence of the simulation results discussed in section 3.5, only the Fitting of the Prior and Posterior method is used for parameter estimation.

The fitting of the prior is applied considering an upper bound for l_{sc}. The upper bound is defined by imposing that the expected frequency content of the load should be higher than the quasi-static limit. In consistency with section 2.4.2.3, this translates into imposing that the relevant frequencies be higher than the quasi-static frequency of $f = 0.1[Hz]$: $\frac{1}{5l_{sc}} > 0.1[Hz] \Rightarrow l_{sc} < 2[s]$. An upper bound is considered for σ from a preliminary analysis of high wind operational conditions: $\sigma < 5 \times 10^4\ [N]$. The maximisation of the joint distribution is computed using python built-in optimisation tools with bound constraints. The initial guess is defined by first computing the surface and finding the maximum. The process is illustrated by record OP6. The joint distribution surface is shown in Figure 4-22, for both directions, and the prior fit is shown in Figure 4-26 to Figure 4-28 for each acceleration measurement. A summary of the parameter estimation for all records analysed is shown in Table 4-4 and Table 4-5 for local directions x and y respectively. Note that the prior is not a perfect match. This is discussed in section 4.5.

The fitting of the posterior considers a tolerance of 1[%] (see section 2.4.5.2.2). This method was observed to diverge in approximately 30[%] of the records. In order to ensure convergence, the iteration is stopped if the relative difference (see section 2.4.5.2.2) stops decreasing. Figure 4-29 and Figure 4-30 shows the noise levels found for each iteration, for local direction x and y respectively. Note that direction x is one of the records for which the iteration was stopped. It is observed that if the iteration is not stopped, the noise level defined for the sensor in the top will keep decreasing, and the noise levels on the sensors at 2L/3 and L/2 will keep increasing. A discussion regarding this stage can be found in section 4.5. Subsequently, the estimated noise is compared with the defined noise in Figure 4-31 to Figure 4-36 for each sensor and each direction. It is highlighted that, in contrast to the results shown in section 3.3.2, the estimated distribution $\widehat{\boldsymbol{R}}$ is compared to the defined distribution for the estimation $\boldsymbol{R}$. The results shown in section 3.3.2 are compared to the real values defined for the simulation. A summary of the parameter estimation for all records analysed is shown in Table 4-4 and Table 4-5 for local directions x and y respectively.

Figure 4-37 and Figure 4-38 shows the strain estimation obtained for the record OP6, for each direction. The MAE and $TRAC$ are summarised in Table 4-6 and Table 4-7 for all analysed records.

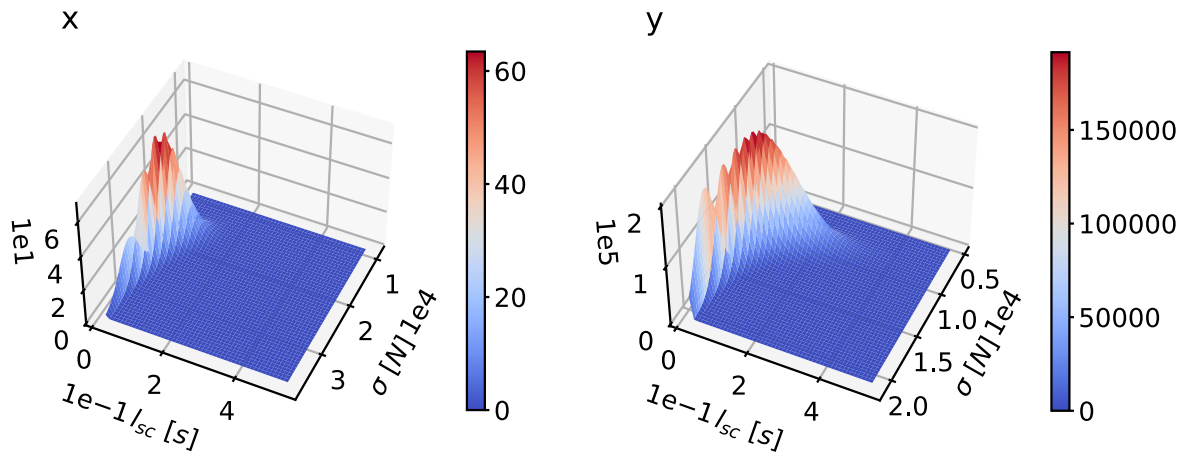

Figure 4-22. Joint distribution surface. Record OP6.
Local x direction (left) and Local y direction (right).

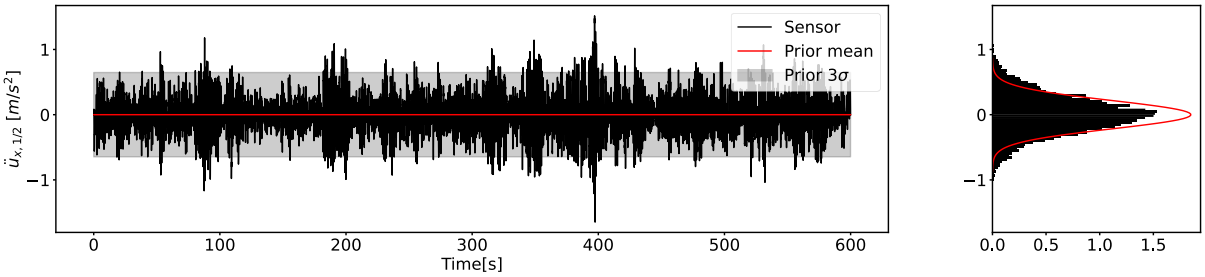

Figure 4-23. Prior fit. Acceleration at L/2. Record OP6-x.

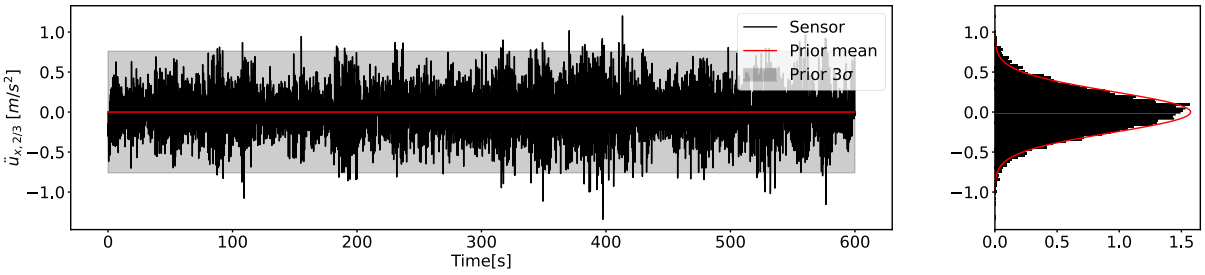

Figure 4-24. Prior fit. Acceleration at 2L/3. Record OP6-x.

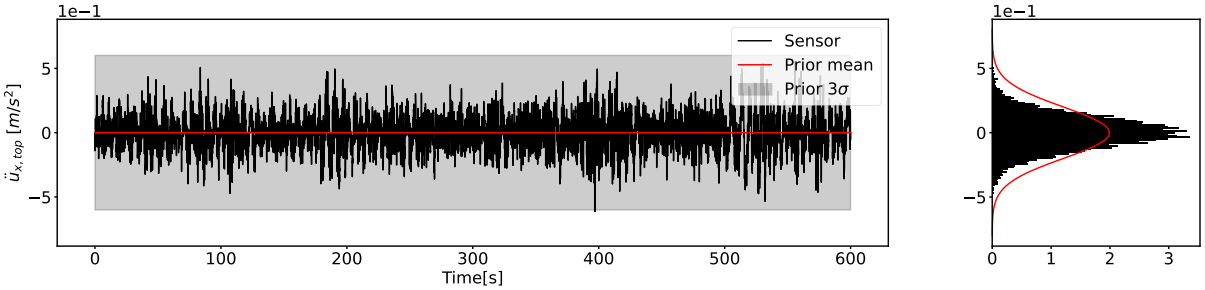

Figure 4-25. Prior fit. Acceleration at top. Record OP6-x.

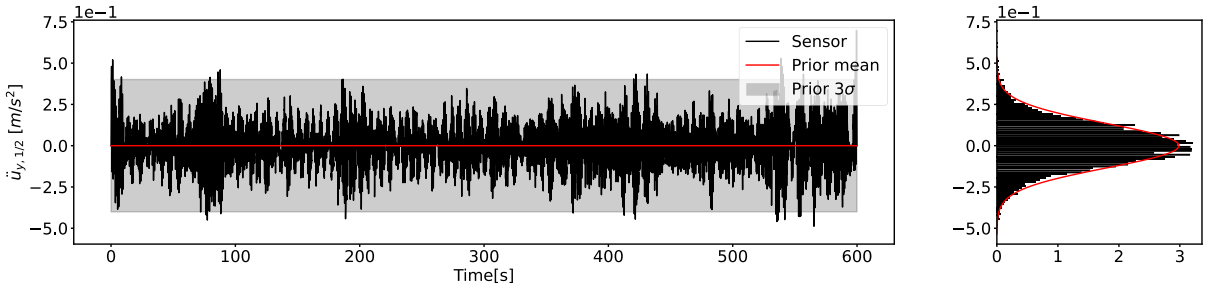

Figure 4-26. Prior fit. Acceleration at L/2. Record OP6-y.

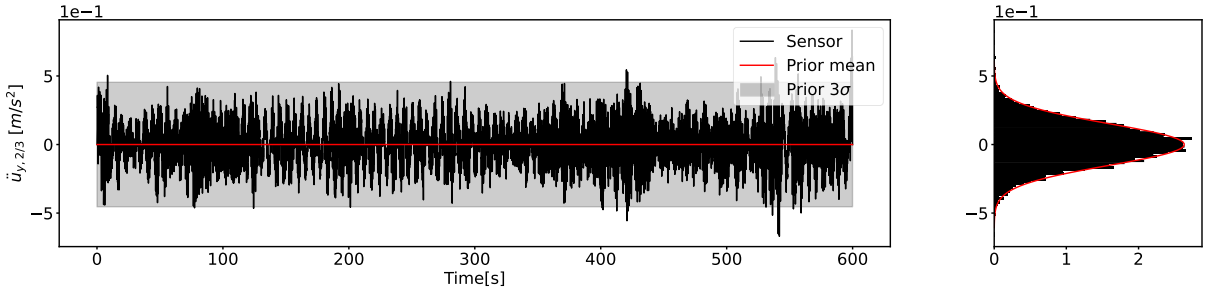

Figure 4-27. Prior fit. Acceleration at 2L/3. Record OP6-y.

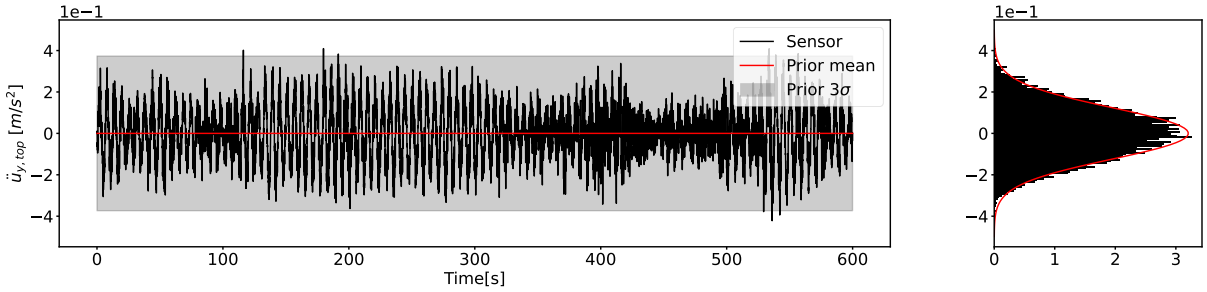

Figure 4-28. Prior fit. Acceleration at top. Record OP6-y.

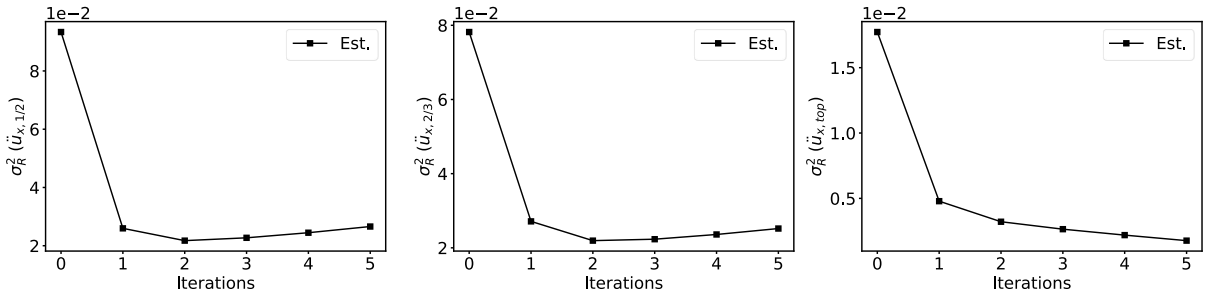

Figure 4-29. Posterior fit. Iterations. Record OP6-x.

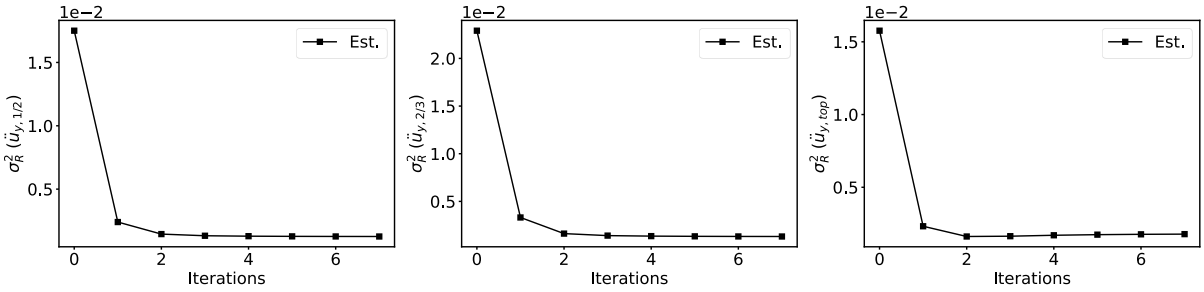

Figure 4-30. Posterior fit. Iterations. Record OP6-y.

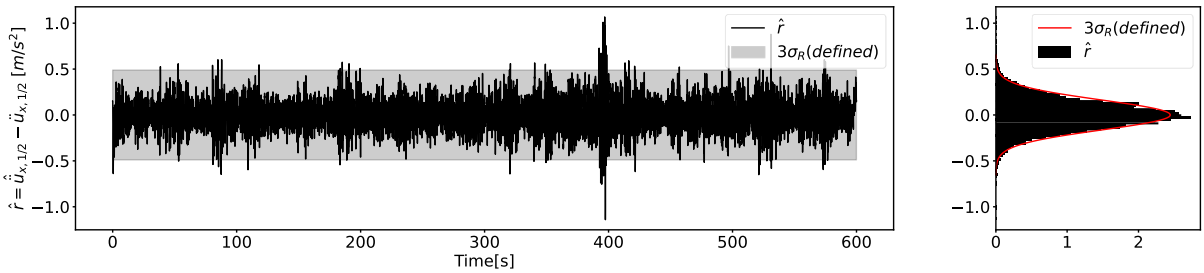

Figure 4-31. Posterior fit. Acceleration at L/2. Record OP6-x.

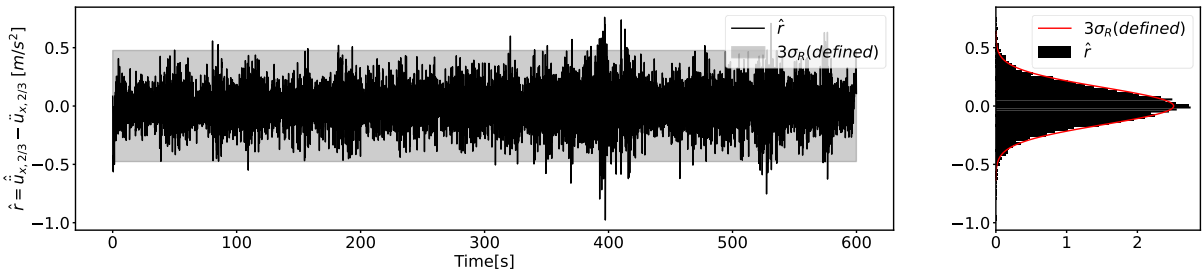

Figure 4-32. Posterior fit. Acceleration at 2L/4. Record OP6-x.

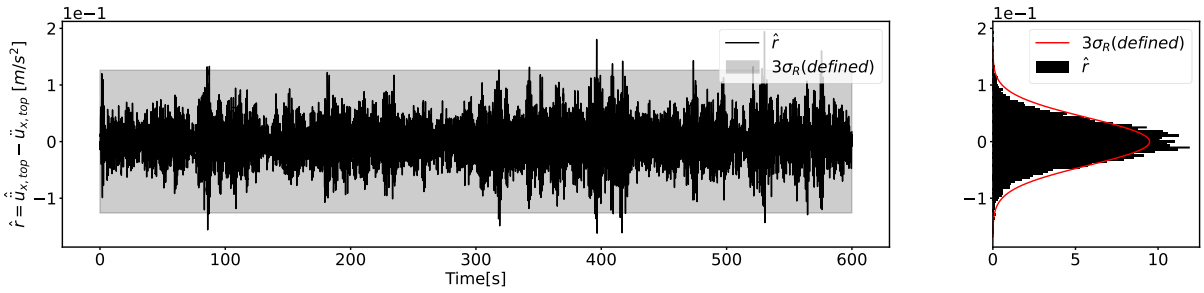

Figure 4-33. Posterior fit. Acceleration at top. Record OP6-x.

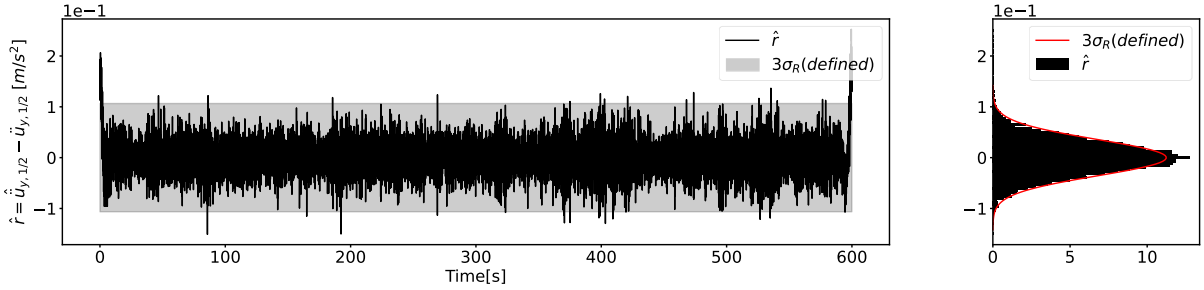

Figure 4-34. Posterior fit. Acceleration at L/2. Record OP6-y.

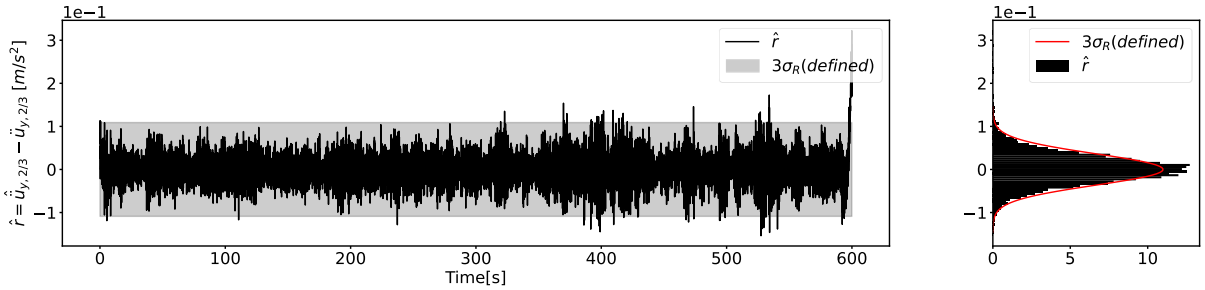

Figure 4-35. Posterior fit. Acceleration at 2L/3. Record OP6-y.

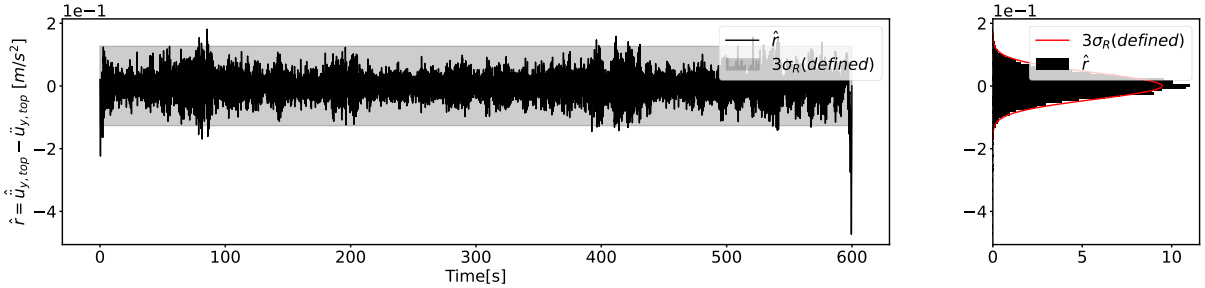

Figure 4-36. Posterior fit. Acceleration at top. Record OP6-y.

Table 4-4. Parameter estimation. All records. Local direction x.

ID	$\sigma[N]$	$l_{sc}[s]$	$\hat{\sigma}_R\left(\ddot{u}_{1/2}\right) \times 10^{-3}\left[\frac{m}{s^2}\right]$	$\hat{\sigma}_R\left(\ddot{u}_{2/3}\right) \times 10^{-3}\left[\frac{m}{s^2}\right]$	$\hat{\sigma}_R\left(\ddot{u}_{top}\right) \times 10^{-3}\left[\frac{m}{s^2}\right]$	tol[%]
OP1-x	3961	0.046	17.30	12.53	16.53	0.67
OP2-x	2049	0.045	13.40	11.08	7.06	1.00
OP3-x	10319	0.048	43.42	42.34	40.15	0.88
OP4-x	13179	0.048	70.85	70.99	38.14	0.86
OP5-x	14404	0.045	69.02	73.30	46.19	5.48
OP6-x	20845	0.050	163.07	158.74	42.04	19.30
OP7-x	15928	0.050	64.24	69.21	66.77	0.90
SU1-x	5952	0.052	21.12	21.52	25.09	0.79
SU2-x	7008	0.048	28.55	29.60	27.84	0.93
SU3-x	866	0.034	6.56	7.93	1.63	46.64
SD1-x	2092	0.268	10.43	13.91	8.22	0.91
SD2-x	3849	0.053	14.65	13.74	13.89	0.97
SD3-x	1742	0.056	10.31	10.90	3.08	30.01
PK1-x	2556	0.318	6.41	11.35	4.95	1.00
PK2-x	462	0.300	3.77	3.59	2.85	0.72
PK3-x	368	0.050	3.59	3.69	1.92	0.92

Table 4-5. Parameter estimation. All records. Local direction y.

ID	$\sigma[N]$	$l_{sc}[s]$	$\hat{\sigma}_R(\ddot{u}_{1/2}) \times 10^{-3}\left[\frac{m}{s^2}\right]$	$\hat{\sigma}_R(\ddot{u}_{2/3}) \times 10^{-3}\left[\frac{m}{s^2}\right]$	$\hat{\sigma}_R(\ddot{u}_{top}) \times 10^{-3}\left[\frac{m}{s^2}\right]$	tol[%]
OP1-y	4993	0.046	28.39	27.40	14.41	0.97
OP2-y	2592	0.045	16.73	17.93	3.96	0.93
OP3-y	10859	0.046	39.35	34.90	48.74	0.66
OP4-y	9557	0.050	43.16	42.83	26.57	3.36
OP5-y	11911	0.051	57.96	58.52	33.86	3.96
OP6-y	11983	0.061	35.52	36.30	42.32	0.73
OP7-y	14404	0.050	79.46	78.27	28.33	6.57
SU1-y	5532	0.052	20.71	20.22	19.36	0.93
SU2-y	6004	0.051	24.75	24.92	13.71	0.24
SU3-y	498	0.194	3.99	5.09	3.92	0.80
SD1-y	2848	0.021	9.13	9.52	1.02	87.99
SD2-y	3538	0.056	11.98	10.29	11.27	0.76
SD3-y	1530	0.069	9.71	10.42	1.57	2.21
PK1-y	1895	0.285	7.07	9.43	3.22	0.77
PK2-y	354	0.220	3.47	3.65	2.68	0.46
PK3-y	296	0.077	3.58	3.15	2.20	0.88

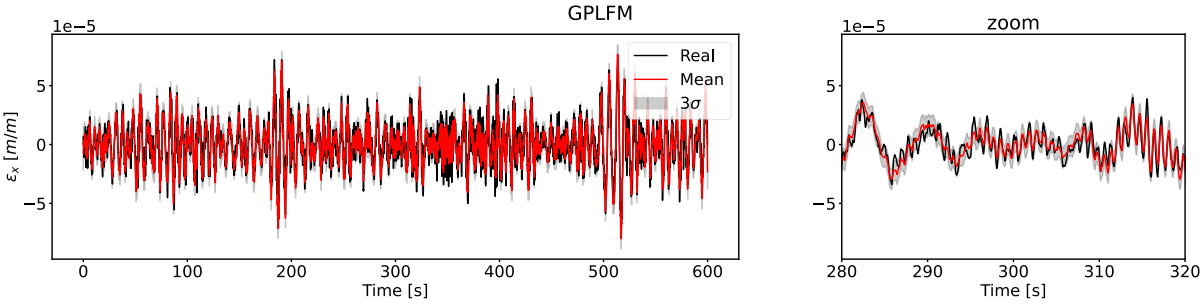

Figure 4-37. Strain estimation. Record OP6-x. GPLFM.

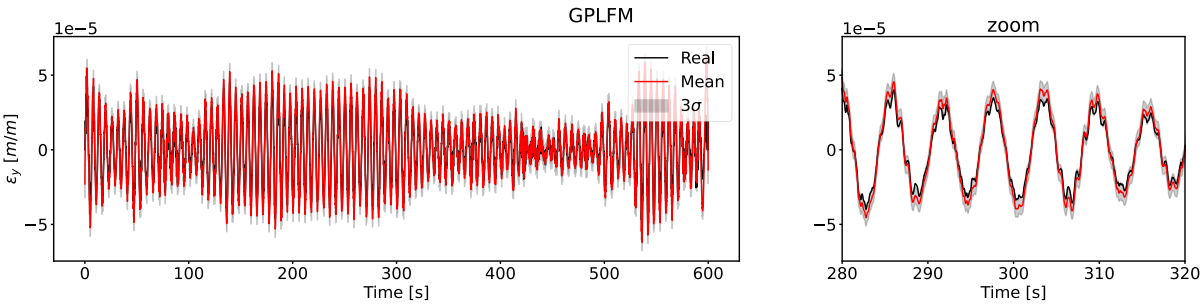

Figure 4-38. Strain estimation. Record OP6-y. GPLFM.

4.3.2 MD&E

Only two modes are used for the MD&E method. The same filter described in section 4.3 is applied after integration in the frequency domain. Figure 4-39 and Figure 4-40 shows the results for record OP6 in both directions. The MAE and $TRAC$ are summarised in Table 4-6 and Table 4-7 for all analysed records.

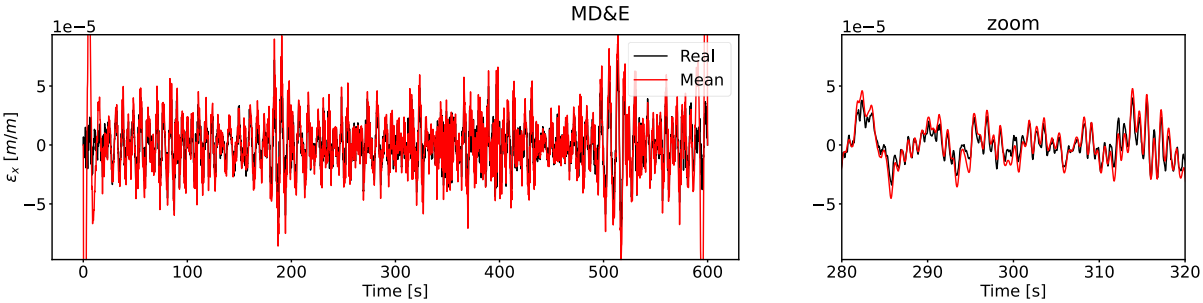

Figure 4-39. Strain estimation. Record OP6-x. MD&E.

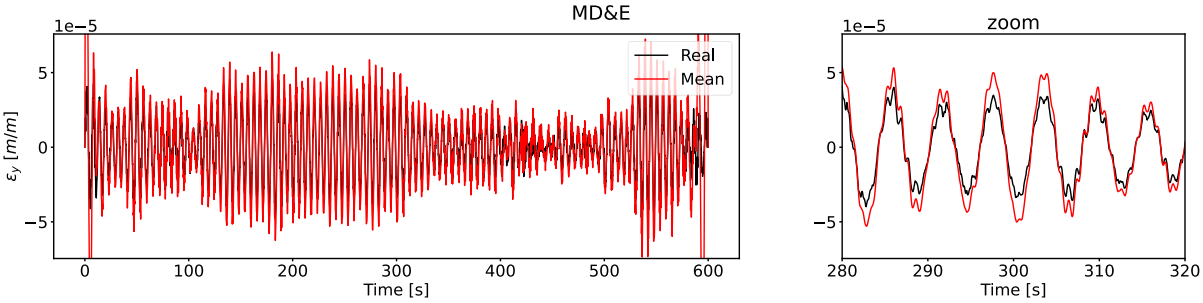

Figure 4-40. Strain estimation. Record OP6-y. MD&E.

4.3.3 Summary of results

The error metrics are summarised in Table 4-6 and Table 4-7 for both response estimation methods and all records under analysis, local directions x and y respectively. Note that, as illustrated in Figure 4-38 and Figure 4-40, the estimation of both methods in the initial and final seconds of the records is inaccurate, with a more noticeable error for MD&E. Therefore, the first and last 100[s] are disregarded so as to provide a fair comparison between the methodologies employed.

Table 4-6. Error Metrics. All records. Local direction x.

	GPLFM		*MD&E*	
ID	$MAE(\varepsilon,\hat{\varepsilon})$ $\times 10^{-6}[m/m]$	$TRAC(\varepsilon,\hat{\varepsilon})$ [%]	$MAE(\varepsilon,\hat{\varepsilon})$ $\times 10^{-6}[m/m]$	$TRAC(\varepsilon,\hat{\varepsilon})$ [%]
OP1-x	0.45	91.22	2.89	33.61
OP2-x	0.55	81.28	1.04	71.59
OP3-x	1.34	95.69	2.65	93.15
OP4-x	2.14	94.38	3.69	94.56
OP5-x	2.40	95.80	4.15	95.48
OP6-x	4.72	86.08	5.79	91.88
OP7-x	2.14	96.12	4.13	93.65
SU1-x	0.87	99.14	1.85	96.55
SU2-x	0.78	96.01	1.94	92.93
SU3-x	0.19	67.44	0.91	23.33
SD1-x	1.10	99.67	2.48	96.79
SD2-x	0.66	94.91	2.33	73.63
SD3-x	0.31	98.97	1.06	91.80
PK1-x	1.27	99.80	3.32	98.80
PK2-x	0.27	99.11	0.94	72.71
PK3-x	0.09	85.42	0.91	14.21

Table 4-7. Error metrics. All records. Local direction y.

	$GPLFM$		$MD\&E$	
ID	$MAE(\varepsilon,\hat{\varepsilon})$ $\times 10^{-6}[m/m]$	$TRAC(\varepsilon,\hat{\varepsilon})$ $[\%]$	$MAE(\varepsilon,\hat{\varepsilon})$ $\times 10^{-6}[m/m]$	$TRAC(\varepsilon,\hat{\varepsilon})$ $[\%]$
OP1-y	1.05	83.88	1.62	81.33
OP2-y	0.93	73.60	1.78	57.44
OP3-y	1.33	93.34	3.99	76.54
OP4-y	1.60	94.55	3.49	87.19
OP5-y	2.09	94.58	3.98	93.37
OP6-y	2.87	99.69	6.34	98.11
OP7-y	2.52	90.93	3.74	90.82
SU1-y	0.79	98.72	1.87	93.09
SU2-y	0.84	96.83	1.93	92.11
SU3-y	0.26	93.67	1.05	47.86
SD1-y	0.61	99.18	2.47	83.80
SD2-y	0.78	97.77	2.92	74.53
SD3-y	0.48	97.45	1.24	81.80
PK1-y	1.11	99.60	1.91	97.59
PK2-y	0.23	95.51	1.03	50.29
PK3-y	0.13	76.02	1.02	12.29

4.4 Fatigue Load Estimation

The underlying aim of this work is to be able to predict the damage that the tower has suffered in terms of fatigue. Damage Equivalent Loads are often used to do so. The damage equivalent load, in terms of stresses, is defined by (see e.g., [43]):

$$\Delta\sigma_{eq} = \sqrt[m]{\frac{\sum_i \Delta\sigma_i^m N_i}{N_{ref}}}$$

With $\Delta\sigma_i$ stress ranges and N_i the corresponding number of cycles. m is a material constant referring to the idealised straight slope observed on a double-logarithmic scaled SN-curve. $\Delta\sigma_{eq}$ is the damage equivalent load, and N_{ref} the number of cycles of the equivalent load. In words, the damage generated by the set of stress ranges $\Delta\sigma_i$ with associated stress cycles N_i would be the same to the damage generated by the equivalent stress range $\Delta\sigma_{eq}$ with associated stress cycle N_{ref}. This under the assumption of linear accumulation of damage (Palmgren-Miner rule, [43]).

The stress ranges and corresponding number of cycles are determined using the rainflow counting method on the analysed records (omitting the initial and last 100[s] from the analysis, as discussed in 4.3.3). The rainflow counting method is applied to each record, and subsequently combined to generate the stress ranges and corresponding number of cycles for all the records analysed. The result is shown in Figure 4-41. Note that stresses are computed by multiplying the obtained strains with the assumed modulus of elasticity $E = 200000[MPa]$. Consequently, the damage equivalent load, and relative errors, are presented in Table 4-8. The damage equivalent load is detailed for each record in Table 4-9 and Table 4-10. Note that the material constant is set as $m = 4$ and the reference number of cycles is set as $N_{ref} = 10^7$, as per industry standard.

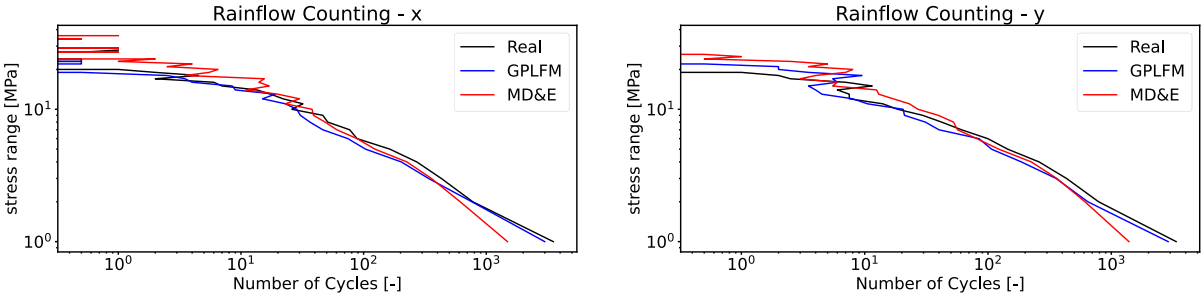

Figure 4-41. Stress ranges and number of cycles. Rainflow counting method.

Table 4-8. Damage Equivalent Load. All records summary.

	Measured	*GPLFM*		*MD&E*	
Direction	$\Delta\sigma_{eq}[MPa]$	$\Delta\hat{\sigma}_{eq}[MPa]$	$e_{\Delta\hat{\sigma}_{eq}}[\%]$	$\Delta\hat{\sigma}_{eq}[MPa]$	$e_{\Delta\hat{\sigma}_{eq}}[\%]$
x	0.860	0.820	-4.71	1.072	$+24.59$
y	0.733	0.801	$+9.36$	0.961	$+31.18$
$\sqrt{x^2+y^2}$	1.130	1.146	$+1.45$	1.439	$+27.40$

Table 4-9. Damage Equivalent Load. All records. Local direction x.

	Measured	*GPLFM*		*MD&E*	
ID	$\Delta\sigma_{eq}[MPa]$	$\Delta\hat{\sigma}_{eq}[MPa]$	$e_{\Delta\hat{\sigma}_{eq}}[\%]$	$\Delta\hat{\sigma}_{eq}[MPa]$	$e_{\Delta\hat{\sigma}_{eq}}[\%]$
OP1-x	0.090	0.084	-6.35	0.175	$+94.64$
OP2-x	0.064	0.061	-4.87	0.090	$+40.47$
OP3-x	0.326	0.328	$+0.52$	0.404	$+24.09$
OP4-x	0.478	0.460	-3.74	0.585	$+22.44$
OP5-x	0.548	0.551	$+0.63$	0.684	$+24.92$
OP6-x	0.739	0.666	-9.86	0.916	$+24.04$
OP7-x	0.530	0.532	$+0.50$	0.662	$+25.04$
SU1-x	0.208	0.230	$+10.81$	0.270	$+29.97$
SU2-x	0.253	0.247	-2.53	0.336	$+32.86$
SU3-x	0.031	0.019	-40.22	0.052	$+67.39$
SD1-x	0.231	0.266	$+14.86$	0.307	$+32.63$
SD2-x	0.168	0.160	-4.73	0.225	$+33.40$
SD3-x	0.086	0.097	$+12.22$	0.121	$+39.78$
PK1-x	0.299	0.343	$+14.77$	0.411	$+37.63$
PK2-x	0.046	0.054	$+16.97$	0.070	$+51.40$
PK3-x	0.008	0.010	$+14.81$	0.044	$+430.15$

Table 4-10. Damage Equivalent Load. All records. Local direction y.

	$Measured$	$GPLFM$		$MD\&E$	
ID	$\Delta\sigma_{eq}[MPa]$	$\Delta\hat{\sigma}_{eq}[MPa]$	$e_{\Delta\hat{\sigma}_{eq}}[\%]$	$\Delta\hat{\sigma}_{eq}[MPa]$	$e_{\Delta\hat{\sigma}_{eq}}[\%]$
OP1-y	0.154	0.109	−29.26	0.201	+30.29
OP2-y	0.088	0.083	−6.02	0.139	+58.03
OP3-y	0.323	0.290	−9.92	0.412	+27.63
OP4-y	0.344	0.349	+1.35	0.428	+24.37
OP5-y	0.436	0.438	+0.51	0.575	+31.92
OP6-y	0.644	0.746	+15.90	0.865	+34.36
OP7-y	0.467	0.425	−9.09	0.560	+19.90
SU1-y	0.178	0.195	+9.65	0.228	+28.11
SU2-y	0.218	0.231	+5.98	0.268	+22.81
SU3-y	0.037	0.042	+16.22	0.063	+73.39
SD1-y	0.134	0.151	+12.08	0.213	+58.37
SD2-y	0.189	0.206	+9.00	0.261	+37.92
SD3-y	0.073	0.086	+17.89	0.106	+44.57
PK1-y	0.203	0.239	+17.66	0.264	+30.15
PK2-y	0.028	0.034	+20.45	0.060	+112.20
PK3-y	0.010	0.012	+18.64	0.047	+376.92

4.5 Discussion

The mechanical model is deemed to be a reasonable representation of the structure as the three bending modes of the tower are observed from identification (see Table 4-2 and Table 4-3). Note that the available information is insufficient to conclude exactly which identified mode represents the third mode, as there are at least two reasonable candidates present in the analysis. However, the relevance of the system identification in the context of this work is to validate the mechanical model. Given that at least one of them should be associated to the third mode, and noticing that they are reasonably accurate, the ignorance regarding exactly which one represents the third mode is not a problem for the subsequent analysis. Furthermore, note that the strain is related to lower frequencies (as it is related to displacements), therefore the accuracy of the first and second mode are more relevant than the third mode.

It is highlighted that this model is not a perfect representation of the real structure, and can be improved. However, given that the same model is used for both response estimation methods, it is considered to be accurate enough to allow a reasonable comparison between them. Many improvements may be considered for future works. Some of them are: the inclusion of aerodynamic damping effect, the addition of soil stiffness, and the addition of the mass moment of inertia on top of the structure. It is highlighted that several modes were identified which are not captured by the mechanical model. These may correspond to rotor modes or torsional modes.

The fitting of the prior is applied by computing the joint distribution surface and finding the maximum as the initial guess for the optimisation algorithm. This initial guess will always be close to the final solution, thus ensuring good results from the optimisation. Note that this process is not computationally expensive given that the only relevant computation needed in each iteration is solving the continuous-time Lyapunov equation (see section 2.4.4.2). This is particularly true when compared with the Maximum A Posteriori approach. As illustrated by Figure 4-26 to Figure 4-28, the prior fit is not perfect. This is not due to failure in finding the best hyperparameters to describe the

load, but rather the failure of the model itself to accurately represent the real response of the structure. Note that the model used includes an assumption regarding the location of the load (horizontal load applied on top).

The σ and l_{sc} found for each record are summarised in Table 4-4 and Table 4-5. Note that, in general, the l_{sc} is relatively constant for most of the records ($l_{sc} \approx 0.05[s]$). Note that, as mentioned in section 2.4.2.3, a relevant correlation can be found up to $5l_{sc}$. Imposing that there should be a relevant amount of correlation between time steps defines a minimum l_{sc} given by: $5l_{sc} > \Delta t \Rightarrow l_{sc} > 0.01[s]$. In all cases the l_{sc} estimated is larger, which means that there is always some relevant correlation between time steps. Furthermore, note that σ tends to increase as the wind speed is higher. This is a direct consequence of higher wind speeds yielding higher amplitudes of the response.

The fitting of the posterior was observed to sometimes fail in finding a relative error lower than the defined tolerance. To explain the observed behaviour, it is important to realise that the model is not perfect. This brings as a consequence that the part of the real response that cannot be captured by the model will be considered as noise. Furthermore, this noise may not behave like a white gaussian noise. This justifies why the convergence is not ensured. The proposed solution, which is to stop the iteration once the relative error stops decreasing, still provides a reasonable solution for the overall process. Note that the fitting of the posterior aims to define a noise level that provides a reasonably accurate estimation for the strain, not to define the exact noise level that the sensor has. The estimation obtained is shown to be accurate in comparison to the MD&E, even for the cases when the iteration has stopped, as presented in section 4.3.3.

Table 4-6 and Table 4-7 summarises the error metrics obtained for both response estimation methods. The MAE is observed to be lower when using the GPLFM method. For all cases. This means that the GPLFM is consistently more accurate than the MD&E. The $TRAC$ is not always lower for the GPLFM, there are a few exceptions observed. Note however that these exceptions yield a very low difference between the $TRAC$ values obtained from each method. In summary, these numerical results clearly show that the GPLFM method is more accurate.

The comparison was extended into the calculation of Damage Equivalent Loads from all the records analysed. The results are summarised in Table 4-8. The resulting Damage Equivalent Loads obtained are observed to be more accurate when using the GPLFM method. From Table 4-9 and Table 4-10 the MD&E are observed to be always overestimating the measured Damage Equivalent Load. This is mainly attributed to the fact that the noise is considered to be part of the response. These results further conclude numerically that the GPLFM is an improvement when compared with the MD&E method.

5 Conclusion

The aim of this work is to answer the research question exposed in section 1.3:

"Does the novel GPLFM method improves upon existing methods?"

In consistency with the methodology defined in section 1.4, the answer is provided from a theoretical point of view and a numerical point of view, and can be briefly stated as follows:

"The GPLFM is an improvement upon existing methods, from both a theoretical and a numerical point of view"

The results that justify this answer are summarised in section 5.1 and 5.2 for the theoretical and numerical assessment, respectively. Section 5.3 provides some relevant observations and recommendations for future works regarding the use of the GPLFM.

5.1 Theoretical assessment

The response estimation methods were divided into three: the Kalman Filter based methods, the MD&E method, and the novel GPLFM.

The GPLFM was recognised in section 1.2 to be also part of the Kalman Filter based methods, and it was observed to be an improvement: it has no stability issues, and it provides a robust way to represent the unknown load instead of assuming it to be a white gaussian noise. Furthermore, in the GPLFM method the stochastic representation of the load is left for the user to be defined. The stochastic definition for the load employed in this work is based upon an adjustable covariance function which only imposes correlations between close points in time. The amplitude of the load and the extent of the correlations are fully controlled by the hyperparameters σ and l_{sc}, as discussed in section 2.4.2.3. It is highlighted that the GPLFM method is not restricted to this covariance function, if there is prior knowledge of harmonics in the load for example, this information could be fed into the model by a periodic covariance function.

The MD&E has been observed to be a very simple yet effective way to estimate the response. From a theoretical perspective, this method neglects the measurement noise, and it requires integration in order to find strains from accelerations. In contrast with the GPLFM: the measurement noise is taken into account, and no integration is required. As a consequence, the GPLFM provides an improved framework for response estimation. It is highlighted however that the simplicity of the MD&E method is translated in less computational cost to implement it when compared with the GPLFM method.

In conclusion, from a theoretical point of view, the GPLFM method has been observed as an improvement upon existing methods.

5.2 Numerical assessment

The numerical assessment has been restricted to a comparison between the MD&E and the GPLFM methods as a consequence of the literature review (see section 1.2). The comparison is made initially upon a simulation, and subsequently upon a real structure.

From the simulation results, as presented in section 3, the response estimation methods are illustrated and validated. The obtained results are accurate for both methods, as expected, but the accuracy is observed to be improved for the GPLFM method. The difference however is low. The simulation also illustrates and validates the approach used for system identification upon the real structure.

For the real structure, a mechanical model was built and validated through system identification. The mechanical model employed was observed to be a simplistic approach of reality, but given that the same mechanical model is used by both methods, it is a sufficient model for the numerical assessment. A set of records are defined for the analysis, they are selected to be representative of the different operational conditions relevant for fatigue design of the wind turbine. The analysis shows that better results are obtained when using the GPLFM for all records. This is further extended in the calculation of Damage Equivalent Loads, providing a measure of accuracy for all records analysed. The result shows a relative error that, depending on operational conditions, ranges within 20-40[%] for the MD&E and less than 10[%] for the GPLFM.

The results obtained from the numerical assessment shows that the GPLFM is an improvement upon the MD&E method. This is valid for both the simulation and the real structure evaluated. From a practical point of view however, the increased computational cost associated to the GPLFM must be taken into account.

5.3 Observations and recommendations for future works

Even though the GPLFM method employed in this work is based upon what has been proposed in [18] for response estimation, there are some differences in the methodology employed that should be noted. This takes into account recent methodologies found in [19] and the underlying theory that can be found in [40] and [39]. In [18], the stationary covariance is defined only for the load and disregards the computation of the stationary covariance for the complete system. Furthermore, an additional white gaussian noise is defined to represent model errors. The approach considered in this work considers the stationary covariance for the complete system (see section 2.4.4.2), which defines as a consequence a physically meaningful white gaussian noise related to the model. This approach is also exposed in [19], although formulated for the context of joint input-state-parameter estimation.

The ‘Fitting of the prior and posterior’ is a new approach for parameter estimation in the context of GPLFM. It has been shown to provide a more intuitive and efficient way to compute the parameters when compared with the ‘Maximum A Posteriori’ approach. The Maximum A Posteriori approach presented here is not the only approach found in literature. For example, in [19] a Markov Chain Monte Carlo is used to perform inference. Note that this method would be even more expensive computationally. Other methods can be found in [39] such as Expectation Maximisation, or a Gradient-based optimisation approach. All these methods follow the same strategy of parameter estimation through maximising the posterior. Research aimed on finding a robust and efficient approach based on maximising the posterior is recommended for future works. The ‘fitting of the prior and posterior’ method may be considered as an intuitive and practical way to verify the results.

Future works should consider an improved mechanical model to represent the wind turbine. The main improvements to consider are: the use of an additional moment load applied on top or modal loads, inclusion of mass moment of inertia (thus distinguishing between FA and SS directions), inclusion of soil stiffness, and inclusion of aerodynamic damping. These additional parameters may change in time, therefore online identification and model updating should be considered. Furthermore, the strain estimations should be sought in the whole frequency range, this can be realised by including measurements that deliver this information (strain measurements, GPS sensors, inclinometers, etc.). It is important to realise that filtering of quasi-static information of accelerometers is not a requirement for applying the GPLFM. The resulting estimation will still be stable, but the quasi-static frequencies will still not be able to be observed from the accelerations. This contrasts with employing the MD&E method, where filtering is a requirement when using accelerations. As a consequence, the GPLFM has the potential to provide a single framework to find the full strain estimation.

Bibliography

[1] United Nations, “Paris Agreement, FCCC/CP/2015/L.9/Rev.1.” 2015.

[2] IRENA, “Future of wind: Deployment, investment, technology, grid integration and socio-economic aspects (A Global Energy Transformation paper).” 2019.

[3] T. Burton, Ed., *Wind energy handbook*, 2nd ed. Chichester, West Sussex: Wiley, 2011.

[4] Det Norske Veritas and Germanischer Lloyd, “DNVGL-ST-0262, Lifetime extension of wind turbines.” 2016.

[5] K. Maes, A. Iliopoulos, W. Weijtjens, C. Devriendt, and G. Lombaert, “Dynamic strain estimation for fatigue assessment of an offshore monopile wind turbine using filtering and modal expansion algorithms,” *Mechanical Systems and Signal Processing*, vol. 76–77, pp. 592–611, Aug. 2016, doi: 10.1016/j.ymssp.2016.01.004.

[6] S. Chauhan *et al.*, “Operational Modal Analysis of Operating Wind Turbines: Application to Measured Data,” in *Rotating Machinery, Structural Health Monitoring, Shock and Vibration, Volume 5*, T. Proulx, Ed. New York, NY: Springer New York, 2011, pp. 65–81. doi: 10.1007/978-1-4419-9428-8_6.

[7] G. Oliveira, “Vibration-Based Structural Health Monitoring of Wind Turbines,” Ph.D. Thesis, Universidade do Porto, Porto, 2016.

[8] R. E. Kalman, “A New Approach to Linear Filtering and Prediction Problems,” *Journal of Basic Engineering*, p. 12, 1960.

[9] E. Lourens, E. Reynders, G. De Roeck, G. Degrande, and G. Lombaert, “An augmented Kalman filter for force identification in structural dynamics,” *Mechanical Systems and Signal Processing*, vol. 27, pp. 446–460, Feb. 2012, doi: 10.1016/j.ymssp.2011.09.025.

[10] K. Maes, E. Lourens, K. Van Nimmen, E. Reynders, G. De Roeck, and G. Lombaert, “Design of sensor networks for instantaneous inversion of modally reduced order models in structural dynamics,” *Mechanical Systems and Signal Processing*, vol. 52–53, pp. 628–644, Feb. 2015, doi: 10.1016/j.ymssp.2014.07.018.

[11] F. Naets, J. Cuadrado, and W. Desmet, “Stable force identification in structural dynamics using Kalman filtering and dummy-measurements,” *Mechanical Systems and Signal Processing*, vol. 50–51, pp. 235–248, Jan. 2015, doi: 10.1016/j.ymssp.2014.05.042.

[12] S. Eftekhar Azam, E. Chatzi, and C. Papadimitriou, “A dual Kalman filter approach for state estimation via output-only acceleration measurements,” *Mechanical Systems and Signal Processing*, vol. 60–61, pp. 866–886, Aug. 2015, doi: 10.1016/j.ymssp.2015.02.001.

[13] K. Tatsis and E. Lourens, “A comparison of two Kalman-type filters for robust extrapolation of offshore wind turbine support structure response,” in *Life-Cycle of Engineering Systems*, 1st ed., J. Bakker, D. M. Frangopol, and K. van Breugel, Eds. CRC Press, 2016, pp. 209–216. doi: 10.1201/9781315375175-20.

[14] S. Gillijns and B. De Moor, “Unbiased minimum-variance input and state estimation for linear discrete-time systems with direct feedthrough,” *Automatica*, vol. 43, no. 5, pp. 934–937, May 2007, doi: 10.1016/j.automatica.2006.11.016.

[15] E. Lourens, C. Papadimitriou, S. Gillijns, E. Reynders, G. De Roeck, and G. Lombaert, “Joint input-response estimation for structural systems based on reduced-order models and vibration data from a limited number of sensors,” *Mechanical Systems and Signal Processing*, vol. 29, pp. 310–327, May 2012, doi: 10.1016/j.ymssp.2012.01.011.

[16] K. Maes, A. W. Smyth, G. De Roeck, and G. Lombaert, “Joint input-state estimation in structural dynamics,” *Mechanical Systems and Signal Processing*, vol. 70–71, pp. 445–466, Mar. 2016, doi: 10.1016/j.ymssp.2015.07.025.

[17] A. Iliopoulos, R. Shirzadeh, W. Weijtjens, P. Guillaume, D. V. Hemelrijck, and C. Devriendt, “A modal decomposition and expansion approach for prediction of dynamic responses on a monopile offshore wind turbine using a limited number of vibration sensors,” *Mechanical Systems and Signal Processing*, vol. 68–69, pp. 84–104, Feb. 2016, doi: 10.1016/j.ymssp.2015.07.016.

[18] R. Nayek, S. Chakraborty, and S. Narasimhan, “A Gaussian process latent force model for joint input-state estimation in linear structural systems,” *Mechanical Systems and Signal Processing*, vol. 128, pp. 497–530, Aug. 2019, doi: 10.1016/j.ymssp.2019.03.048.

[19] T. J. Rogers, K. Worden, and E. J. Cross, “On the application of Gaussian process latent force models for joint input-state-parameter estimation: With a view to Bayesian operational identification,” *Mechanical Systems and Signal Processing*, vol. 140, p. 106580, Jun. 2020, doi: 10.1016/j.ymssp.2019.106580.

[20] R. Baudisch, “Structural Health Monitoring of Offshore Wind Turbines,” M.Sc. Thesis, Danmarks Tekniske Universitet, 2012.

[21] A. Iliopoulos, C. Devriendt, P. Guillaume, and D. Van Hemelrijck, “Continuous Fatigue Assessment of an Offshore Wind Turbine Using a Limited Number of Vibration Sensors,” in *7th European Workshop on Structural Health Monitoring*, La cité, Nantes, France, Jul. 2014, p. 8.

[22] A. Iliopoulos, W. Weijtjens, D. Van Hemelrijck, and C. Devriendt, “Fatigue assessment of offshore wind turbines on monopile foundations using multi-band modal expansion: Fatigue assessment of monopile OWTs using multi-band modal expansion,” *Wind Energ.*, vol. 20, no. 8, pp. 1463–1479, Aug. 2017, doi: 10.1002/we.2104.

[23] N. Noppe, A. Iliopoulos, W. Weijtjens, and C. Devriendt, “Full load estimation of an offshore wind turbine based on SCADA and accelerometer data,” *J. Phys.: Conf. Ser.*, vol. 753, p. 072025, Sep. 2016, doi: 10.1088/1742-6596/753/7/072025.

[24] N. Noppe, K. Tatsis, E. Chatzi, C. Devriendt, and W. Weijtjens, “Fatigue stress estimation of offshore wind turbine using a Kalman filter in combination with accelerometers,” in *28th International Conference on Noise and Vibration engineering (ISMA2018)*, Dec. 2018, p. 10.

[25] R. W. Clough and J. Penzien, *Dynamics of structures*. New York: McGraw-Hill, 1975.

[26] A. K. Chopra, *Dynamics of structures: theory and applications to earthquake engineering*. Englewood Cliffs, N.J: Prentice Hall, 1995.

[27] G. R. Liu and S. S. Quek, *The finite element method: a practical course*, Second edition. Amsterdam ; Oxford: Butterworth-Heinemann, 2014.

[28] M. Weber, “Structural health monitoring of offshore wind monopiles - Automated identification of the modal parameters,” M.Sc. Thesis, Technische Universität Darmstadt, 2020.

[29] C. Devriendt, F. Magalhães, W. Weijtjens, G. De Sitter, Á. Cunha, and P. Guillaume, “Structural health monitoring of offshore wind turbines using automated operational modal analysis,” *Structural Health Monitoring*, vol. 13, no. 6, pp. 644–659, Nov. 2014, doi: 10.1177/1475921714556568.

[30] B. Peeters and G. De Roeck, “Reference-based Stochastic Subspace Identification for Output-Only Modal Analysis,” *Mechanical Systems and Signal Processing*, vol. 13, no. 6, pp. 855–878, Nov. 1999, doi: 10.1006/mssp.1999.1249.

[31] B. Peeters and H. Van der Auweraer, “PolyMax: a revolution in operational modal analysis,” presented at the 1st International Operational Modal Analysis Conference, 2005.

[32] E. Reynders, J. Houbrechts, and G. De Roeck, “Fully automated (operational) modal analysis,” *Mechanical Systems and Signal Processing*, vol. 29, pp. 228–250, May 2012, doi: 10.1016/j.ymssp.2012.01.007.

[33] M. Ankerst, M. M. Breunig, H.-P. Kriegel, and J. Sander, “OPTICS: Ordering Points To Identify the Clustering Structure,” *Wiley Interdisciplinary Reviews: Data Mining and Knowledge Discovery*, vol. 1, no. 3, pp. 231–240.

[34] R. L. Boroschek and J. A. Bilbao, “Interpretation of stabilization diagrams using density-based clustering algorithm,” *Engineering Structures*, vol. 178, pp. 245–257, Jan. 2019, doi: 10.1016/j.engstruct.2018.09.091.

[35] B. Peeters, “Proefschrift voorgedragen tot het behalen van het doctoraat in de toegepaste wetenschappen door,” p. 257, 2000.

[36] V. Zabel, “Operational modal analysis Theory and aspects of application in civil engineering,” Thesis, Bauhaus-Universität Weimar, 2019.

[37] R. J. Allemang, “The Modal Assurance Criterion – Twenty Years of Use and Abuse,” *SOUND AND VIBRATION*, p. 8, 2003.

[38] C. E. Rasmussen and C. K. I. Williams, *Gaussian processes for machine learning*. Cambridge, Mass: MIT Press, 2006.

[39] J. Hartikainen and S. Särkkä, “Kalman filtering and smoothing solutions to temporal Gaussian process regression models,” in *2010 IEEE International Workshop on Machine Learning for Signal Processing*, Kittila, Finland, Aug. 2010, pp. 379–384. doi: 10.1109/MLSP.2010.5589113.

[40] S. Särkkä and A. Solin, *Applied stochastic differential equations*. Cambridge ; New York, NY: Cambridge University Press, 2019.

[41] S. Särkkä, *Bayesian filtering and smoothing*. Cambridge, U.K. ; New York: Cambridge University Press, 2013.

[42] International Electrotechnical Commission, *Wind energy generation systems. design requirements Part 1*. 2019.

[43] N. Cosack, “Fatigue load monitoring with standard wind turbine signals,” Ph.D. Thesis, Universität Stuttgart, 2010.

List of Figures

List of Tables